[127]. The phase of the temperature gradient generation is the same as the phase of displacement. The thermal diffusion is determined by the thermal conductivity (k), density (ρ), and specific heat (c_p) of the material. The energy loss due to TED is also proportional to the phase offset between the stress and strain profile during oscillation cycles.

Anchor loss is due to the transfer of acoustic energy from the resonator to the substrate. The amount of acoustic energy transferred to the substrate is proportional to the stress profile at the anchor interface. The analytical expression of anchor loss for a simple cantilever was studied by Jimbo [113]. They first calculated the axial force, moment, and the shear force acting on a beam with an ideal anchor. The forces were applied to the 2D wave equation to compute the amount of displacement at the anchor, with an assumption that the substrate is a half-infinite domain and no waves are reflected back to the resonator. A similar analytical study was done by Hao [114] for a MEMS cantilever and clamped-clamped-beam resonator. Bindel presented a method to calculate anchor loss using FEM [115]. To model zero reflection from the boundary to the model,

Table 5.3. Geometry, electrical properties, and physical properties of the 1st generation CING

Geometry and Electrical Properties				Calculated Physical Properties	
Outer radius (R)	2.5mm	Side electrode capacitance (gap: 9μm)	290fF	Wineglass mode freq. (f_{WG})	17.3kHz (T=30μm) 23.1kHz (T=40μm)
Anchor radius (AR)	1mm	Bottom electrode capacitance (gap: 2.5μm)	3.7pF	Tilting mode freq. ($f_{tilting}$)	>30kHz
Ring thickness (T)	30, 40μm			Vertical mode freq. ($f_{vertical}$)	>50kHz
Anchor thickness (AT)	100μm			Angular gain (A_g) (ANSYS)	0.07
Bottom plate thickness (BT)	30~50μm			Effective mass (M)	~700μg

a mechanical Perfectly Matched Layer (PML) was included near the boundary. The mechanical PML absorbs the incident elastic wave of all wavelengths from all angles, and is available in commercial FEM programs, including COMSOL. One of the critical challenges in mechanical simulation with PML is excessive computing time. The properties of the mechanical PML can be approximated by using a mechanical Matched Layer (ML) [116]. The difference between the ML and is the PML is that the ML only absorbs the wave that is along the normal direction to the surface. By careful selection of the geometry for the ML region, very close matching of Q_{anchor} using the ML and PML was found in [116]. In this study, we use FEM with a ML to calculate the anchor loss of the CING.

Surface loss is caused by uneven stress distribution at the surface of a resonator due to surface roughness. The approximation of the dependency of $Q_{surface}$ on surface roughness, geometry, and mode can be obtained by modeling a resonator as a perfect resonator, surrounded by a thin, damaged material layer [117]. Following this analysis, we can find the location on the CING that provides the largest contribution to $Q_{surface}$.

5.3.1. Calculation of Thermoelastic Damping (TED)

An approximate expression for Q_{TED} can be expressed in terms of the relaxation strength (Δ), frequency (ω), and the thermal diffusion time constant (τ_h), as shown in Equation 5.5-Equation 5.8.

$$\frac{1}{Q_{TED}} = \frac{\alpha^2 T_{initial} E}{c_p \rho} \frac{\omega\tau}{1+\left(\omega\tau\right)^2} \qquad \text{(Equation 5.5)}$$

$$\Delta = \frac{\alpha^2 T_{initial} E}{c_p \rho} \qquad \text{(Equation 5.6)}$$

$$\tau_h = \frac{b^2}{\pi^2 \chi} \qquad \text{(Equation 5.7)}$$

$$\chi = \frac{\kappa}{c_p \rho} \qquad \text{(Equation 5.8)}$$

In Equation 5.5, α (K^{-1}) denotes the linear thermal expansion coefficient, $T_{initial}$ (K) denotes the nominal temperature, E (Pa) denotes Young's modulus, c_p (J/kg/K) denotes the specific heat under a constant pressure, ρ (kg/m^3) denotes the density, b (m) denotes the width of the beam where thermal field is generated, and κ (W/mK) denotes thermal conductivity. The relationship between oscillation frequency ω normalized to τ and Q_{TED}^{-1} is plotted in Figure 5.11. The loss, Q_{TED}^{-1}, reaches the maximum value when ω is equal to τ^{-1}. At this frequency, the thermal gradient and the thermal conduction are balanced and create the largest out-of-phase stress. When ω is smaller than τ^{-1}, the thermal diffusion process dominates the thermal gradient generation process. In this region, thermal equilibrium is reached more quickly than the mechanical oscillation period leading to a more uniform temperature profile across the strained and compressed regions of the resonator. As the temperature profile across the resonator becomes more uniform, the amount of thermal expansion per oscillation reduces, so less energy is dissipated during oscillation. When ω is larger than τ^{-1}, the thermal gradient generation process dominates the diffusion process. In this region, the oscillation period is small compared to the thermal equilibrium time constant leading to a more bipolar temperature profile. The phase of the strain due to thermal expansion matches the strain due to mechanical oscillation of the resonator which leads to less energy dissipated per oscillation.

The Q_{TED} can be controlled by choice of material, width of critical beams (b) where the temperature gradient is created, and the oscillation frequency (ω). MEMS materials with high thermal conductivity, such as Si (κ: 130W/mK) and diamond (κ: 2200W/mK), have lower nominal thermal diffusion time constants (τ) than other MEMS materials. With these materials, a higher Q_{TED} can be achieved by reducing both b, which increases τ^{-1} and ω, which increases the separation between the maximum damping frequency and the operating frequency. On the other hand, MEMS materials with lower thermal conductivity, such as fused silica (κ: 1.3W/mK), have larger τ than other MEMS materials. In this case, a larger Q_{TED} can be achieved by increasing b and increasing the ω.
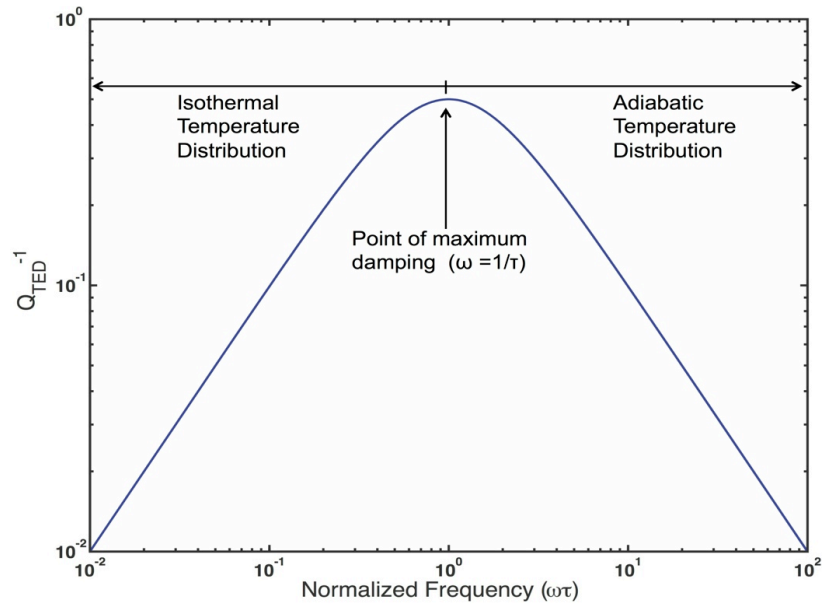

Figure 5.11. Relationship between oscillation frequency normalized to thermal diffusion time constant ($\omega\tau$) and Q_{TED}^{-1} from [106].

The temperature profile of the cross-section of a CING in the $n=2$ wineglass mode is found using ANSYS for the geometry in Table 5.3. In the simulation, the number of rings (N) is reduced to 30 to reduce the simulation time. Using the meshing element in

for calculating the TED loss, the wineglass mode is found at 25.7kHz. In the harmonic analysis, pressures are applied from the bottom plate along the z-axis to deform the gyro in the shape closest to the wineglass mode. Figure 5.12 shows that a temperature gradient is generated 1) at the interface between the bottom plate and the multiple rings, especially at the innermost ring, 2) across the ring, along the radial direction (x-axis), and 3) parallel to its thickness (z-axis).
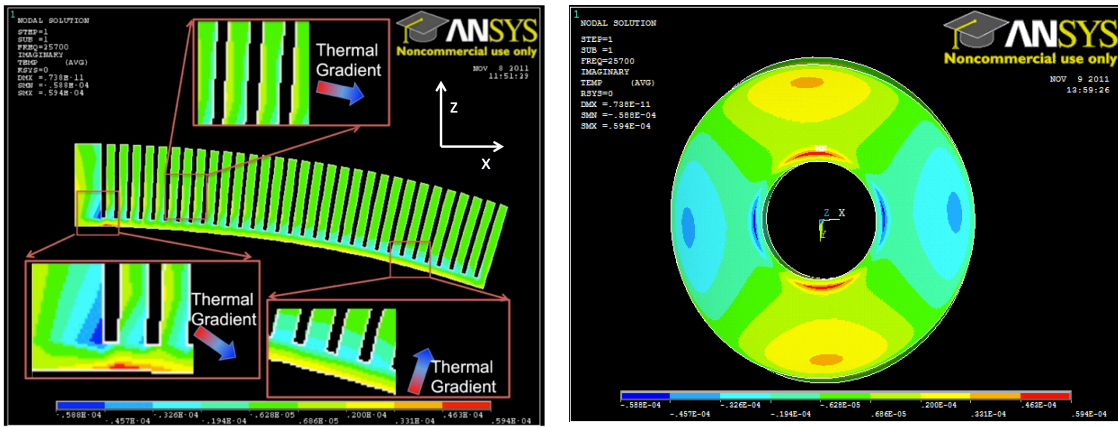
(a) Temperature distribution for the cross-sectional plane of the CING

(b) Temperature distribution of the bottom plate of the CING

Figure 5.12. Cross-sectional view of the temperature distribution of the CING, simulated from harmonic analysis after applying complementary Z-axis pressure from the bottom plate of the resonator. The gyro dimension includes outer radius (*R*) of 2.5mm, anchor radius (*AR*) of 1mm, height (*H*) of 300μm, ring thickness (*T*) of 30μm, bottom plate thickness (*BT*) of 30μm, and number of rings (*N*) of 30. The simulation is conducted at 25.7kHz.

The amount of TED is not uniformly distributed in the CING. In Figure 5.13, the CING is divided into three regions to understand the amount of energy dissipation. The regions are: 1) lower half of the bottom plate, 2) upper half of the bottom plate to the lower one-fifth of the ring, which includes the corner between the rings and the bottom plate, and 3) and the upper four-fifth of the ring. Table 5.4 shows the ratio between the average stored energy (E_{avg}), average dissipated energy (ΔE_{avg}) during a single oscillation cycle, and the ratio between the ΔE_{avg} and E_{avg} for each region. The ratio between the

average energy loss and the stored energy $\Delta E_{avg}/E_{avg}$ is termed the local Q_{TED}^{-1}. The FEM analysis calculated that the local Q_{TED}^{-1} is largest in Region 2 followed by Region 1, and the Region 3. The difference is attributed to the different amounts of stress concentration during an oscillation.
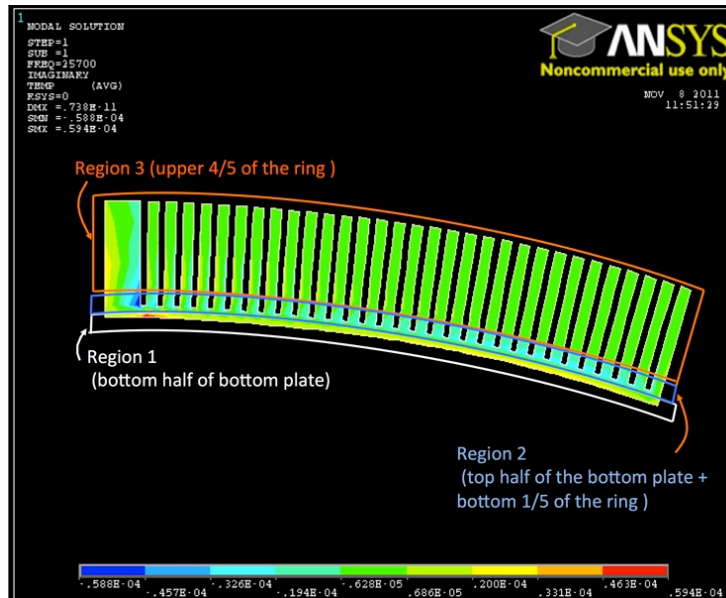

Figure 5.13. Divisions of regions used for local TED analysis.

5.3.1.1. Relation Between the Bottom Plate Thickness (*BT*) and *Q*$_{TED}$

The bottom plate of the cylinder is the critical location for TED. The dependency of the overall Q_{TED} on the bottom plate thickness (*BT*) is shown in Figure 5.14. The simulation results are compared with the Q_{TED} from Zener's expression, for a simple bending beam [106]. The two calculation results agree well for *BT* of >30μm, indicating that the dominant loss mechanism for the bottom plate at this *BT* range is due to thermal diffusion across the surfaces of the bottom plate, similar to a simple bending beam; however, as the *BT* becomes less than 20μm, the simulated Q_{TED} of the CING starts to be smaller than the Q_{TED} from Zener's expression, indicating that a damping source, which

does not exist in the simple bending beam, starts to dominate the overall damping. The source of damping at this region is believed to be the stress developed at sharp corners formed between the rings and the bottom plate. In this case, Q_{TED} can be improved by rounding the corners, possibly by applying an isotropic etchant after the DRIE step.

5.3.1.2. Relationship Between the Number of Rings (*N*) and Q_{TED}

The stress profile caused from the multiple rings has the same shape at each ring, so each ring is expected to have the same local Q_{TED}^{-1}. As the number of the rings (*N*) increases, the average energy loss ΔE_{avg} and the overall stored energy E_{avg} are both expected to increase with a constant rate. As a result, an increase in *N* is not expected to affect Q_{TED} significantly. Figure 5.15 shows the relationship between Q_{TED} and four different values of *N* (5, 10, 20, and 30). The rest of the geometry is kept the same with the previous calculations. Compared to *BT*, the influence of *N* on Q_{TED} is small.

Table 5.4. Normalized stored and dissipated energies from TED for three different regions of the CING (Section 1-3). Gyro dimension includes outer radius (*R*) of 2.5mm, anchor radius (*AR*) of 1mm, height (*H*) of 300μm, ring thickness (*T*) of 30μm, bottom plate thickness (*BT*) of 30μm, and number of rings (*N*) of 30. The simulation is conducted at 25.7kHz.

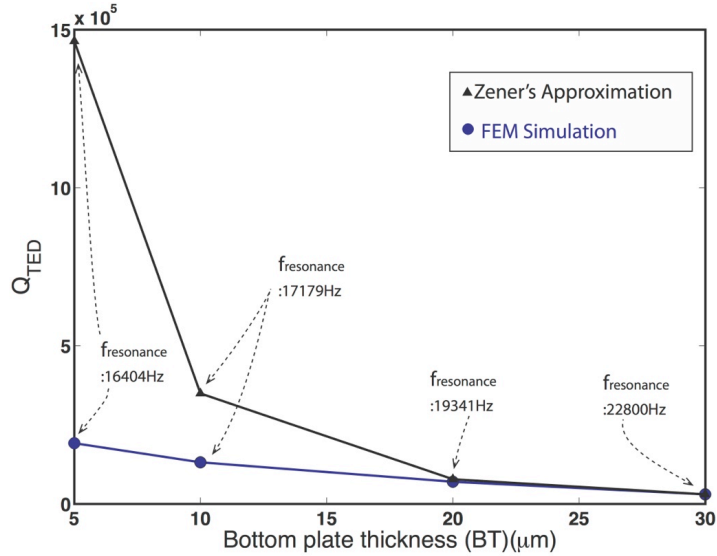|	Average stored strain energy ($E_{avg,local}$ / E_{avg})	Average dissipated energy ($\Delta E_{avg,local}$ / E_{avg})	Ratio between and ΔE and E_{avg} (Local Q_{TED}^{-1})
Section 1 (Lower half of the bottom plate)	22.2%	33.1%	1.49
Section 2 (Upper half of bottom plate to the lower 1/5 of ring)	34.8 %	54.7%	1.57
Section 3 (Upper 4/5 of the ring)	43%	12.2%	0.28
Total	100%	100%	NA

Figure 5.14. Relationship between the bottom plate thickness (*BT*) and the Q_{TED}, compared with Zener's expression for simple bended beam [106]. Gyro dimension includes outer radius (*R*) of 2.5mm, anchor radius (*AR*) of 1mm, height (*H*) of 300μm, ring thickness (*T*) of 30μm, and number of rings (*N*) of 30.

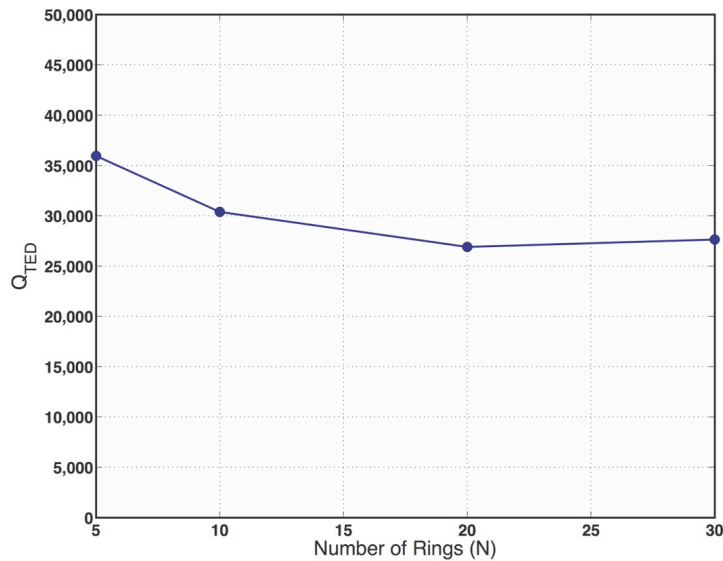Figure 5.15. Relation between the number of rings (*N*) and the Q_{TED}. The dimension of the gyro includes outer radius (*R*) of 2.5mm, anchor radius (*AR*) of 1mm, height (*H*) of 300μm, bottom plate thickness (*BT*) of 30μm, and ring thickness (*T*) of 30μm. The Q_{TED} is evaluated at 25.7kHz.

5.3.2. Anchor Loss

The anchor loss of the CING was calculated from a damped eigenvalue model of the gyro, where the substrate includes a matched layer (ML) to absorb the incident elastic

158

wave normal to the surface of the layer. To allow zero reflection at the interface between the glass and the ML, the acoustic impedance ($Z_{acoustic}$) of the ML is matched to the acoustic impedance of glass. The wave-absorbing characteristics of the ML can be modeled by introducing a negative exponential decay factor in the velocity of the incident wave. The Young's modulus E_{ML}, density ρ_{ML}, and the Poisson's ratio v_{ML} of the ML are related to the physical parameters of the substrate and the exponential decay factor (α_{decay}) by [116]:

$$E_{ML} = jE_{substrate}/\alpha_{decay} \qquad \text{(Equation 5.9)}$$

$$\rho_{ML} = -j\alpha_{decay}\rho_{substrate} \qquad \text{(Equation 5.10)}$$

$$v_{ML} = v_{substrate} \qquad \text{(Equation 5.11)}$$

The bottom substrate in the model is built with a length larger than the wavelength of the elastic wave in glass (λ_{glass}). The λ_{glass} is calculated by:

$$\lambda_{glass} = \frac{c_{glass}}{f_o} \qquad \text{(Equation 5.12)}$$

In Equation 5.12, c_{glass} denote the speed of sound in glass (~4000m/sec). The λ_{glass} for a 20kHz resonator is about 0.2 meters. The glass substrate is modeled with a half-sphere with a radius of 0.4 meters. The outer boundary of the substrate is surrounded with a ML layer, with a side length of 0.4 meters. The number of element divisions along the radial direction is set to 15, and the number of element divisions along the angular direction is set to 10. The number of elements was limited by the computation speed. Figure 5.16 shows the cross-sectional view of the entire reduced-ring-count model.
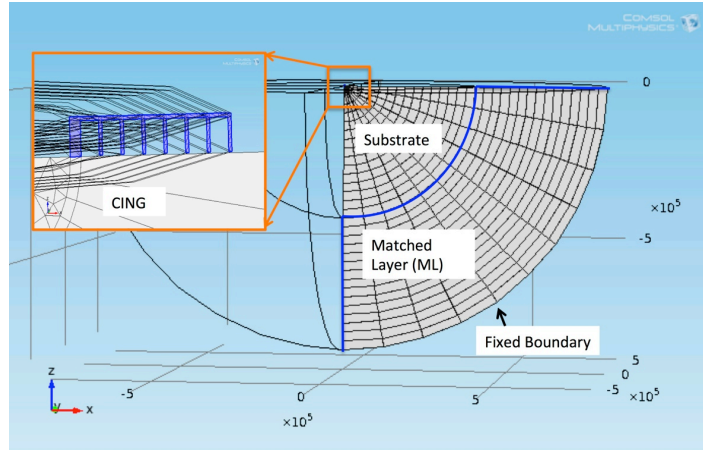
(a) Cross-sectional view of the meshing (element divisions along the radial direction is 15, element divisions along the angular direction is 10).
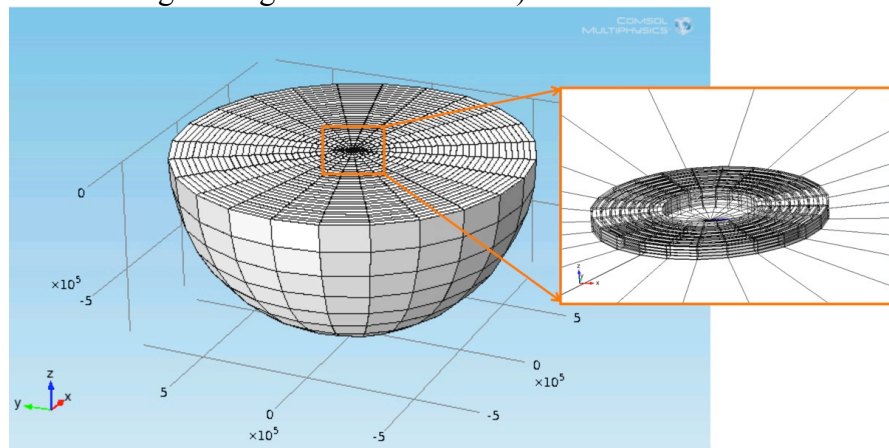
(b) 3D view of the meshing (latitudinal element divisions is 24).
Figure 5.16. Modeling of CING geometry with element with Matched Layer (ML).

Figure 5.17 shows the cross-sectional picture of the simulated von-Mises stress in the wineglass mode for a device with an anchor radius (AR) of 1mm, outer radius (R) of 2.5mm, ring thickness (T) of 30μm, and height (H) of 300μm. The Q_{anchor} based on the eigenvalue is roughly 50 million. Change in the number of rings has negligible effect on Q_{anchor} since the ring does not change the stress profile at the anchor of the device. The Q_{anchor} is analyzed for different anchor radii, ranging from 500 to 2000μm. The rest of the geometry parameters are held constant at outer radius (R) of 2500μm, height (H) of 300μm, and the anchor thickness (AT) of 100μm. From the simulation, all of the geometries produce Q_{anchor} above 10 million. From the analysis results, the anchor loss is

not expected to limit the overall Q of the CING. The accuracy of the current analysis, however, may be limited by the density of the mesh.
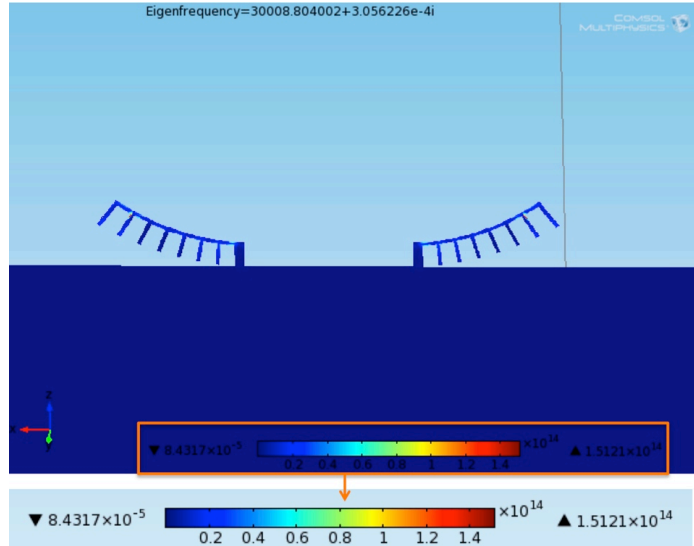

Figure 5.17. Von Mises stress plot of the cross-section of the CING in the wineglass mode. The stress concentration at the boundary region is found to be negligibly smaller than the stress within the geometry.

5.3.3. Surface Loss

The rough surface of the device can be approximated by a thin layer with a certain damping parameter surrounding the rest of the device, which can be considered completely elastic. The $Q_{surface}$ is the ratio between average stored energy over the entire geometry divided by the energy lost from the damaged layer over an oscillation cycle [117, 118]. The surface loss an arbitrary-shaped gyroscope can be simulated using Comsol. Figure 1.18 shows a Comsol model of a hemispherical shell resonator, consisting of a perfectly elastic layer and a damaged layer with complex moduli of $E_{elastic}$ and $E_{elastic} + jE_{anelastic}$, respectively. The thicknesses of the elastic and damaged layers are t and δ, respectively. The $Q_{surface}$ can be calculated from the complex eigenvalue of this model. For flexural mode resonators, the $Q_{surface}$ is expressed as:

$$Q_{surface} \propto \frac{t}{E_{anelastic}\delta} \qquad \text{(Equation 5.13)}$$

Note that $Q_{surface}$ is determined sorely from t-to-δ ratio and $E_{anielastic}$. When surface damping dominates the overall Q of a gyro, the measured Q will be linearly proportional to t-to-δ ratio. In the case of the CING, the largest stress concentration is found at the bottom plate, and the surface roughness of the bottom plate makes the largest contribution to $Q_{surface}$. The $Q_{surface}$ of the CING can be increased by polishing the bottom surface using CMP and by increasing bottom plate thickness (BT).
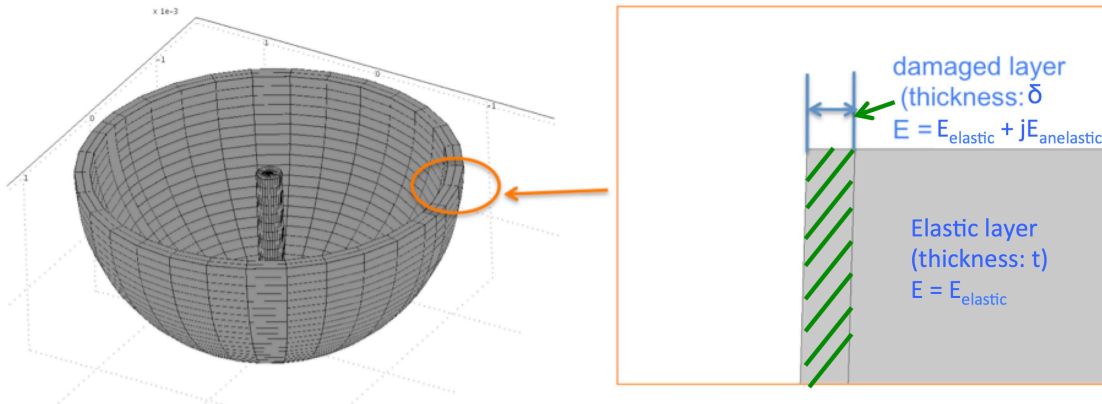

Figure 5.18. Comsol model of hemispherical shell resonator, where perfectly elastic layer (thickness: t, elastic modulus: $E_{elastic}$) is surrounded by damaged layer (thickness: δ, complex elastic modulus: $E_{elastic} + jE_{anelastic}$).

5.4. Three-Dimesional Si-On-Glass (SOG) Process

The process steps of the Si-on-Glass (SOG) process, used to create the CING, are described in Figure 5.19. The process begins with defining the geometry of the resonator and the electrodes using DRIE of a p-type ($\rho < 0.005\Omega$-cm), (111), 550µm-thick Si wafer. The bottom surface of the Si wafer is covered with 2000Å PECVD oxide protection layer. As a masking material, 15µm-thick AZ9260 is used. The photoresist was soft-baked on a 110°C hotplate for 4 minutes. The PR is exposed by an I-line ($\lambda=$

365nm) stepper (GCA Autostep). The conventional developer for AZ9260, diluted AZ400k, induced stress in the PR layer causing it to peel off the PR mask for the thin rings during the developing step. This problem is solved by using MIF300 or MIF319 developer instead of AZ400K. An optimal developing speed and near 100% yield is achieved by dividing the developing process into four steps, consisting of 1) first hydration (30 minutes), 2) first developing (5 minutes), 3) second hydration (10 minutes), and 4) second developing (~5 minutes). Due to the high aspect ratio of the PR patterns, drying between the first and the second developing steps is avoided to ensure hydration of the PR. In case there is thin PR layer left at the bottom of the trenches, the wafer is briefly descumed in O_2 plasma. The SEM of the patterned photoresist, with mask opening sizes of 2μm and 5μm, are shown in Figure 5.20.
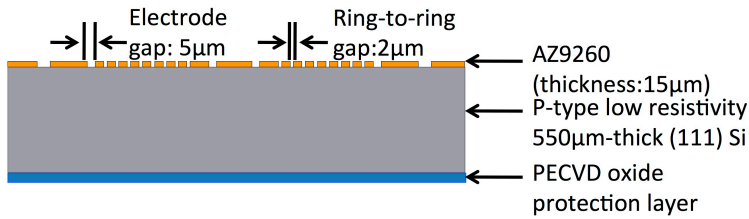
The wafer is then etched in a SPTS Pegasus 4 DRIE machine. Compared to the older-generation STS DRIE machines, this machine provides superior wafer cooling by clamping the wafer using electrostatic force instead of mechanical clamping. The machine also provides more stable etch rates by keeping the chamber at an elevated temperature (120°C) to prevent the deposition of the passivation polymer on the chamber walls which prevents unwanted re-deposition of that polymer on the wafer during the normal etching process. The machine also provides both high-and low-frequency ICP, reducing the footing effect. After 150 minutes of etching, the depths found for 2μm and 5μm openings are measured to be 300μm and 370μm, respectively. An etch aspect ratio of 1:75 to 1:87 is achieved. The DRIE masks are stripped in PRS2000, and the Si wafer is further cleaned in the Piranha solution ($H_2SO_4:H_2O_2 = 1:1$) for more than 30 minutes.

The backside oxide protection layer is then etched using BHF. The wafer is then rinsed in DI water for about 30 minutes.

The glass substrate is a 550μm-thick glass wafer (borofloat33 from PlanOptiks). Recesses with a depth of 3μm are defined and the wet etching is done in straight HF (49%) with a stack of Cr (1000Å) and AZ9260 (15μm) as an etch mask. After etching, the masks are removed, and the glass wafer is etched in BHF for about 30 seconds to remove the thin layer of Cr residue remaining on the surface of the wafer. Then Cr/Pt (100Å/700Å) electrodes and electrical leads are patterned using the liftoff method. The glass and Si wafers are then aligned and bonded with a Karl-Suss SB6E machine in vacuum. A bonding temperature of 400°C and bonding voltages of -500 and -1300V are used for the first and second phases of the bonding process. A bonding misalignment of less than 5μm is achieved.

The bonded wafer is mounted on a supporting substrate using SPI Crystalbond555. The wafer is then etched using the SPTS Pegasus 4 machine to release the gyro structure. Due to the large etch area and thermal insulation by the thick glass wafer, there is considerable lateral etching during the final releasing step (step (e)) when a fast-releasing recipe was used. To prevent excessive heating, the etch rate of the recipe in step (e) is set to be ~4μm/min. The etch depth is calibrated to etch the bottom plate thickness (BT) to be less than 40μm. After the release etching, the wafer is cleaned using high-pressure, low-bias O_2 plasma to remove the passivation layer deposited on the sidewalls. The natural oxide on the wafer from the O_2 plasma step is removed with RIE. The wafer is etched briefly in XeF_2 (pressure: 3Torr, etch time per cycle: 20 seconds, number of cycles: 20) to remove thin Si filaments that were left at the edge of the electrode due to
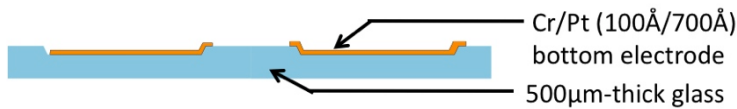
the passivation polymer. The wafer is also annealed at 400°C in vacuum for about 1 hour to remove the polymer and reduce residual stress. The wafer is then cooled down at a rate of 2°C/min to minimize thermal shock to the device. The top-side and cross-sectional SEM pictures of the fabricated CING are shown in Figures 5.21 and 5.22.

Electrode gap: 5μm   Ring-to-ring gap: 2μm

AZ9260 (thickness:15μm)
P-type low resistivity 550μm-thick (111) Si
PECVD oxide protection layer

(a) Pattern DRIE PR mask on a 550μm P-type (111) Si wafer. The gap between ring and ring is 3μm narrower than the gap between ring and electrode.
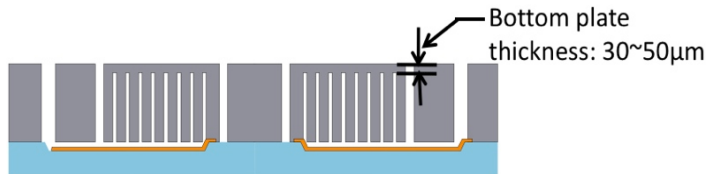
Etch depth: 350μm (for 5μm-opening)
DRIE lag: ~80μm
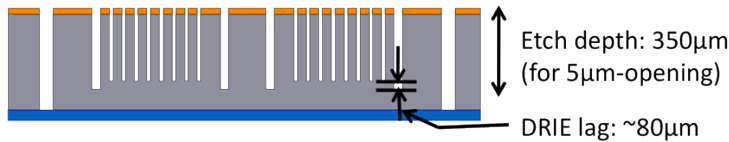
(b) Define DRIE trenches, use DRIE lag to form bottom 80μm-thick bottom silicon.

Cr/Pt (100Å/700Å) bottom electrode
500μm-thick glass

(c) Etch 3μm recess in borosilicate wafer, form bottom Cr/Pt electrodes.
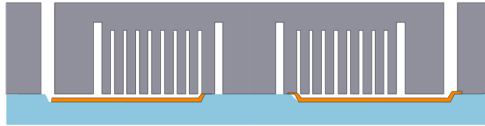
(d) Si and glass wafers are anodically bonded.

Bottom plate thickness: 30~50μm
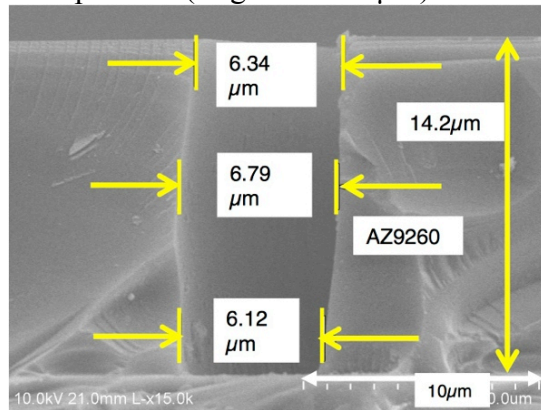
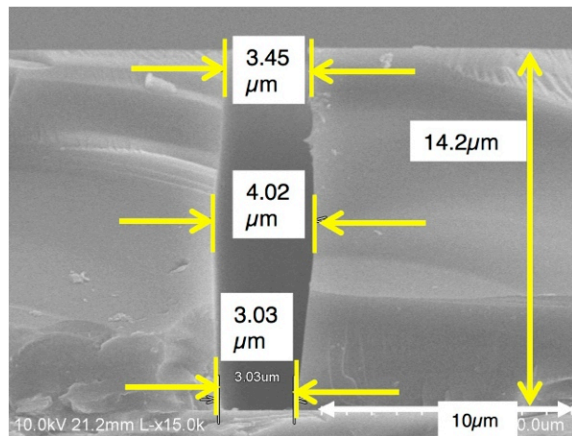(e) Etch Si backside, leaving 30~50μm at the bottom of the cylinder.

Figure 5.19. Silicon-on-Glass (SOG) process for the Cylindrical Rate-Integrating Gyro (CING).
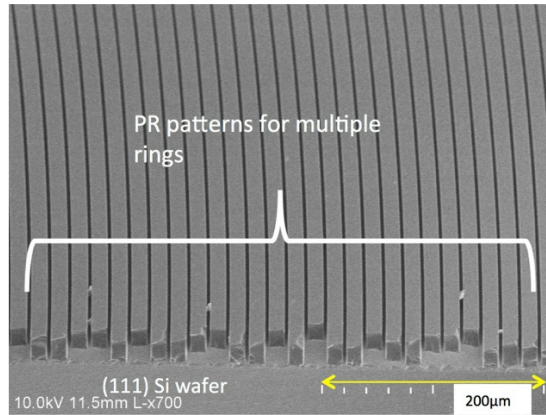
(a) SEM picture of 9260 patterns (ring width: 15µm).

(b) Cross-sectional view of 6µm-wide opening (between electrode and ring). Original mask opening size is 5µm.

(c) Cross-sectional view of 3µm-wide opening (between ring and ring). Original mask opening size is 2µm.

Figure 5.20. SEM pictures of AZ9260 patterns used to pattern the CING. The photoresist is exposed using I-line stepper and developed in MIF319 or MIF 300 developer. The thickness of the pattern is 14.2µm, and the opening sizes between ring and electrode and rings are 6.12µm and 3.03µm for mask opening sizes of 5 and 2µm, respectively.
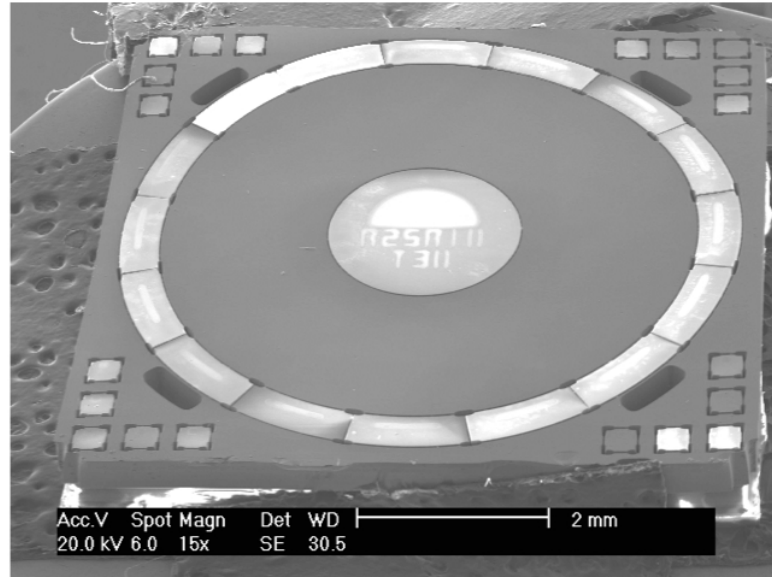
Figure 5.21. SEM picture of the first-generation CING. The device measures outer (R) and anchor (AR) radii of 2.5mm and 1mm, respectively, ring thickness (T) of 30~40µm, bottom plate thickness (BT) of 30~50µm, and height (H) of 300µm.
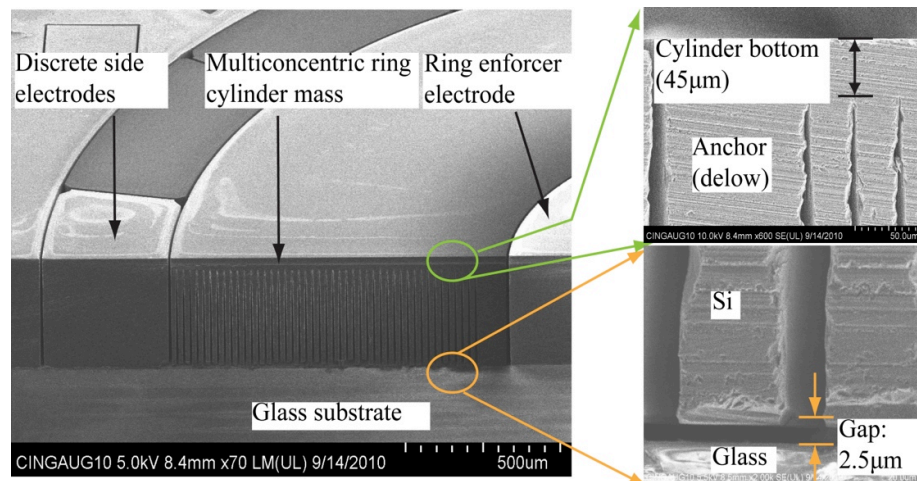
Figure 5.22. Cross-sectional SEM picture of first-generation silicon-on-glass (SOG) CING after dicing. The bottom plate thickness (BT) is 45µm, and the capacitive gap between the mass and the glass is 2.5µm.

5.4.1. Characterization of Anodic Bonding Process

Due to the high-aspect-ratio pre-patterned features on the Si wafer, the conventional bonding recipe at 300°C, used in the SOG process of the BOG, did not produce strong-enough bonding. Figure 5.23 shows a photograph of the Si-glass bonding interface of the

167

CING, bonded at 300°C with a voltage of -1300V, after manually separating the Si layer from the glass layer. The picture shows that anodic bonding occurred only at a part of the side electrode, with a preferential direction. The boundary and the pads for the bottom electrodes are also only partially bonded. Figure 5.24 shows a photograph of the Si-glass bonding interface of the CING, bonded at 400°C with a voltage of -1300V, after manually separating Si layer from the glass layer. Significant improvement in the bonding quality is found by increasing the temperature to 400°C.

The yield from the DRIE releasing step is found to be limited by the residual stress of the bonded wafer. Wafers without proper annealing and slow temperature ramp-down are cracked during the release step by the thermally-induced stress due to the etch heat. Significant increase in the releasing yield is found after introducing an annealing step at 400°C for more than an hour and reducing the cooling-down rate to 2°C/min.
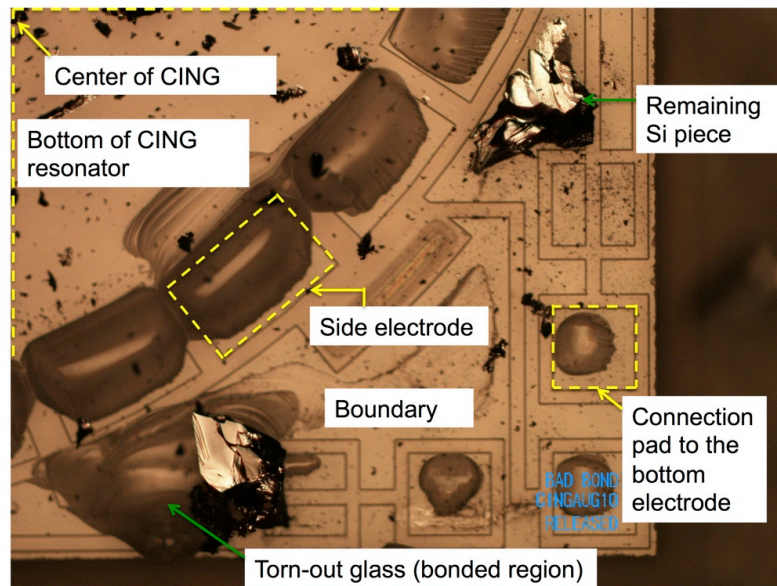

Figure 5.23 Anodic bonding interface of 550µm-Si and 500µm-thick glass bonded at a voltage of -500/-1300V at 300°C, indicating weak bonding strength (Si and glass are separated after the end of fabrication).
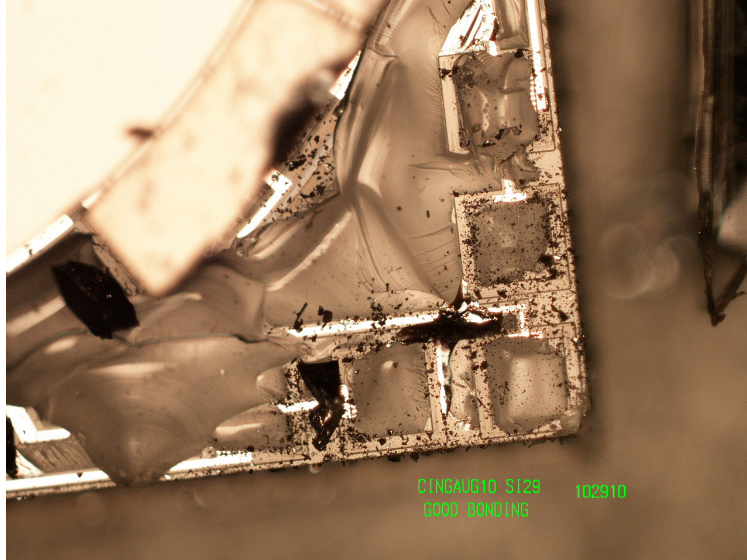
Figure 5.24. Bonding interface of 550μm-Si and 500μm-thick glass bonded at a voltage of -500/-1300V at 400°C, indicating strong bonding strength (Si and glass are separated after the end of fabrication).

5.5. Device Evaluation

5.5.1. Modal Characteristics

The modal characteristics of the first-generation CING are measured at <5mTorr at room temperature (uncontrolled). The side electrodes are used to drive and sense the modes, and the bottom electrodes are used to balance the stiffness axis and perfectly match the resonance frequencies. The two-channel gain-and-phase analyzer presented in [119] is used to simultaneously sense the gyro along both principal axes, which are separated by 45 degrees. Among the tested devices (~100), the average mode separation ranged from 50~150Hz. The smallest mode separation measured is 7Hz. The Q of the gyros ranged from 20,000 to 70,000.

5.5.2. Mode Tuning

The resonance frequencies of the two wineglass modes are electronically matched by applying DC voltages to the electrodes, following the method in [7]. The resonance

frequency of the CING is constantly evaluated by actuating from two axes (separated by 45°) and measuring the capacitance change along the same axes. Electric bias is applied to the balancing electrode, located in the middle of the actuation-and-sensing axes at 22.5°, until the output amplitude from each axes due to an off-axis force is minimized. This is the condition when the principal axes are aligned to the two transduction axes. When the stiffness axes are aligned to the transduction axes, the resonance frequencies of the modes can be individually controlled with the bottom electrodes along the respective axes. By applying DC bias to the axis of the larger stiffness, the modes are matched within 3dB frequency. Figure 5.25 shows the mode matching of the CING, with a matched Q of 21,800. Due to non-ideal cross axis effects of the balancing and tuning biases, the tuning is performed iteratively to achieve the minimum mode separation.

The CING is tested in closed-loop mode. Figure 5.26 shows the architecture of the interface circuitry [119, 120]. The front-end circuitry consists of TL082 JFET amplifier with a feedback resistance of 1MΩ, with additional signals to buffer driving signals and output signals of the transimpedance amplifier (TIA). The digital control circuitry is implemented in a Universal Software Radio Peripheral (USRP) FPGA. The digitally converted sense signals are demodulated with in-phase and quadrature reference signals, and the system calculates the phase, rate-feedback, quadrature-feedback, and amplitude-controlling signals. The amplitude control signal is modulated and sent to the driving axis. The rate-feedback and quadrature control signals are modulated using in-phase and quadrature reference signals, respectively, and sent to the sense axis. The phase signals are used to calculate the delay, and the delay signal is applied to the reference signal.
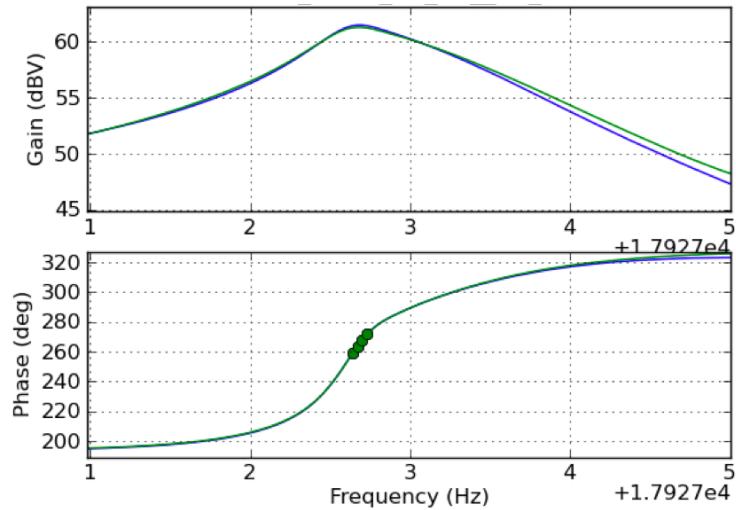
Figure 5.25. Frequency and gain plots of matched $n=2$ wineglass mode peaks of the CING at 17.9kHz.
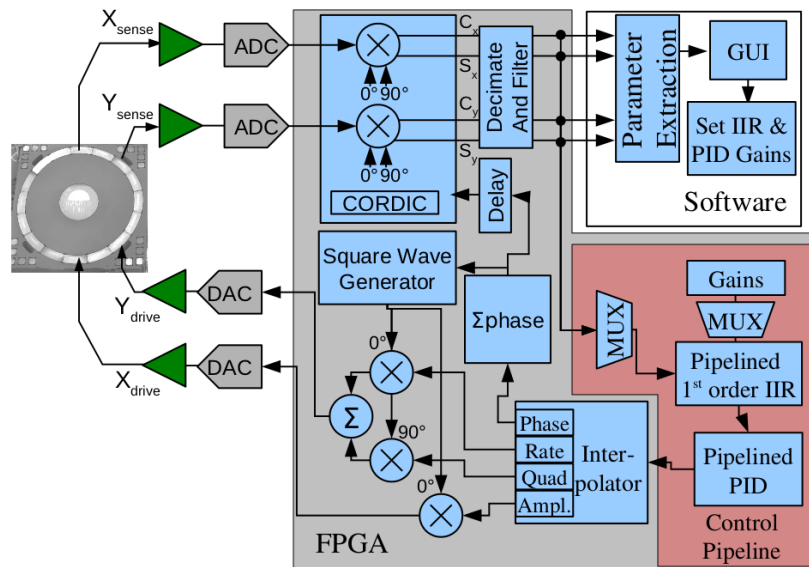
Figure 5.26. Rate-sensing mode control circuitry implemented in FPGA [119].

The testing is done for a gyro sample operating at nominal frequencies of 15,695.1 and 15,695.6Hz, shown in Figure 5.27. Based from the phase shift measured at the driving and the sensing mode, the Q of the two modes at this condition are about 8,865 and 8,889, respectively. The corresponding decay time constant is 0.18 seconds.

The angular gain (A_g) of the device is evaluated from the ratios of amplitudes for actuation and force feedback under different rotation rates [7]. The Coriolis force for a

n=2 wineglass gyro is expressed using effective mass (M), driving velocity amplitude ($\dot{q}_{drive}$), A_g, and a rotation rate (Ω_z) as:

$$F_{Coriolis} = 4MA_g\dot{q}_{drive}\Omega_z \qquad \text{(Equation 5.14)}$$

In the force feedback mode, the A_g is related to the feedback force ($F_{feedback}$) to counterbalance the $F_{Coriolis}$ as:

$$A_g = \frac{F_{Feedback}}{4M\dot{q}_{drive}\Omega_z} \qquad \text{(Equation 5.15)}$$

The relationship between the $\dot{q}_{drive}$ and the voltage amplitude ($E_{control}$) is:

$$\begin{aligned}
\dot{q}_{drive} &= \omega q_{drive} \\
&= \frac{\omega Q_{drive}}{k_{11}} F_{drive} \\
&= \frac{\omega Q_{drive}}{k_{11}}\left(\frac{\varepsilon A_{elec}}{g^2}V_p\right)E_{control}
\end{aligned} \qquad \text{(Equation 5.16)}$$

The feedback force amplitude ($F_{feedback}$) is related to the feedback voltage amplitude ($\theta_{control}$) by:

$$F_{feedback} = \left(\frac{\varepsilon A_{elec}}{g^2}V_p\right)\theta_{control} \qquad \text{(Equation 5.17)}$$

The A_g can be expressed in terms of $\theta_{control}$, $E_{control}$, the damping time in the driving mode τ_{drive} as:

$$\begin{aligned}
A_g &= \frac{\theta_{control}}{4M\Omega_z\left(\dfrac{\omega Q_{drive}}{k_{11}}E_{control}\right)} \\
&= \frac{\theta_{control}}{E_{control}}\frac{1}{2\tau_{drive}\Omega_z}
\end{aligned} \qquad \text{(Equation 5.18)}$$

Figure 5.28 shows the plot between the input rotation rate Ω from -45 to 45deg/s and the ratio between rate feedback amplitude and driving amplitude ($\theta_{control}/E_{control}$). From

the slope of the curve, and with a τ_{drive} of 0.18 seconds, the A_g is calculated as 0.05. This is value is close to the theoretically calculated value of 0.07 using FEM.
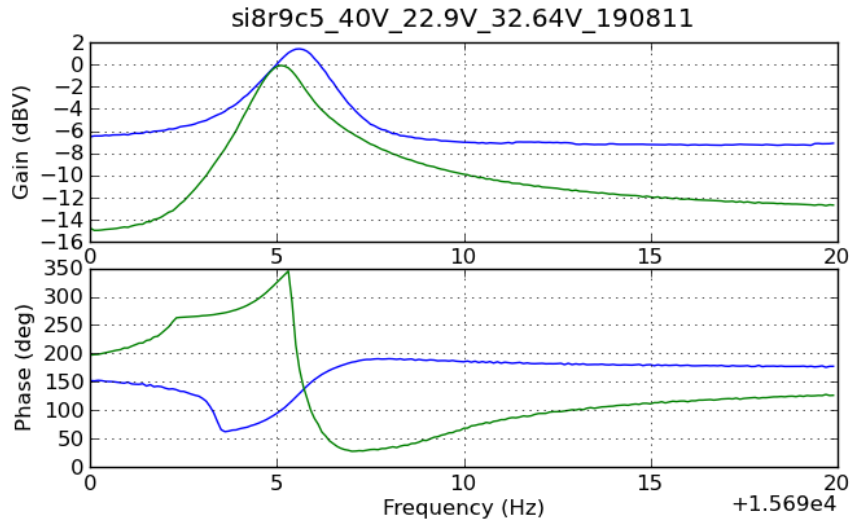
Figure 5.27. Gain and phase plots of slightly mismatched CING, operating at 15695.1Hz and 15695.6Hz and Q of 8865 and 8889.
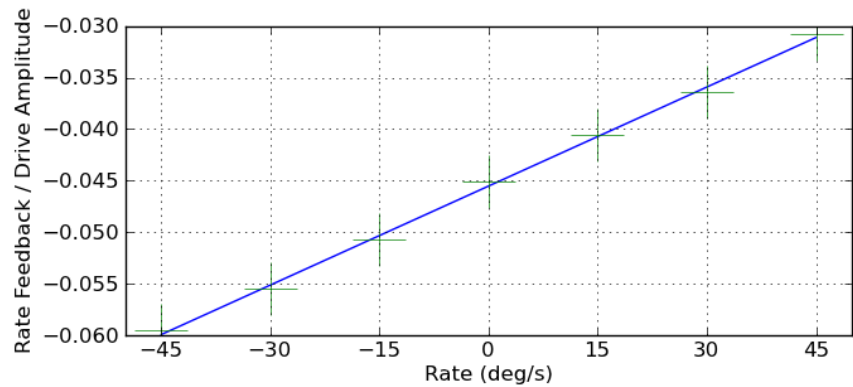
Figure 5.28. Input rotation rate (Ω) and ratio of rate feedback force ($\theta_{control}$) and driving voltage ($E_{control}$). The A_g can be calculated from the slope of this figure and Equation 5.18.

The Allan variance plot of the first-generation CING is shown in Figure 5.29. The bias stability of the sensor is 72deg/hr, and the stability is currently limited by the white noise of the PLL. Figure 5.30 shows the power spectrum density of the white output noise of the sensor. From the graph, the angle random walk (ARW) at 0.1Hz is measured as 7deg/√hr (420deg/hr/√Hz). The output signal of the sensor under rotation rates of -45

173

to 45deg/s with 15deg/s steps is shown in Figure 5.31. The output signal suffers from bias instability of the sensor. The bias stability and ARW are currently limited due to the white noise signal in the phase lock loop (PLL) and small angular gain (A_g). This introduces phase error that creates the bias noise of such level. The small A_g of 0.05 is also responsible for the low resolution, since the scale factor of the rate-mode output is proportional to A_g.
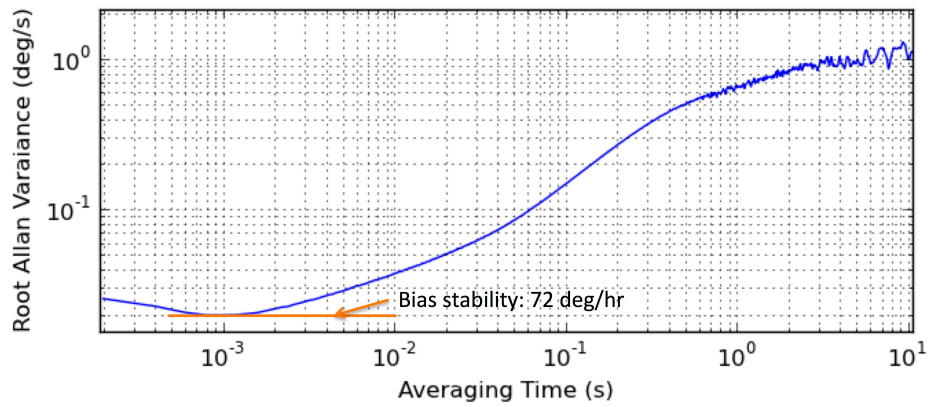

Figure 5.29. Allan variance plot of first-generation CING. Bias stability is 72 deg/hr.
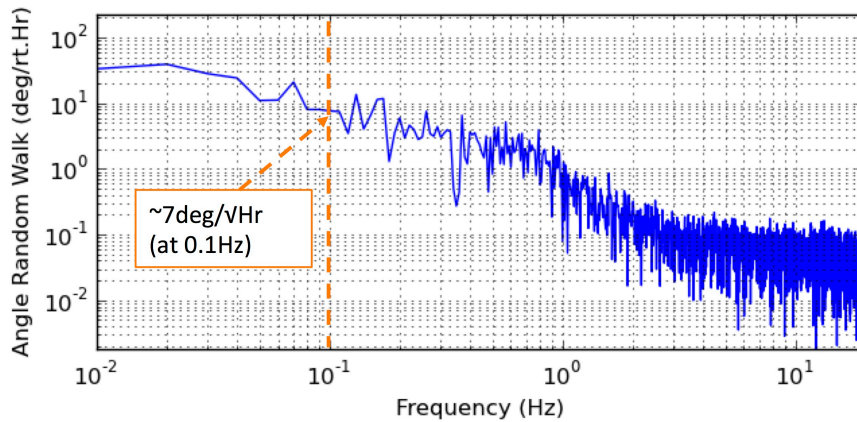
Figure 5.30. Noise power spectrum plot, indicating angle random walk (ARW) of ~7 deg/√hr at 0.1Hz.
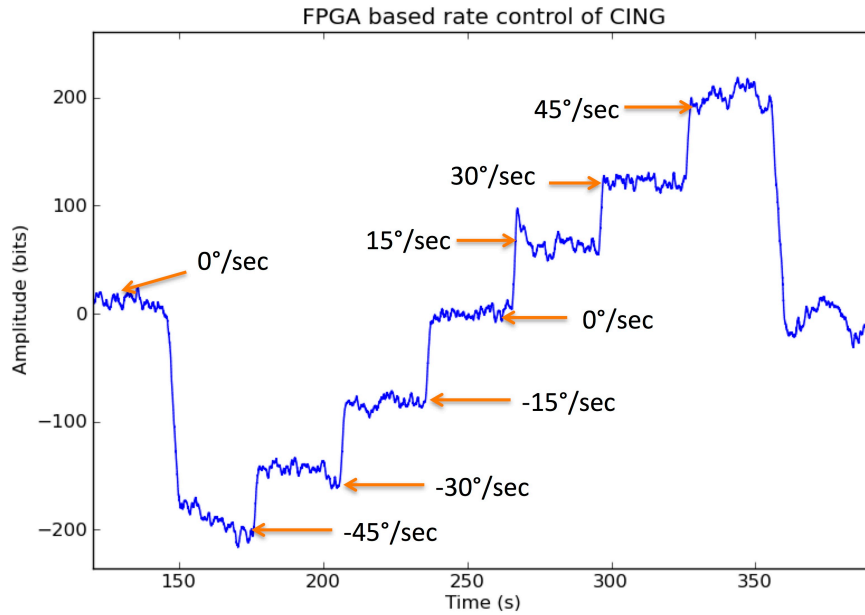
Figure 5.31. Open loop sensor response of the first-generation CING under -45deg/s to 45deg/s rotation with step of 15deg/s.

5.5.3. Rate-Integration Mode (Whole-Angle-Mode) Operation

In the whole-angle mode, the anti-nodal position of the wineglass mode precesses during rotation with an angular gain (A_g). The rotation angle (θ) is found by the arctangent of the ratio of the amplitude of the two wineglass-mode axes, separated by 45 degrees. The architecture of the controlling system is shown in Figure 5.32. The whole angle gyro control is performed following the HRG's control system [88].

The testing is done for the gyro with mode mismatch less than 1mHz, with a matched Q of 21,800 (Figure 5.25). The main reference loop constrains the phase difference between the actuation signals and the output of the transimpedance amplifier (TIA) to be zero. At this phase relationship the CING oscillates at its natural frequency. A software phase-lock-loop (PLL) generates in-phase (i) and out-of-phase (q)

components of the reference signal. The reference signal is used to demodulate the main

amplitude and quadrature amplitude of the CING's oscillation.
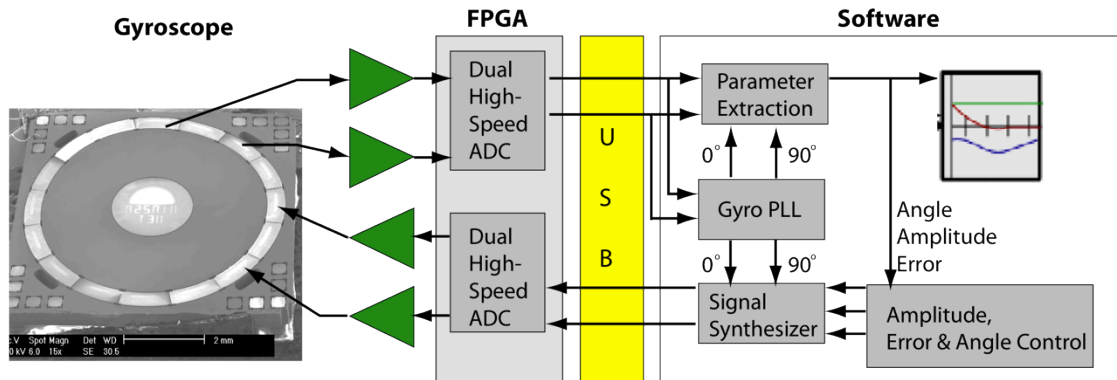
Figure 5.32. Interface/control circuitry algorithm for the whole-angle-mode operation of the CING.

The in-phase and quadrature amplitudes of the vibrational signal measured from the

two axes are used to calculate the overall in-phase amplitude, quadrature amplitude, and

the angle (θ) of the 2-DOF pendulum equation. For the whole-angle mode operation, the

in-phase amplitude is set constant, and the quadrature amplitude is set zero, using a PID

controller, while the drive signals are proportioned to the two axes with the same ratio as

the sense signals, allowing the swinging pattern to precess freely.

The CING is tested for whole-angle-mode operation on an Ideal Aerospace Aero900

rotation table. The CING is directly mounted on the front-end PCB board and wire-

bonded to the sense and drive amplifiers. The output of the frontend circuitry connects to

outside of the rotation table through slip ring electrodes. The gyro is placed at a pressure

of <5mTorr and at room temperature (uncontrolled). Figure 5.33 shows the comparison

of output signal of the interface circuitry as the CING switches from the rate mode and

the whole-angle mode while the sensor is rotated at 15 deg/sec. Before the time point (x-

axis) of 27.8 seconds, the sensor is operated in the rate mode. The recorded rate-

measurement data is shown in red. The measured angular position (blue) and projected

angular position (green), assuming an A_g of 0.3, in the whole angle mode are recorded for a time span of 7.2 seconds. Note that the A_g used for projected angular position does not reflect the real A_g value of the device. The precession angle (θ) follows the direction of the input rotation, but its scale factor does not match the scale factor calculated from the rate-mode operation.

The accuracy of the first-generation CING system is believed to be limited by large loop delay in the PLL which has to be manually cancelled using a software phase-shifter. This issue is solved in the next version interface circuitry by moving the PLL unit into FPGA. The improved interface circuitry is used in the evaluation of the second-generation CING, discussed in the next chapter.

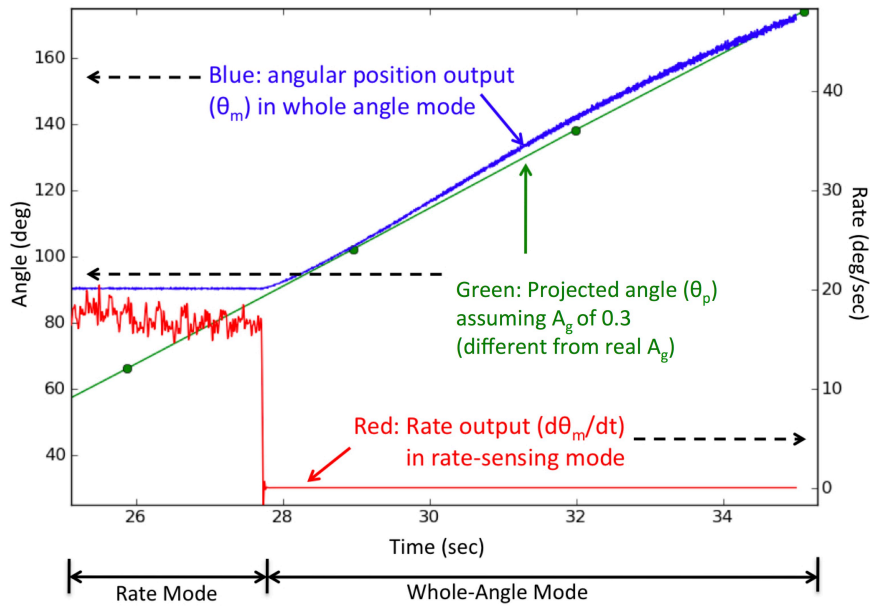Figure 5.33. Switching between rate mode to whole-angle-mode of the first-generation CING. After time point of 27.8 seconds, the gyro is operated in the whole-angle mode. The whole-angle-mode operation is limited by loop delay in the PLL unit.

The bias drift in the angular position ($\dot{\theta}$) in whole angle mode is inversely proportional to the nominal damping time constant (τ_o), so the sensor accuracy will be

improved by increasing τ_o. The τ_o (= $2Q/\omega$) can be improved by lowering ω and increasing Q. As we discussed earlier in this section, due to large thermal conductivity of Si, lower thermoelastic damping (TED) is achieved as ω is lowered. The second-generation CING, which will be discussed in Chapter 6, has 6 times lower frequency than the first-generation (f_{WG}: 3000Hz) and achieves 25 times increase in the τ_o. However, a shortcoming of this approach is reduction in angular gain (A_g) due to decrease in the aspect ratio.

5.6. Summary and Conclusion

Axisymmetric gyros are advantageous for rate-integrating gyroscopes (RIG) because of innate isotropy in stiffness and damping. The Cylindrical Rate-Integrating Gyro (CING) offers complete axisymmetry, self-alignment of the resonator with anchor and electrodes, and a large ratio between parasitic and the wineglass mode frequencies ($f_{parasitic}/f_{WG}$), leading to better vibration insensitivity. A challenge of the CING is a small angular gain (A_g: 0.05) due to a low aspect ratio. From FEM simulation, the A_g of the sensor improves up to a maximum value of 0.3 as the aspect ratio reaches 1.

The first-generation CING is fabricated using the Si-on-glass (SOG) process with 550μm-thick (111) Si substrate. The gyro measures a radius (R) of 2.5mm, anchor radius (AR) of 1mm, height (H) of 300μm, ring thickness (T) of 30~40μm, and bottom plate thickness (BT) of 30~50μm. The Q (~22,000) is limited by thermoelastic damping (TED), which is calculated to be ~30,000 at 22kHz. The largest TED loss occurs from the bottom plate.

The CING is tested in rate- and rate-integrating modes using digital interface circuitry. The CING measured an A_g of 0.05, similar to the simulated value of 0.07. A

frequency mismatch (Δf) of <1mHz is demonstrated, and a mode-matched Q 21,800 is found. An angle random walk (ARW) of 7deg/$\sqrt{Hr}$ and a bias stability of 72deg/hr are measured. The large bias stability is attributed to the white noise in the phase lock loop (PLL) adding phase noise to the system. The whole-angle mode operation is limited by large delay in PLL in the software-defined radio.

In the next chapter we describe the design, fabrication, and evaluation of the second-generation CING with lower f_{WG} (3kHz), increased τ_o, and reduced initial mode mismatch. The design and test results of the first-generation CING are summarized in Table 5.5.

Table 5.5. Design and test summary of first-generation CING

Geometry and Electrical property		Calculated Physical Parameters		Test Results (gyro with T=30µm)	
Outer radius (R)	2.5mm	Wineglass freq. (f_{WG})	17.3kHz (T=30µm)	f_{WG} ($\Delta f/f$)	17.9kHz (0.58%)
Anchor radius (AR)	1mm	Tilting mode freq. ($f_{tilting}$)	>30kHz	Angular gain (A_g)	0.05 (force feedback mode)
Ring thickness (T)	30µm, 40µm	Vertical mode freq. ($f_{vertical}$)	>50kHz	Q ($\Delta 1/\tau$)	21,800 (0.0047Hz) (under exact matching)
Anchor thickness (AT)	100µm	Effective mass (M)	~700µg	Angle Random Walk (ARW)	7deg/$\sqrt{Hr}$ (force feedback mode)
Bottom plate thickness (BT)	30~50 µm	Angular gain (A_g) (ANSYS)	~0.07	Bias stability	72 deg/hr (force feedback mode)
Height (H)	300µm	Q_{TED} (ANSYS)	~30,000 (at 22kHz)	Rate-integrating mode operation	Limited by delay in PLL block
Side electrode capacitance (gap: 9µm)	290fF	Q_{anchor} (Comsol)	>1million (with axisymmetry)		
Bottom electrode capacitance (gap: 2.5µm)	3.7pF				

CHAPTER 6.

LOW-FREQUENCY SINGLE-CRYSTAL-SILICON CYLINDRICAL RATE-INTEGRATING GYROSCOPE (CING)

The motivation of the development of the low-frequency CING is to increase the nominal damping time (τ_o) and take advantage of better innate mode frequency matching. This chapter discusses on the mechanical design, fabrication, and testing of the second-generation (3kHz) CING in both rate- and rate-integrating modes using digital interface circuitry.

6.1. Design of Low-Frequency CING

In the first-generation CING we are able to partially verify the whole-angle-operation of the CING. In the second-generation CING, we aim to achieve a larger nominal decay time constant (τ_o), which leads to smaller bias drift from damping anisotropy by lowering the wineglass mode frequency (f_{WG}) to be about 3kHz by increasing the radius of the device and by increasing the Q. A drawback of this approach is reduction in the angular gain (A_g), because the A_g is related to the aspect ratio (height / radius) of a device. However, a CING with a longer τ_o can be still useful for the development of the necessary whole-angle-mode readout and control system. Due to the increase the effective mass (M) and reduction in the effective stiffness (k), we expect smaller nominal frequency gap between the f_{WG}.

The second-generation CING has the same basic structure as the first-generation CING. In order to reduce sensitivity to external noise and to have larger shock resistance, the stiffness ratio between parasitic modes ($f_{parasitic}$) and the f_{WG} should be maximized. The two in-phase modes located near f_{WG} are the tilting mode ($f_{tilting}$) and the vertical mode ($f_{vertical}$). The four design parameters for frequency engineering are outer radius (R), anchor radius (AR), thickness of ring (T), and ring height (H). Figures 6.1(a)-(c) show the relation between f_{WG}, $f_{tilting}$, and $f_{vertical}$ with these parameters, calculated using ANSYS. Both AR and T affect the stiffness of the bottom plate. As T increases, the stiffness of the bottom plate starts to level off, so the resonance frequencies start to level off. The f_{WG} is determined mostly by R with a negligible dependency on AR. As H increases from 100μm to 500μm, the CING changes from a disk-like structure to a cylinder-like structure. When the CING behaves similarly to a disk, its flexibility is dominated by the flexibility of the bottom plate. Thus, as H increases, the stiffness of the bottom plate increases. As H passes a transition point (300μm), the flexibility of the rings starts to counteract the bottom plate stiffness. For a device with R of 6mm, $AR >$ 1.5mm, and $T > 20$μm, with an operating frequency of 3kHz, $f_{parasitic}/f_{WG}$ of as high as 1.8 can be achieved. The geometry of the low-frequency CING is selected to have $f_{WG} <$ 3kHz and have $f_{tilting}$ and $f_{vertical}$ located above f_{WG} by 1~2kHz. The dimensions of the CING are provided in Table 6.1.

The Q_{TED} of the CING is calculated the same method that is described in Chapter 5. The model is approximated to have 50 concentric rings, which is 1/4 of the actual number of the multiple rings in the gyro. Therefore, the accuracy of the simulation is limited by the geometrical complexity of the gyro. From this model, a Q_{TED} of 129,000 is calculated

at f_{WG} (3kHz), which corresponds to a nominal decay time constant (τ_o) of ~13.7 seconds. At f_{WG} the largest temperature variation is found across the vertical sidewall of the gyroscope (Figure 6.2). The thermal dissipation coefficient (τ_h) associated with conduction in the height direction ($b = 320\mu m$) is found using Equation 5.7 as:
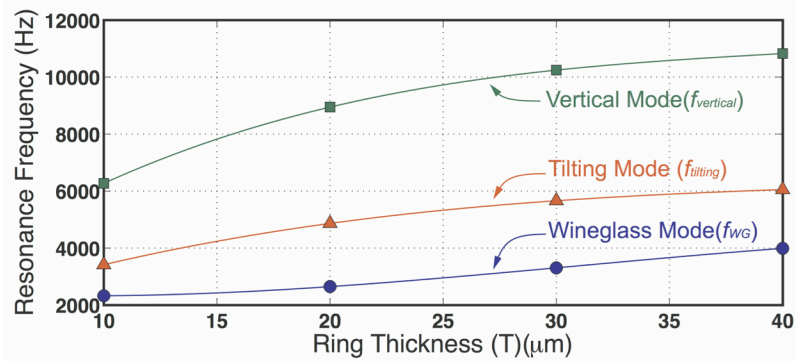
(a) Dependency on ring thickness (T) [radius R: 6mm, anchor radius AR: 1.5mm, height H: 300μm, gap between rings G: 2μm, bottom plate thickness BT: 30μm]
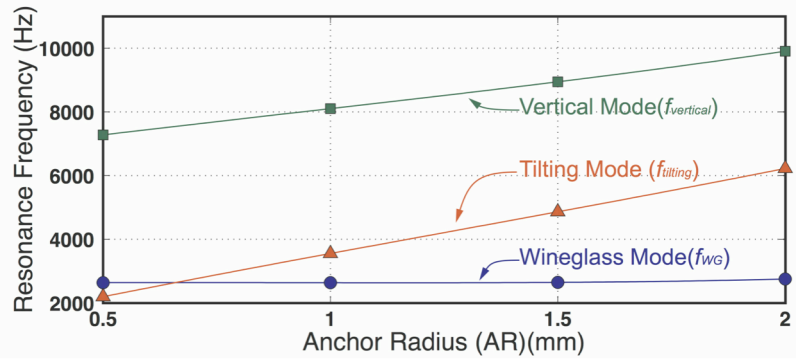
(b) Dependency on anchor radius AR [R: 6mm, T: 20μm, H: 300μm, G: 2μm, BT: 30μm]
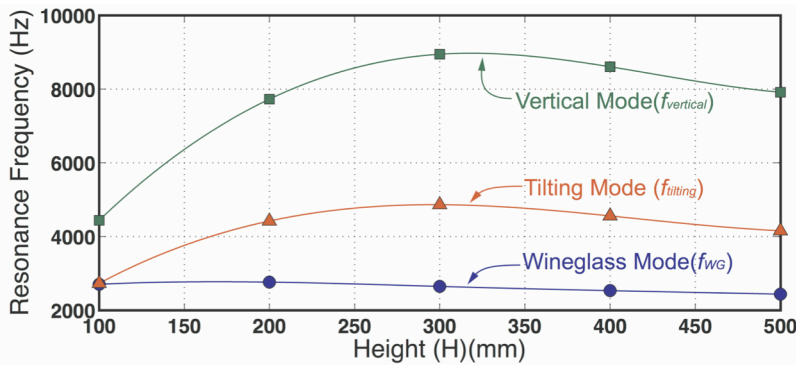
(c) Dependency on height H [R: 6mm, AR: 1.5mm, T: 20μm, G: 2μm, BT: 30μm]

Figure 6.1. Dependence of the wineglass mode (f_{WG}), tilting mode ($f_{tilting}$), and vertical mode ($f_{vertical}$) frequencies on the geometry of low-frequency CING.

$$\tau_h = \frac{h^2}{\pi^2 \chi_{Si}}$$

$$= 10^{-4}(\text{sec})$$

(Equation 6.1)

The Q_{TED}^{-1} reaches to maximum at the frequency ω_h that satisfies the condition $\omega_h \tau_h = 1$ [106], which yields f_h of 1.5kHz. Since the second-generation CING is flatter than the first-generation CING, the gyro has more vertical motion, and because of this, the stress on the sidewall of the gyro becomes more significant.

Table 6.1. Geometry, electrical properties, and physical properties of the 2nd generation CING

Geometry and Electrical Property		Calculated Physical Property	
Outer radius (R):	6mm	Wineglass mode frequency (f_{WG})	3kHz
Inner radius (AR)	1.5mm	Tilting mode frequency ($f_{tilting}$)	5kHz
Anchor width (AT)	100µm	Vertical mode frequency ($f_{vertical}$)	9kHz
Ring width (T)	20µm	Q_{TED} (ANSYS)	129,000 (τ_o=13.7sec)
Bottom plate thickness (BT)	20µm	Effective mass (M) (ANSYS)	4.6mg
Side electrode (Gap: 9µm)	2.6pF	Angular gain (A_g) (ANSYS)	0.03
Bottom electrode (Gap: 5µm)	10pF		

(a) side view (b) bottom view
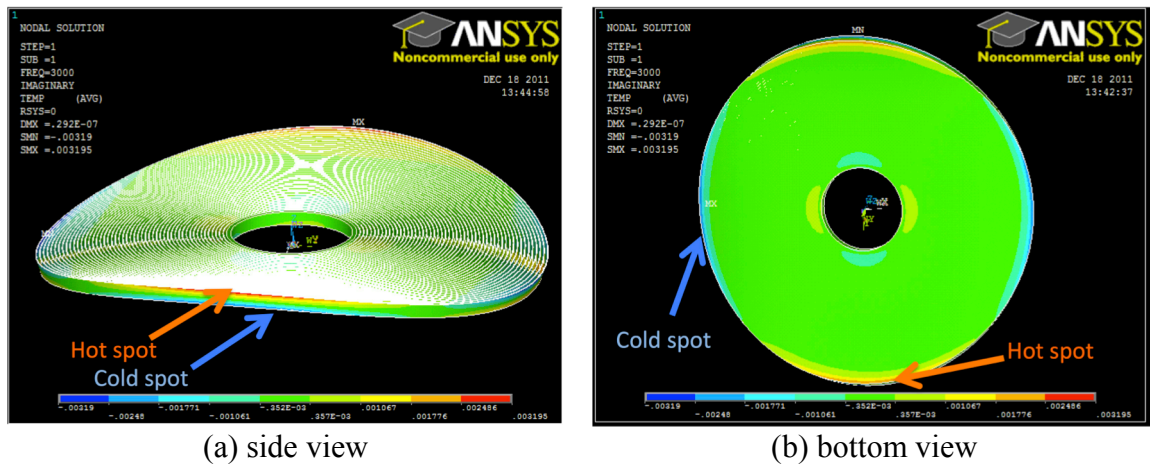
Figure 6.2. Temperature profile of second-generation CING from TED simulation. The largest temperature gradient is found between the top and bottom edges of vertical sidewalls from stress developed during flexing of the sidewalls.

6.2. Si-On-Glass (SOG) Process for Low-Frequency CING

The low-frequency CING is fabricated using the same Si-on-Glass (SOG) process that is developed for the first-generation CING. The glass recess depth is set to 5µm to prevent the pull-down of Si wafer to glass during anodic bonding and to prevent the touch-down of the released gyro to the glass substrate due to stress created from mismatch in the coefficients of thermal expansion (CTE) between glass and Si. The bottom plate thickness (*BT*) set to be <20µm to reduce the TED loss. The fabricated device measures 1.3cm × 1.3cm × 0.6cm (Figure 6.3). The SEM picture the cross-section of the manually cracked CING indicates a bottom plate with a thickness of less than 20µm (Figure 6.4).

6.2.1. Development of Higher-Accuracy Device Releasing Processes

One of the most critical process steps that reduce the yield of the current SOG process is the final DRIE releasing step. Since the low-frequency CING has a large mass size, the device has a smaller thermal diffusivity. During the releasing step using DRIE,
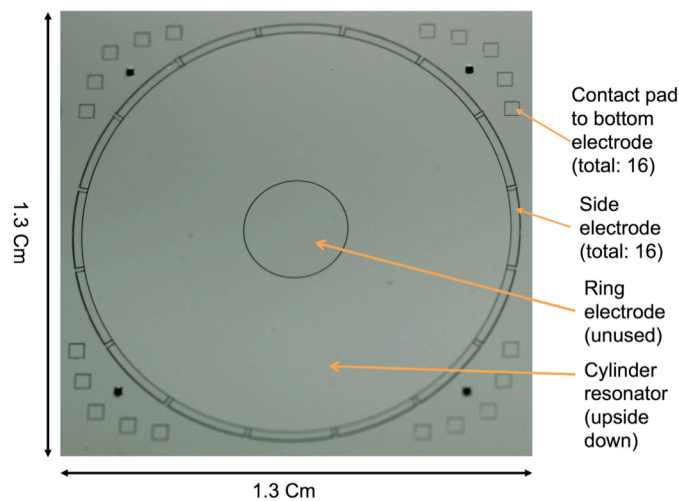
Figure 6.3. Top side photograph of low-frequency CING [radius (*R*): 6mm, anchor radius (*AR*): 1.5mm, height (*H*): ~300µm, operating frequency: 3kHz].

the temperature of the suspended gyro mass becomes high, so the etch rate becomes more difficult to control, and gyros are etched more in the lateral directions. In order to address this issue, two different releasing steps are tested. In the first process, a thick Al layer is used to touch a part of the gyro mass in order to diffuse away the heat. This process is similar to the fabrication process for the Balanced Oscillating Gyroscope (BOG), except that in this case, the Al layer is placed on the glass recess. In the second process, the wafer is released using lapping and chemical-mechanical polishing (CMP). This process is attractive because it is a room-temperature process and that the bottom plate of the gyro is polished when the gyro is released.

Figure 6.5 shows the process steps of the first process. The first two steps are identical to the steps in the original SOG process. In step (c), 20Å-thick Ti (adhesion layer) and >5µm-thick Al is deposited using multiple evaporation runs. The thermal dissipation layers are defined using wet etching, and the height of the layer is adjusted to create a step height between the top of the dissipation layer and the glass surface by less than 800Å. The two wafers are anodically bonded at 400°C, using two voltage steps of -500V and -1300V in a Karl Suss SB6E wafer bonder (step (d)). After the bonding step,
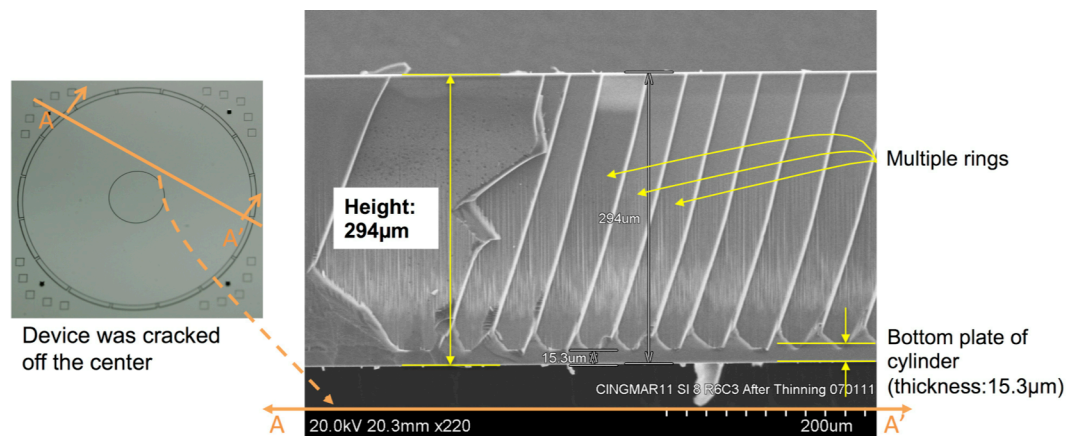
Figure 6.4. Cross-sectional SEM of CING after manually cracking the device. The sidewalls of the rings appear slanted, because the device is cracked off the center.

the wafer is annealed at the same temperature for 2 hours, and the wafer is cooled down slowly (2ºC/min) to room temperature to minimize thermoresidual stress. Then the Si wafer is released using DRIE (step (e)), and the thermal dissipation layer is wet etched with Al etchant (Transene Aluminum Etchant Type A) and Piranha (H_2SO_4:H_2O_2=1:4) solution. The wafer is rinsed and left in IPA or methanol for >5 days, and the wafer is dried on an 115ºC hot plate (step (f)).

With this modified process, significant improvement in the reduction of lateral etching during the DRIE releasing step is achieved. However, during the bonding step (step (d)) the Al-Pt and Al-Si layers reacted and formed intermetallic material. The part of Pt electrode that react with Al is also etched away, and bottom electrodes are disconnected. The Si-Al reaction leaves particles on the surface of the reacted Si, but it does not significantly affect the operation of the sensor. The amount of reaction between and Pt and Al is reduced by a lot by increasing the thickness of the Ti layer up to 2000μm following the study by [121]. However, the thick Ti layer after the annealing cannot be completely etched using conventional Ti etchants such as Piranha, BHF, hydrogen peroxide, and sulfuric acid. The feasibility of this process is thus limited.

Figure 6.6 shows the process flow of the modified releasing step that uses mechanical lapping and CMP process to release the final structure. The first two steps are the same as those in Figure 6.5. In step (c), PECVD oxide (1kÅ) is deposited as a diffusion barrier layer and an Al layer of a thickness of ~5μm is deposited using multiple evaporation steps. Although it has not been tested, it is believed that Ti can replace the PECVD oxide layer. The Al and oxide layers are wet etched, and the top of the Al layer is adjusted to ~3000Å lower than the top of the glass surface to account for the thermal

expansion during the anodic bonding step. In this process, the Al layer does not have to fully contact Al layer is used to vertically support the Si layer during the lapping step and to block the flow of slurries to the recess region, so the Al layer does not have to contact the Si layer. Although it is desirable to have a strong seal between the Al and Si, we avoid it to prevent the intermetallic reaction at 400°C. The two wafers are bonded at 300°C with a bonding voltage of -500V and -2000V (step (d)). Then the device is lapped and polished using IPEC-472 CMP machine (step (e)). Then the wafer is cleaned in the

Etch depth: 350μm
(for 5μm-opening)

DRIE lag: ~80μm

(a) Pattern DRIE recess on p-type (111) Si wafer

Cr/Pt (100Å/700Å)
bottom electrode
500μm-thick glass

(b) Pattern 5 μm-deep glass recess and Cr/Pt 100Å/700Å electrodes

Ti/Al(20Å/>5μm)
Heat dissipation layer

Level of Metal(1)
Level of Glass (2)

0Å < (1) – (2) <800Å

(c) Evaporate Ti/Al dissipation layer with thicknesses of 20Å/>5μm. Pattern the layer using wet etching. Then adjust the level using maskless wet etching in Al etchant.

(d) Anodic bonding at 400°C -500V/-1300V in vacuum. Anneal for 2 hours and cool down to room temperature with a rate of -2°C/min.

Bottom plate
thickness: <20μm

(e) Release the gyro using DRIE.

(f) Release the metal layer in Al etchant and piranha solution (H_2SO_4:H_2O_2 = 1:4). Rinse and dip in IPA or methanol for >5 days. Dry on an 115°C hot plate

Figure 6.5. Modified SOG process flow for including thick Al thermal dissipation layer for DRIE process.

post-CMP cleaner and cleaned in the piranha solution. Then the remaining Al layer is etched in the Al etchant. The wafer is cleaned BHF to remove the oxide layer. The wafer is dipped in methanol or IPA for more than 5 days and dried on the 115°C hot plate (step (f)).

Figure 6.7 shows the topside photographs of the process wafer, taken right after the

(a) Pattern DRIE recess on p-type (111) Si wafer.

(b) Pattern 5 µm-deep glass recess and Cr/Pt 100Å/700Å electrodes.

(c) Deposit PECVD oxide 1kA as a diffusion block layer. Deposit Al layer with thickness of ~5µm using multiple evaporation run. Pattern the layers using wet etching. Then adjust the level using maskless wet etching in Al etchant to have a level of Al slightly lower than the level of glass to account for expansion during the anodic bonding step.

(d) Anodic bonding at 300°C -500V/-2000V in vacuum. Anneal for 2 hours and cool down to room temperature with a rate of -2°C/min.

(e) Release the gyro using mehcanial lapping and CMP.

(f) Clean the wafer using post-CMP cleaner and clean using piranha solution (H_2SO_4:H_2O_2 = 1:4). Remove remaining Al using Al etchant. Rinse and dip in IPA or methanol for >5 days. Dry on the top of 115°C hot plate

Figure 6.6. Modified SOG process flow releasing the CING using mechanical lapping and CMP.

mechanical releasing step. The release quality and the surface quality are found to be good. However, the feasibility of the current process is limited by CMP slurries that remain on the sidewall of DRIE trenches. It is found to be very challenging to clean them using post-CMP cleaning or Piranha cleaning methods.

Figure 6.7. Photograph of CING released using lapping and CMP.
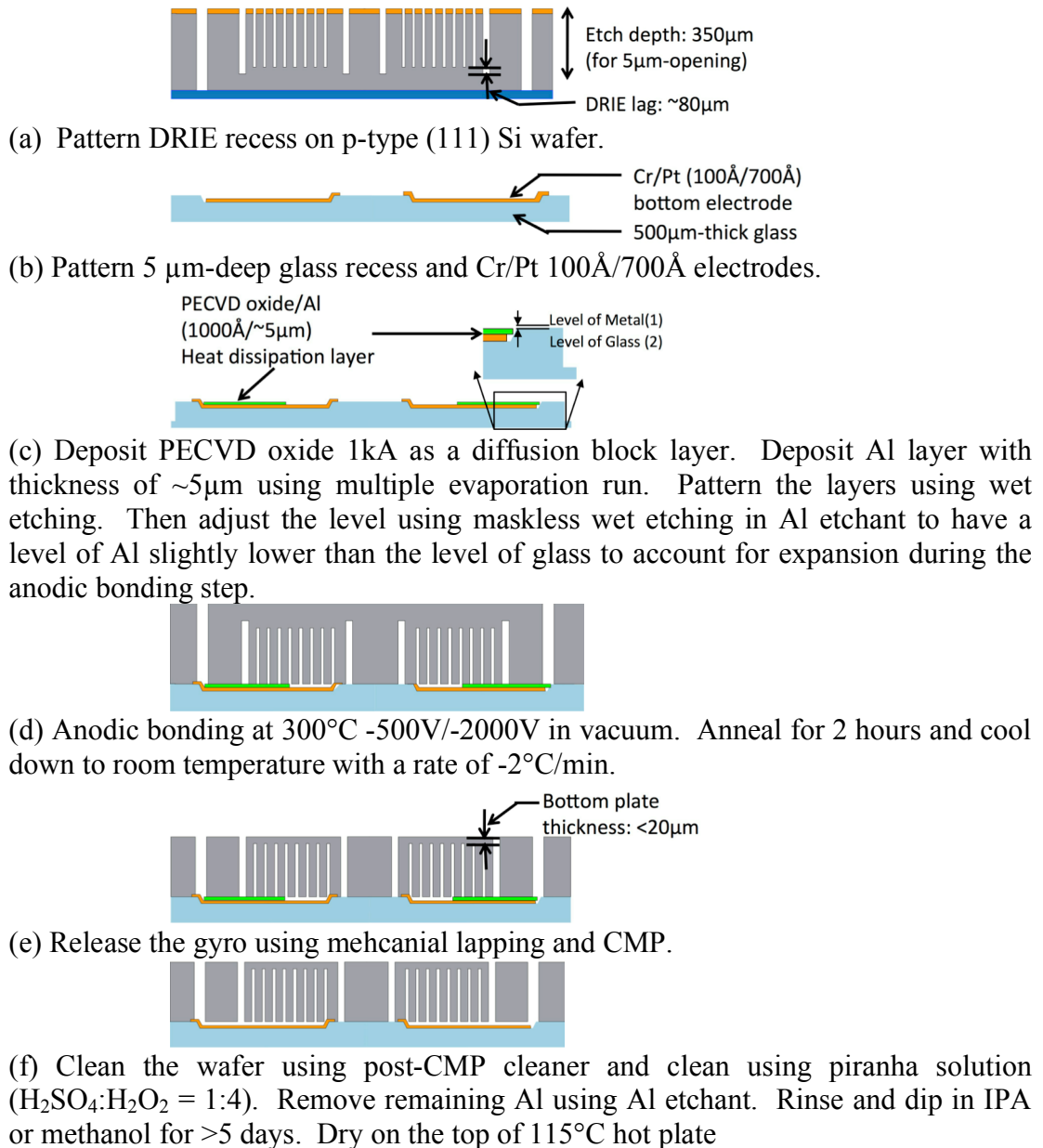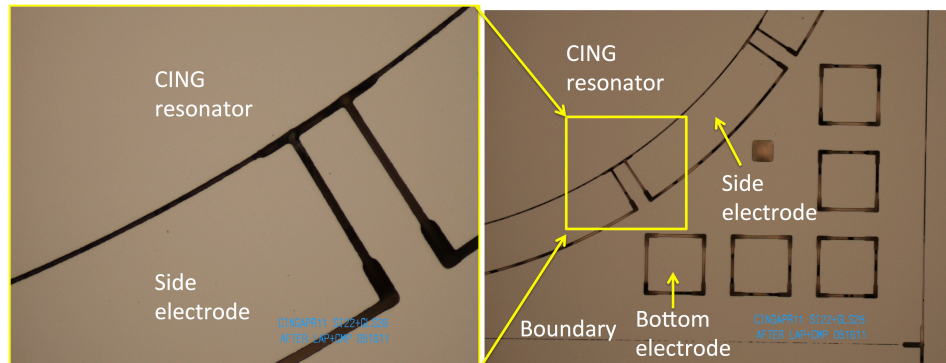
6.3. Evaluation of Modal Characteristics of the Low-Frequency CING

The quality factor (Q) of a large-decay-time (τ_o) resonator is difficult to measure using a conventional gain-phase analyzer, since the ring down of the oscillating amplitude from a previous measurement frequency will overlap the response of the mechanical system under the oscillation frequency. Since the decaying time can be related to Q, it is more accurate to measure the Q from the decay time. The τ_o of the low-frequency CING is measured with a decay-time measurement program, configured using a software-controlled radio. The program is designed by Jeffrey Gregory. Figure 6.8 shows the decay time plots of the CING, recorded using the program. The oscillation is measured using the bottom electrode, with a body bias less than 10V. The wineglass mode frequency of the gyro (f_{WG}) is found at 2995Hz, with a nominal frequency mismatch Δf of 7Hz ($\Delta f/f = 0.2\%$). The nominal decay time of the gyro at unturned state are found as 11.5 seconds ($Q = 108,000$) and 10 seconds ($Q = 94,000$).

189

Figure 6.9 shows the resonance peaks of the wineglass modes, measured using two-channel gain-phase analyzer configured in the software radio. The resonance frequencies of the gyroscope are matched within 20mHz using the bottom electrode. The mode mismatch varies up to 80mHz after a few days of testing. Figure 6.10 shows the decay time plots of the two wineglass modes, measured after tuning both modes. The τ_o values of the two modes after mode matching are measured to be 8.67 and 7.57 seconds. It is believed that the reduction in τ_o after tuning occurs due to cross coupling between the two modes.
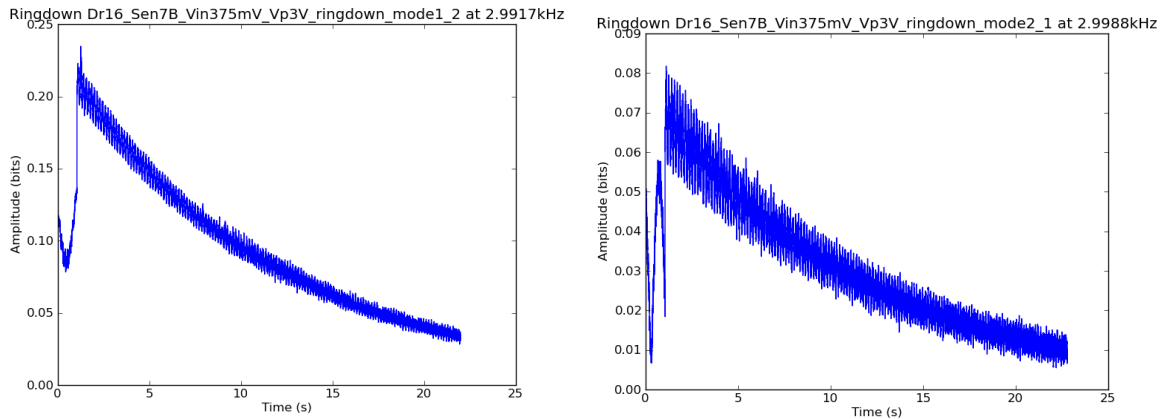
(a) Mode 1 (at 2991.7Hz)   (b) Mode 2 (at 2998.8Hz)

Figure 6.8. Decay time plots of the two wineglass modes of the CING at untuned state. The measured decay time constants (τ_o) of the two modes are 10 and 11.5 seconds.
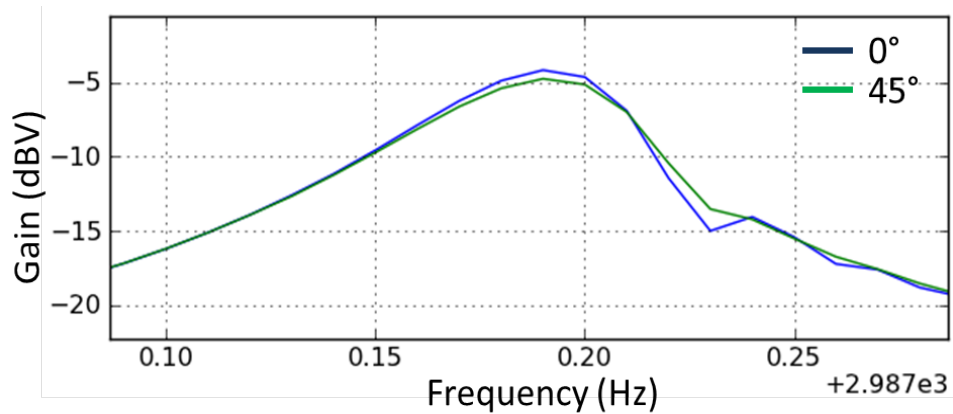
Figure 6.9. FFT plots of the two wineglass mode peaks after tuning them within 20mHz.
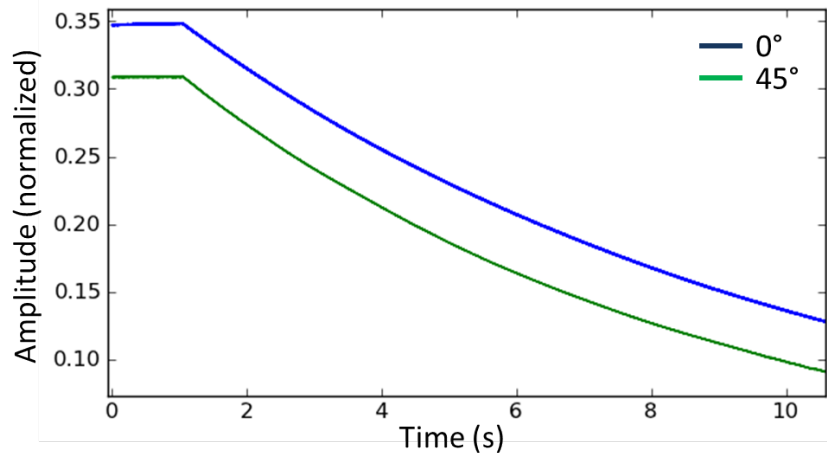
Figure 6.10. Decay time constants of the two wineglass modes after mode matching (<20mHz). The τ_o are 8.67 and 7.57 seconds.

6.4. Device Evaluation

The CING is tested both in the rate and rate-integrating modes using two different interface circuits. The CING is mounted on the PCB board containing the frontend circuitry and placed in an Ideal Aerospace Aero900 rotation table.

6.4.1. Architecture of Interface Circuitry for Rate- and Rate-Integrating Operations

The interface circuitry for rate-sensing mode control is identical to the circuit in Chapter 5. The interface circuitry for rate-integration mode is implemented using a combination of firmware and software in USRP1 system (Figure 6.11) [122]. In the FPGA, readout signals are demodulated with reference signals, and the data is sent to the computer where in-phase energy (E), quadrature energy (Q), and oscillation position (θ) are calculated. The system can also position the wave pattern at a programmed position.

191
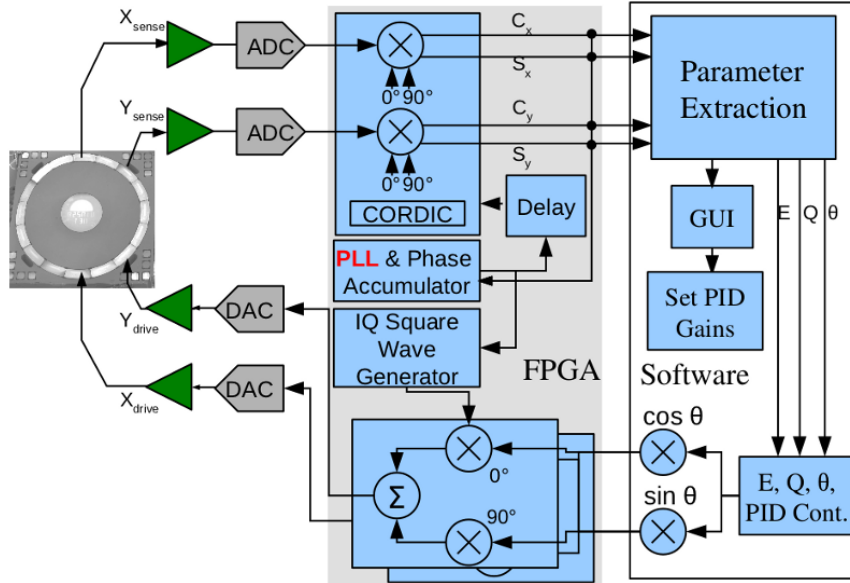
Figure 6.11. Architecture of digital circuit for rate-integrating-mode operation [122].

6.4.2. Angular Gain (A_g) Measurement

Tue angular gain (A_g) of the gyro is measured using from the slope of the input rotation (Ω) and the ratio of driving and force-feedback amplitudes ($\theta_{control}/E_{control}$), which is the same method discussed in Chapter 5. Figure 6.12 shows input rate and ($\theta_{control}/E_{control}$) of the low-frequency CING with matched τ of 8 seconds. From the slope of this graph and the τ, the A_g is calculated as 0.0065.
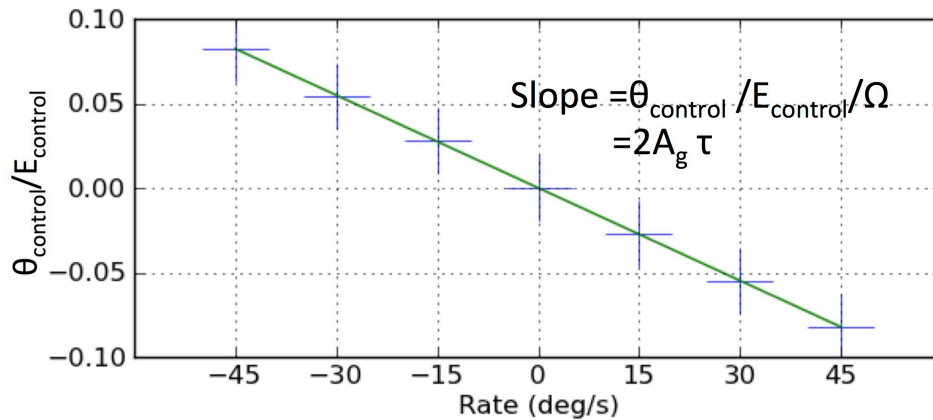
Figure 6.12. Ratio of sense feedback and driving amplitudes ($\theta_{control}/E_{control}$) versus in rotation rate (Ω).

6.4.3. Rate-Sensing Mode Operation

The root Allan variance plot of CING is shown in Figure 6.13. The measured angle random walk (ARW) is 0.09°/√Hr, and the bias stability is 129°/Hr. It is believed that there is a low-frequency noise source at 0.1Hz, which limits the stability. The stability of the sensor is also expected to improve with temperature control. The relationship between the ratio of the position-control signal amplitude and amplitude-control signal amplitude ($\theta_{control}/E_{control}$) under input rotation rate (Ω) of -45 deg/sec to 45 deg/sec is shown in Figure 6.14. This measurement is done using rate-integrating mode control circuitry by holding the wave position at an arbitrary position (θ). The rate-mode scale factor of gyro can be found from the slope of this graph [-0.0018(V/V)/(°/sec)]. A stable scale factor is calculated by holding the wave pattern at different positions. However, due to the difference in the mechanical anisotropy, bias in the measured signals is found to vary with θ. Figure 6.15 shows the change in the $\theta_{control}/E_{control}$ measured for rotation
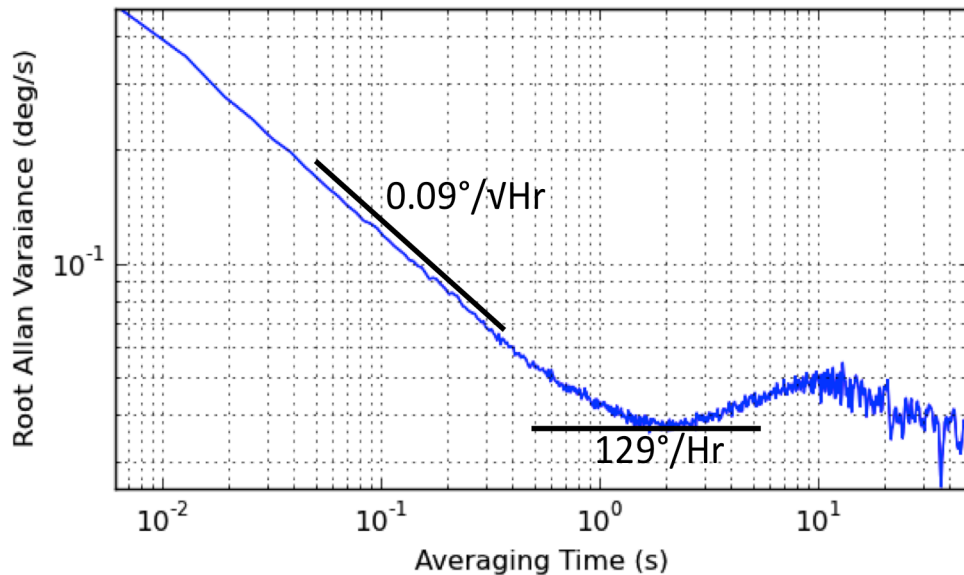
Figure 6.13. Root Allan variance plot of the low-frequency CING, indicating angle random walk (ARW) of 0.09°/√Hr and bias stability of 129°/Hr.

rates from -45 deg/sec to 45 deg/sec with a step of 15deg/sec for 40 minutes without compensating the device temperature. The drift rate of the sensor is found as 1°/sec/Hr.
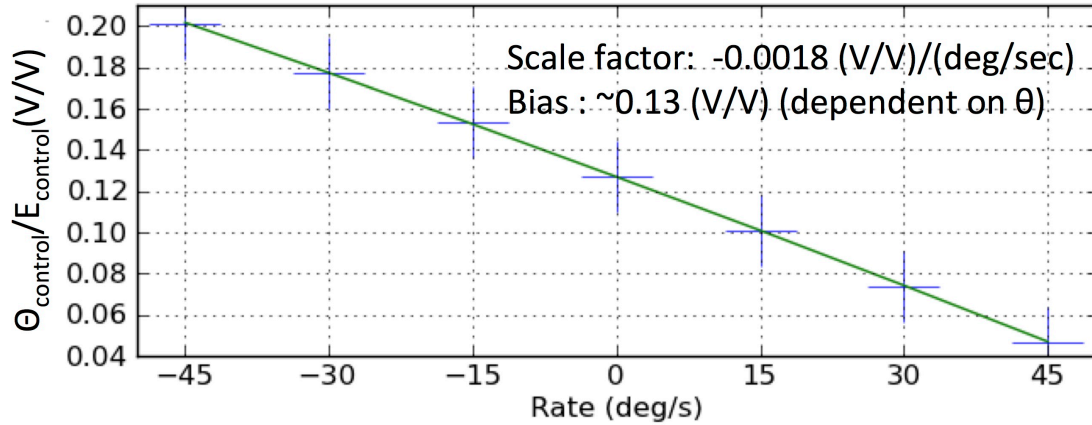
Figure 6.14. Ratio of position-control signal to amplitude-control signal ($\theta_{control}/E_{control}$) under rotation rate ($\Omega$) of -45 to 45deg/sec, measured in force feedback mode using rate-integrating-mode control circuitry.
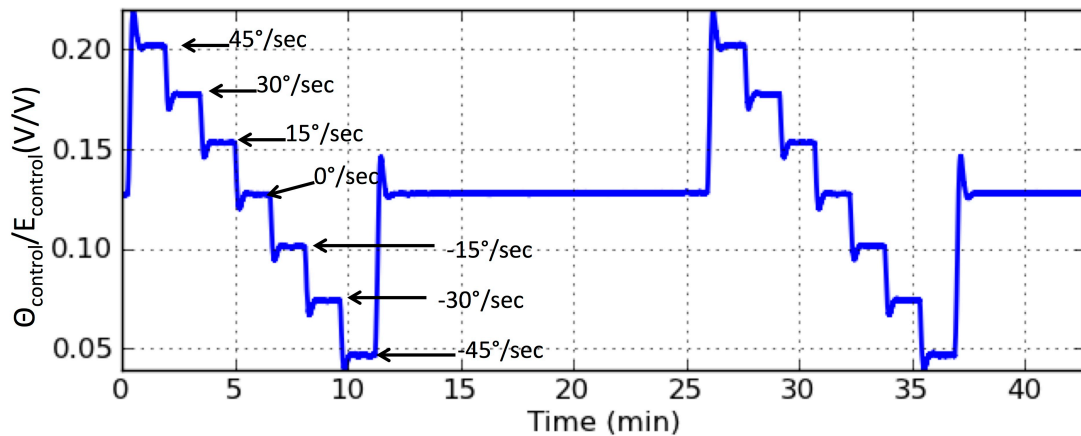
Figure 6.15. Ratio of position-control signal to amplitude-control signal ($\theta_{control}/E_{control}$) under rotation rate ($\Omega$) of -45°/s to 45°/s with step of 15°/s for 40 minutes of operation.

6.4.1. Rate-Integration Mode (Whole-Angle-Mode) Operation

The CING is tested under rotation rates of 60º/sec and 30º/sec in rate-integrating mode. Figure 6.16 shows the plots of precessional pattern positions (θ). The blue curve and green curve indicate the change in the θ under rotational rates of 60°/sec and 30°/sec, respectively. The gyroscope coordinate rotates by 180° in 276 seconds at 60°/sec and in

535 seconds at 30°/sec. An ideal gyro will have a linear change in θ with respect to time, but due to the mechanical anisotropy, the precessional patterns deviate from linear curve.

The angular gain (A_g) is defined as the ratio between the precessed angle of the vibrational pattern measured in the Cartesian coordinate to an applied rotation angle. The A_g is calculated as:

$$A_g = \frac{180(\text{deg})}{60(\text{deg}/s) \times 276 \text{sec}} = 0.0108 \qquad \text{(Equation 6.2)}$$

The measured A_g from the precessional pattern is slightly different from the A_g measured in the rate-sensing mode (0.006) in Section 6.4.2. The same A_g is calculated from the precessional data under a rotation rate of 30°/sec. The A_g is found to be stable at
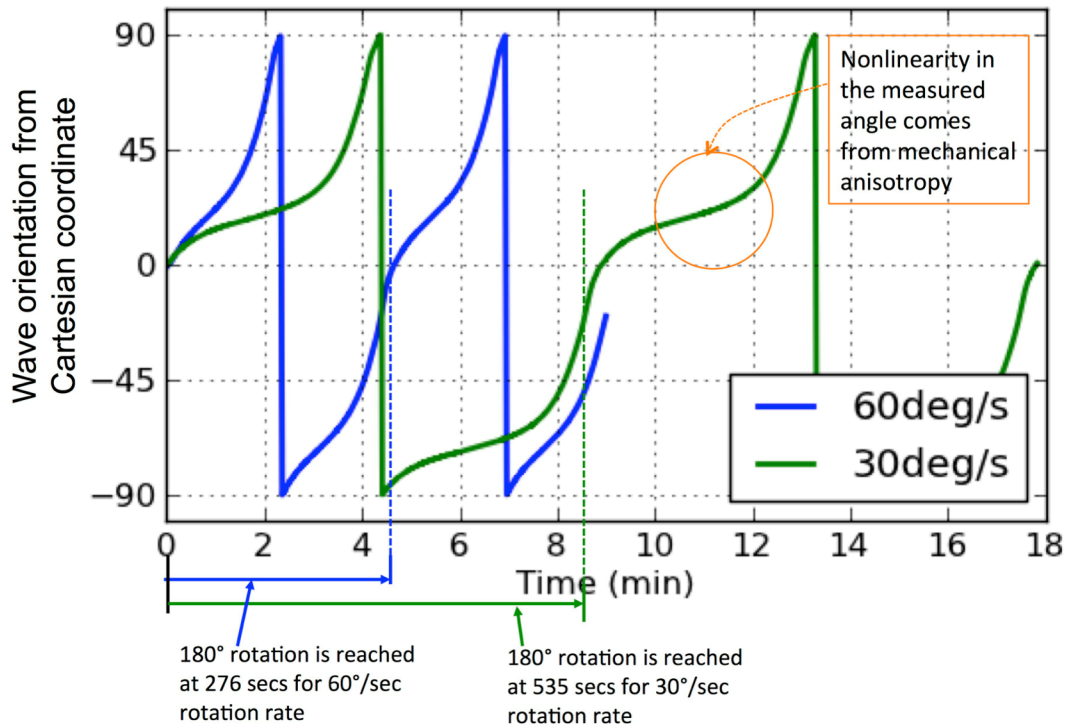
Figure 6.16. Change in wave orientation following rotation rate of 60°/sec and 30°/sec. The wave pattern under 60°/sec reaches to 180° in 276 seconds. The wave pattern under 30°/sec reaches to 180° in 535 seconds. The data indicates a constant angular gain (A_g) of 0.0108 for both cases, proving the concept of the whole-angle mode gyroscope. The A_g is found to be 0.011±0.001 under 20~80mHz mode mismatch.

0.011±0.001 over a wide frequency range of 20~80mHz for several days, proving the concept of the whole-angle-mode gyroscope.

Figure 6.17 shows the change in the quadrature control amplitude for a wave position (θ) of -90° to 90°. The value of the quadrature-compensating signal shown in this graph is normalized with respect to its mean value. The quadrature error compensation output is proportional to the pattern of mass, stiffness and damping anisotropy, and the periodicity in the quadrature compensation signal indicates the periodicity in the mechanical anisotropy profile along the perimeter of the gyro. The amplitude of the quadrature control signals under rotation signals of 0 deg/sec, 30 deg/sec, and 60 deg/sec match, indicating that the physical sources causing the quadrature error do not vary with rotation speed. These anisotropy data can be calibrated and used to compensate the inaccuracy of the gyro in the future.

Figure 6.17.   Wave orientation with respect to the principal motion axes of the wineglass mode, under 0 deg/sec, 30 deg/sec, and 60 deg/sec rotation rates.

6.5. Summary and Discussion

The second-generation CING is designed to provide a longer nominal damping time τ_o to reduce the angular drift due to damping anisotropy. The dimension of the CING measures outer (R) and anchor radii (AR) of 6mm and 1.5mm, respectively, ring thickness (T) of 20μm, height (H) of >300μm, and a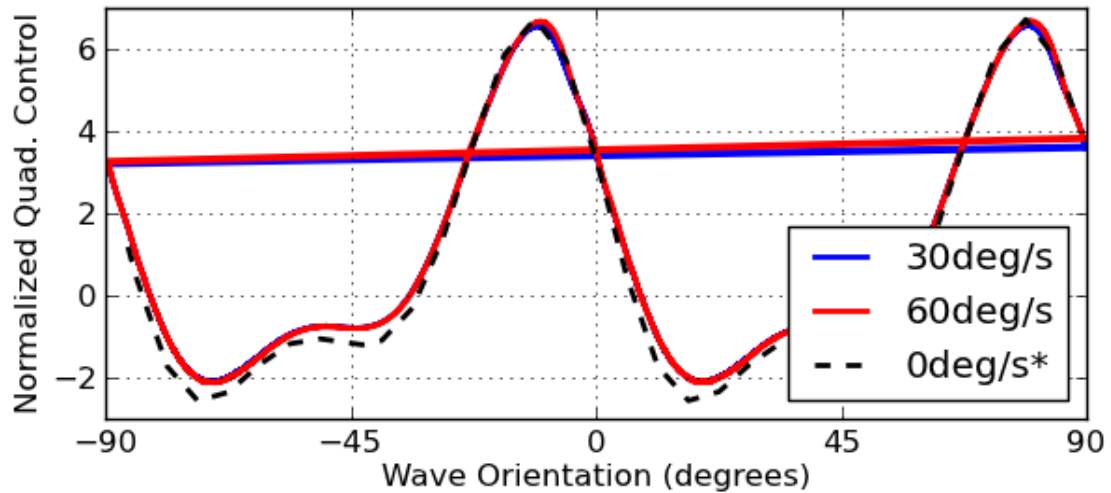 bottom plate thickness (BT) of ~20μm. The $n=2$ wineglass mode is found at 3kHz, and its lowest parasitic mode is found at >5kHz from ANSYS simulation. This modal characteristic is believed to provide superior vibration rejection. A drawback of the second-generation CING geometry is low angular gain (A_g) due to low aspect ratio (~0.01).

The CING is fabricated using the same Si-on-glass (SOG) process that is used to fabricate the first-generation CING. The depth of glass recess is increased to 5μm to account bowing due to TCE mismatch between glass and Si. Due to its large device size, the gyro has nearly 10pF capacitance from the bottom electrode and 2.6pF capacitance from the side electrode. The simulated Q_{TED} value from ANSYS matches very closely with the measured Q value (~100,000). A nominal frequency mismatch of less than 10Hz is found, and the frequencies are electronically tuned to 20mHz mismatch.

The CING is tested with digital interface circuitry. The sensor measures an angle random walk (ARW) of 0.09°/√Hr and a bias stability is 129°/Hr. The resolution of the gyro is limited by the A_g (~0.01) and electrical noise.

In the whole-angle-mode operation, the second-generation CING measures an A_g of 0.011±0.001 at a frequency gap of 20~80mHz for several days of operation. The design and test summary of the second-generation CING is provided in Table 6.2.

The A_g of the CING is small because of large vertical motion in the wineglass mode, which does not contribute to the generation of the Coriolis force. The A_g can be improved by increasing the device height, but due to the limitation in the etch depth in the SOG process, it is challenging to increase the device.

To achieve improved whole-angle-mode performance, it is necessary to find a new axisymmetric gyro geometry with low f_{WG} (<5kHz), large separation between $f_{parasitic}$ and f_{WG} (>2kHz), large A_g (~0.3), small device size (<1cm).

Table 6.2. Design and test summary of second-generation CING

Design / Fabrication Results	Value	Sensor Parameters	Value
Anchor / outer radii (*AR*/*R*)	1.5mm / 6mm	f_{WG} (Δf (original))	3kHz (7Hz)
Height (*H*)	320µm	τ_o ($\Delta 1/\tau$)	10~12 sec (0.01Hz)
Anchor width (*AT*) / ring width (*T*)	100µm / 20µm	A_g	0.0065 (rate-mode), 0.011 (whole-angle mode)
Bottom plate thickness (*BT*)	~20µm	Bias stability (rate mode)	129°/Hr
Drive / sense capacitance	2.6pF/10pF	Angle random walk (ARW) (rate mode)	0.09/√Hr
		Offset drift (rate mode)	1°/s/Hr

CHAPTER 7.

VIBRATION SENSITIVITY OF BALANCED-MODE GYROSCOPES

In the previous few chapters, we have discussed the design of balanced-mode gyroscopes. The balanced-mode gyroscope has two advantages with respect to vibration sensitivity: ideally zero coupling from vibration to the sense mode, and differential cancellation of in-phase modes. However, due to structural imbalance, the design does not entirely remove vibration sensitivity. In this chapter, the effect of acceleration on the mechanical system will be explained using lumped-mass models. The influence of acceleration on the Balanced Oscillating Gyroscope (BOG) and the Cylindrical Rate-Integrating Gyroscope (CING) with mechanical anisotropy will then be analyzed using FEM.

7.1. Vibration Sensitivity of Single Mass Gyroscope

The simplest form of gyroscope is the single mass gyroscope (Figure 7.1). In this gyroscope, a mass is surrounded by directional springs along two orthogonal axes. The dynamics of the single mass gyroscope is simple and obvious. The behavior of this type of gyro under environmental acceleration can be also easily explained. The vibrational gyro dynamics of this simple gyroscope, however, share a lot of common physical principles with complex multiple-degree-of-order systems.
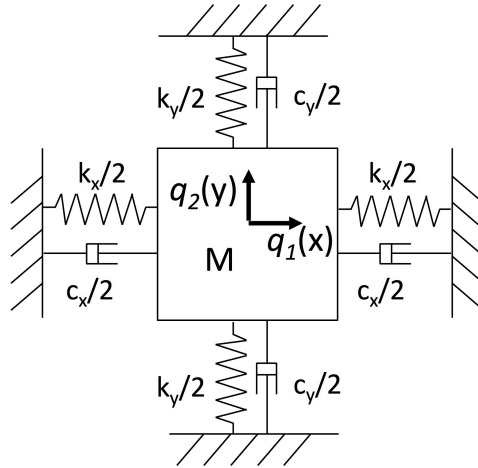
Figure 7.1. Single mass gyroscope.

The gyroscope's dynamics along the two axes can be explained using two sets of motional equations defined from its potential energy, inertia, and damping energy (Equations 7.1-7.2). The system also includes the Coriolis force, control force, and force generated from external vibrations.

Inertia		Damping		Coriolis force		Stiffness		Control force	Vibraiton
$M\ddot{q}_1$	$+$	$c_1\dot{q}_1$		$-\,2MA_g\dot{q}_2\Omega_z$	$+$	k_1q_1	$=$	$f_1(t)$	$+\quad Ma_1$

$$\text{(Equation 7.1)}$$

Inertia		Damping		Coriolis force		Stiffness		Control force	Vibraiton
$M\ddot{q}_2$	$+$	$c_2\dot{q}_2$		$-\,2MA_g\dot{q}_2\Omega_z$	$+$	k_2q_2	$=$	$f_2(t)$	$+\quad Ma_2$

$$\text{(Equation 7.2)}$$

Ideally, there is no force except the Coriolis force that can excite the sense mode motion. In rate gyroscopes, the magnitude of the Coriolis force along the driving axis is usually small, because there is only very small motion in the sense axis and the amplitude control loop can easily cancel the small Coriolis force. In the rate-integrating gyroscope (RIG), only the total oscillation energy is controlled and Coriolis force from either axis can be large.

Depending on the nature of vibration, the vibration force can be either a periodic or random signal. When a periodic force is acting along driving direction, the control circuit

essentially cancels the effect of both in-phase and quadrature forces. When the vibration force has the same phase as the existing driving force, the two forces will add constructively, and the control circuitry will adjust the drive amplitude in order to maintain the right oscillation amplitude. When the vibration force is a quadrature signal with respect to the existing oscillation, the addition of the two signals produces a motion that has a slight angle mismatch with respect to the driving signal. Then naturally the self-oscillation circuit adjusts the input force phase to maintain 0-degree phase shift over the drive loop, which brings the drive oscillation in phase with the noise signal. Therefore, regardless of the phase between the existing oscillation and the applied vibration, the self-oscillation loop absorbs the noise signal. Practically, there is very small amount of noise energy that can match the driving mode frequency, due to narrow bandwidth and high quality factor (Q).

On the other hand, when the vibration along the sense direction has the same phase with the Coriolis force, the signal is indistinguishable from a rate signal. When the vibration pattern has a quadrature relationship with the Coriolis force, the motion can be canceled by a quadrature control loop or rejected by phase sensitive processing of the rate signal. In the rate-integrating gyroscope (RIG), the quadrature environmental forces along both axes can be nulled by a quadrature control loop. An environmental force that is in phase with the Coriolis force can induce drift.

For these reasons and because a random motional force along the drive axis is generally much smaller than the driving force, random vibrational motion along the sense axis dominates the vibration-induced rate noise signal.

One can define the vibrational sensitivity of a gyroscope ($S_{vibration}$) as a rotational rate that generates same amount of Coriolis force to the force generated by random acceleration of amplitude a. The acceleration force is simply Ma, and the apparent Coriolis force is $2kMq_{drive}\omega\Omega$, where k angular gain factor, q_{drive} is the drive axis amplitude, ω is the operating frequency, and Ω is rotation rate. The k of a tuning fork gyro is 1, and the k of an $n=2$ wineglass mode gyro is $2A_g$, where A_g denotes angular gain. Assuming matched mode, $S_{vibration}(\omega)$ for a single mass gyro can be calculated as:

$$S_{vibration}(\omega)[\Omega/(g/\sqrt{Hz})] = \frac{Ma}{2kMq_{drive}\omega}$$
$$= \frac{a}{2kq_{drive}\omega} \qquad \text{(Equation 7.3)}$$

The $S_{vibration}$ is directly proportional to a and inversely proportional to k, q_{drive}, and ω.

7.2. Vibration Sensitivity of Balanced Gyroscope

In the balanced mode, the net momentum of the motional system is zero because of the complementary phase of the masses constituting the resonator. In a balanced mode gyroscope, there are two balanced modes, one for the driving mode and the other for the sensing mode. In the case of the BOG, the driving mode consists of four degrees of freedom. There are four independent but coupled driving masses, making four different modes. In the sense direction, there are two modes, where the two semi-open frames oscillate either in-phase or out-of-phase (Figure 7.2). The characteristic coordinates of displacement for each mass in a dynamic system is called the generalized coordinate. For the BOG, the generalized coordinate q_1, q_2, q_3, and q_4 are for the driving mode along x-axis coordinates. The coordinates q_5 and q_6 are for the sense mode and represent torsional angles along the x-axis.
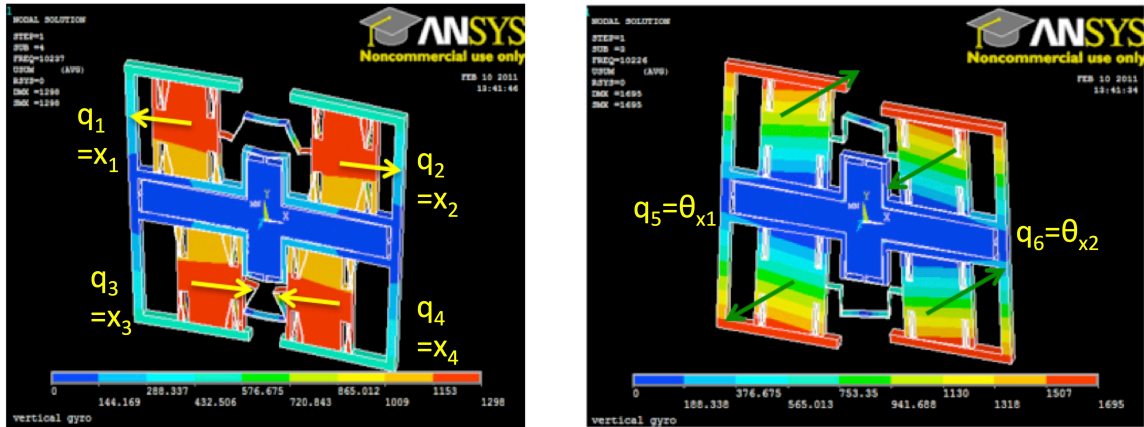
(a) Drive mode: generalized coordinates are x-axis coordinates of the individual driving masses (q_1-q_4)

(b) Sense mode: generalized coordinates are x-axis torsional angles (q_5, q_6)

Figure 7.2. Driving and sensing mode patterns of the Balanced Oscillating Gyroscope (BOG).

As we discussed in the previous section, for the rate gyroscope (RG), the vibrational noise signal is dominated by the motion along the sense axis. Therefore, vibrational sensitivity can be studied by considering the sense mode motion. In the rate-integrating gyroscope (RIG), vibration along both axes contributes equally to the sense mode, but one can consider the device behavior along a single axis to predict the vibrational sensitivity.

In this study, we first consider a simple 2-DOF balanced mechanical system (Figure 7.3). The two masses are connected in the middle with a coupling spring, and the masses are connected to the anchor via two separate springs. This mechanical system has two resonance modes. In the first mode (the in-phase mode), the two masses oscillate in the same direction, with the same amplitude. The stiffness of the in-phase mode is determined by only the springs that connect the mass to the anchor, and so its frequency must be lower than the balanced mode. The second mode is the balanced mode, where the two masses oscillate with opposite phase and exactly the same amplitude. The

stiffness of this mode is determined by the coupling spring as well as the anchor springs, so the frequency is higher than the in-phase mode.

The in-phase mode can be excited with environmental acceleration, so in a noisy environment, there is a large motion at this frequency due to resonance of the masses. However, the effect of this motion on the rate signal is relatively small due to two reasons. First, the in-phase motion is differentially cancelled in the interface circuitry. When the amplitude is large, residual noise can remain due to nonlinearity and mismatch in the capacitive measurement mechanism. The second reason is that the in-phase mode can be located outside the bandwidth of the sensor by controlling the coupling stiffness. In this case, the interface circuit can filter out the in-phase mode frequency component.

The balanced mode cannot be excited by external vibration. This is because the forces generated in the two identical masses under external vibration always have the same phase and the same magnitude and so the direction of these forces does not cause out-of-phase motion. This will be proven in a later section. The vibration sensitivity of the balanced mode is therefore zero.

The power spectral density of the motional amplitude of a perfectly balanced gyroscope under external vibration is described in Figure 7.6. This model assumes perfectly matched modes and a zero rotation rate. The diagram also includes the sense mode gain curve and the filter gain curves. The largest motional amplitudes are found at the driving mode frequency (ω_{drive}), the parasitic sensing mode frequency ($\omega_{parasitic\text{-}sensing}$), and additionally the parasitic driving frequency ($\omega_{parasitic\text{-}driving}$). The parasitic driving motion is in-phase motion along the driving axis. Under rotation, it creates Coriolis force which excites the in-phase sense axis mode, which can be differentially canceled by the

interface circuitry. When these modes are located outside the sensor bandwidth, the

perfectly balanced gyroscope effectively has zero vibration sensitivity.
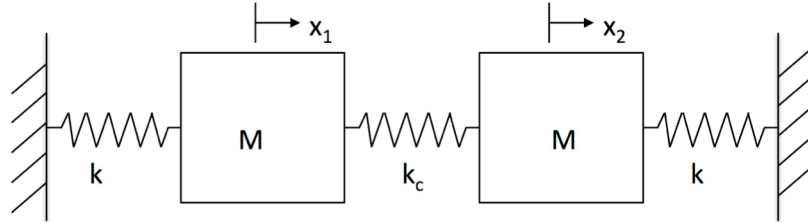
Figure 7.3. Two degree-of-freedom balanced system. The mass (M) and stiffness (k) are identical. Generalized coordinates are q_1 and q_2.
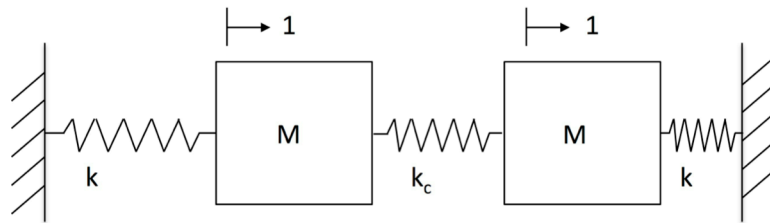
Figure 7.4. Displacement of masses at the parasitic resonance mode
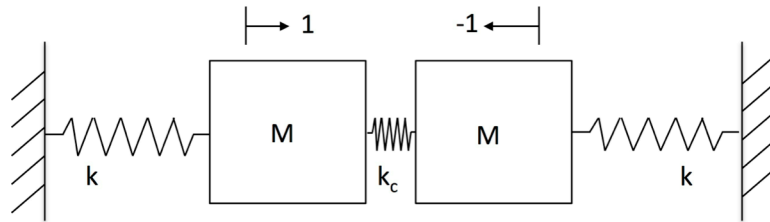
Figure 7.5. Displacement of masses at the balanced mode.
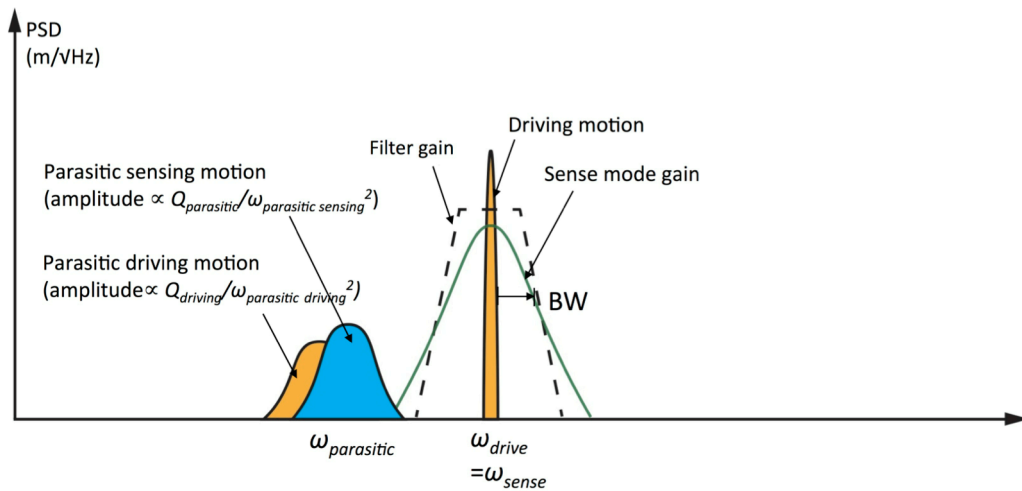
Figure 7.6. Power spectral density of perfectly balanced gyroscope (matched mode case). The parasitic mode frequency $\omega_{parasitic}$ is located outside the bandwidth of the sensor, so the effect of the parasitic motion is negligible.

7.3. Vibration Sensitivity of Non-Ideally Balanced Gyroscope

7.3.1. Effect of Mass and Stiffness Imbalance on the 2-DOF Spring-Mass System

In the real case, a coupled mechanical system cannot have perfectly matched stiffness and mass. When there is a difference between the masses or the springs in the coupled mechanical system, the eigenvector ratios at both resonance modes deviate from the perfect case of $q_1/q_2 = 1$ (in-phase frequency) and $q_1/q_2 = -1$ (balanced frequency) (Figure 7.7).

Under external acceleration, the imperfectly balanced mode becomes excitable with external vibration. Therefore, the power spectral density of the imperfectly balanced system under vibration has motional amplitude at the sense mode frequency (ω_{sense}), even when there is no rotation (Figure 7.8). This sense-mode motion has the same shape as any sense-mode motion excited by the Coriolis force, so the vibrational error signal cannot be distinguished from a real rotation signal.

7.3.2. Derivation of the Out-of-Phase Motion of an Imperfectly Balanced System

Stiffness and mass mismatch affect the system independently, and the motional equations accounting for each of these effects can be separately derived. The motion of the 2-DOF unbalanced system (Figure 7.7 (a)) under stiffness imbalance can be derived with the following procedure. The displacement ratio of the two masses for a high-Q system does not change significantly with damping, so we will neglect the damping effect in this calculation. The kinetic energy (T) and potential energy (V) due to the springs for each single mass are described in terms of its generalized coordinate. For the mass on the left, T becomes:

$$T_1 = \frac{1}{2} M \dot{q}_1^2 \qquad \text{(Equation 7.4)}$$

The *V* associated with this mass is the spring energies for the spring (*k+Δk/2*) connected

to the anchor and the coupling spring (*k_c*). The potential energy accumulated is a

function of the difference in the displacement between *q₁* and *q₂*.

$$V_1 = \frac{1}{2}(k + \Delta k/2)q_1^2 + \frac{1}{2}k_c(q_1 - q_2)^2 \qquad \text{(Equation 7.5)}$$

The kinetic and potential energies (*T₂*, *V₂*) of the mass on the right are calculated in the

(a) Stiffness anisotropy

(b) Mass anisotropy
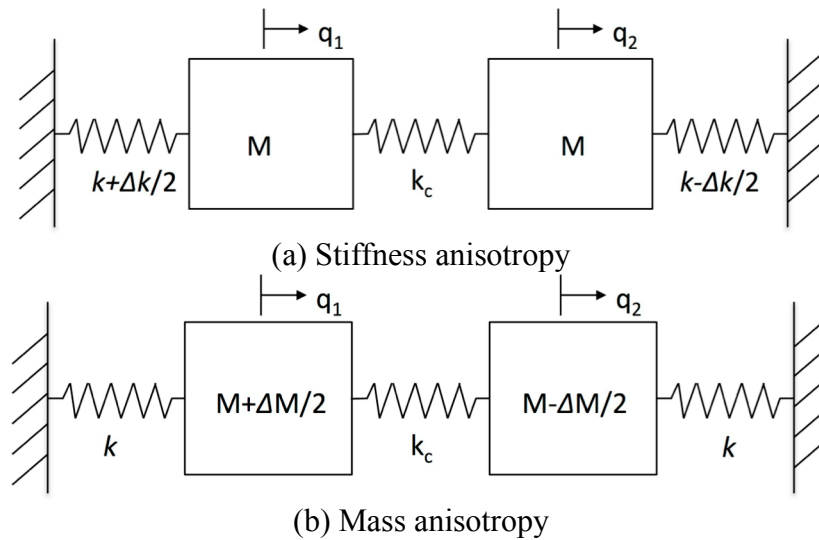
Figure 7.7. Imperfectly balanced system with stiffness and mass mismatch
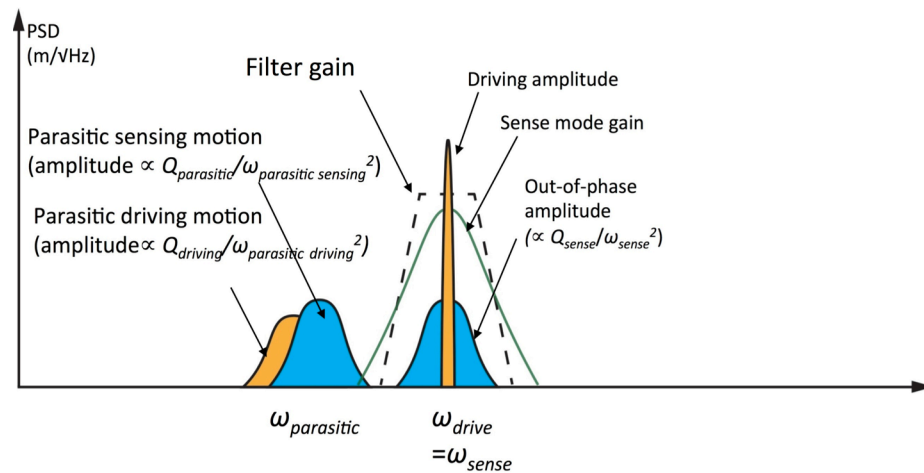
Figure 7.8. Power spectral density of imperfectly balanced gyroscope (matched mode case). External vibration excites sense mode. The sense-mode motions excited by external vibration and Coriolis force cannot be distinguished.

similar way, yielding:

$$T_2 = \frac{1}{2}M\dot{q}_2^2$$

$$V_2 = \frac{1}{2}(k - \Delta k/2)q_2^2 + \frac{1}{2}k_c(q_1 - q_2)^2$$

Under external acceleration a, the generated forces are:

$$F_1 = F_2 = Ma$$

Then the motional equation for this system can be summarized as Equation 7.9.

$$\begin{bmatrix} M & 0 \\ 0 & M \end{bmatrix} \begin{bmatrix} \ddot{q}_1 \\ \ddot{q}_2 \end{bmatrix} + \begin{bmatrix} k + \Delta k/2 + k_c & -k_c \\ -k_c & k - \Delta k/2 + k_c \end{bmatrix} \begin{bmatrix} q_1 \\ q_2 \end{bmatrix} = \begin{bmatrix} F_1 \\ F_2 \end{bmatrix}$$

If F_1 and F_2 are harmonic forces, the displacements of the system q_1 and q_2 are also periodic. By assuming q_1 to be $Q_1 exp(j\omega t)$ and q_2 to be $Q_2 exp(j\omega t)$, the eigenvalue of this system is found from equating the left-hand-side matrix to zero.

$$\det\left(\begin{bmatrix} -M\omega^2 + \left(k + \Delta k/2 + k_c\right) & -k_c \\ -k_c & -M\omega^2 + \left(k - \Delta k/2 + k_c\right) \end{bmatrix}\right) = 0$$

The solutions of this equation are:

$$\omega_1 = \pm\sqrt{\frac{2(k + k_c) - \sqrt{\Delta k^2 + 4k}}{2M}}$$

(in-phase mode)

$$\omega_2 = \pm\sqrt{\frac{2(k + k_c) - \sqrt{\Delta k^2 + 4k}}{2M}}$$

(out-of-phase mode)

The eigenvectors for the two modes are found by entering ω_1 and ω_2 in the motional equations. When the eigenvectors of the masses are normalized in terms of displacement

of the left-hand-side mass, the normalized amplitudes for the left and right masses in the

in-phase and out-of-phase modes ϕ_{ij} (i: mass number, j: mode number) become:

$$(\phi_{11}, \phi_{21}) = \left(1, \frac{\Delta k + \sqrt{\Delta k^2 + 4k_c^2}}{2k_c}\right) \quad \text{(In-phase mode)} \qquad \text{(Equation 7.13)}$$

$$(\phi_{12}, \phi_{22}) = \left(1, \frac{\Delta k - \sqrt{\Delta k^2 + 4k_c^2}}{2k_c}\right) \quad \text{(Out-of-phase mode)} \qquad \text{(Equation 7.14)}$$

At the in-phase mode, the mass connected to the spring with smaller stiffness

oscillates with larger amplitude than the mass connected to spring with larger stiffness.

At the out-of-phase mode, the mass connected to a spring with the smaller stiffness

oscillates with smaller amplitude than the mass connected to the spring with the larger

stiffness. The absolute value of the eigenvector ratios ϕ_{21}/ϕ_{11} and ϕ_{12}/ϕ_{22} deviate further

from 1 with increasing $|\Delta k/k_c|$.

The original motional equation (Equation 7.9) is derived accounting for the motion

of each mass. However, the motion of each mass is a superposition of the two modal

patterns, and the motional equation can be expressed in terms of each mode. The method

to treat the overall displacement as a sum of the displacements of the modes is called the

modal superposition method [123]. The modal superposition method is very useful in

understanding how much effective mass, stiffness, and force exists at each of the modes.

The modal motional equation can be simply derived from the previous motional

equation by accounting for the modal eigenvector ratio. The displacements (q_1 and q_2)

are a sum of normalized eigenvectors ϕ_{ij} (i: mass number, j: mode number), multiplied by

the modal amplitude, named the eigencoordinate (z_j).

$$q_1 = \phi_{11}z_1 + \phi_{12}z_2 \qquad \text{(Equation 7.15)}$$

$$q_2 = \phi_{21}z_1 + \phi_{22}z_2 \qquad \text{(Equation 7.16)}$$

The expressions for q_1 and q_2 (Equations 7.15 and 7.16) are then inserted in the original motional equation (Equation 7.9).

$$M(\phi_{11}\ddot{z}_1 + \phi_{12}\ddot{z}_2) + (k + \Delta k/2 + k_c)(\phi_{11}z_1 + \phi_{12}z_2) - k_c(\phi_{21}z_1 + \phi_{22}z_2) = F_1 \qquad \text{(Equation 7.17)}$$

$$M(\phi_{21}\ddot{z}_1 + \phi_{22}\ddot{z}_2) + (k - \Delta k/2 + k_c)(\phi_{21}z_1 + \phi_{22}z_2) - k_c(\phi_{11}z_1 + \phi_{12}z_2) = F_2 \qquad \text{(Equation 7.18)}$$

The Equations 7.17 and 7.18 are then scaled by (ϕ_{11}, ϕ_{21}) and (ϕ_{12}, ϕ_{22}), respectively, to form two pairs of equations.

- First pair:

$$M(\phi_{11}^2\ddot{z}_1 + \phi_{11}\phi_{12}\ddot{z}_2) + (k + \Delta k/2 + k_c)(\phi_{11}^2 z_1 + \phi_{11}\phi_{12}z_2) - k_c(\phi_{11}\phi_{21}z_1 + \phi_{11}\phi_{22}z_2) = \phi_{11}F_1$$
$$\text{(Equation 7.19)}$$

$$M(\phi_{21}^2\ddot{z}_1 + \phi_{21}\phi_{22}\ddot{z}_2) + (k - \Delta k/2 + k_c)(\phi_{21}^2 z_1 + \phi_{21}\phi_{22}z_2) - k_c(\phi_{21}\phi_{11}z_1 + \phi_{21}\phi_{12}z_2) = \phi_{21}F_2$$
$$\text{(Equation 7.20)}$$

- Second pair:

$$M(\phi_{11}\phi_{12}\ddot{z}_1 + \phi_{12}^2\ddot{z}_2) + (k + \Delta k/2 + k_c)(\phi_{11}\phi_{12}z_1 + \phi_{12}^2 z_2) - k_c(\phi_{12}\phi_{21}z_1 + \phi_{12}\phi_{22}z_2) = \phi_{12}F_1$$
$$\text{(Equation 7.21)}$$

$$M(\phi_{21}\phi_{22}\ddot{z}_1 + \phi_{22}^2\ddot{z}_2) + (k - \Delta k/2 + k_c)(\phi_{21}\phi_{22}z_1 + \phi_{22}^2 z_2) - k_c(\phi_{11}\phi_{22}z_1 + \phi_{12}\phi_{22}z_2) = \phi_{22}F_2$$
$$\text{(Equation 7.22)}$$

The two pairs of equations are now summed. In the summation, some of the resulting eigenvectors can be summed to zero, using principles of modal mass and stiffness orthogonality [146]. In the modal equations, the products of the eigenvectors for different modes acting on the same discrete mass or spring constants are zero. The equations are expressed using the mass (M), stiffness matrix (K), and the eigenvector as:

$$\phi_{ij}^T M \phi_{ik} = 0 \text{ (when } j \neq k)$$ (Equation 7.23)

$$\phi_{ij}^T K \phi_{ik} = 0 \text{ (when } j \neq k)$$ (Equation 7.24)

$$M = \begin{bmatrix} M & 0 \\ 0 & M \end{bmatrix}$$ (Equation 7.25)

$$K = \begin{bmatrix} k + \Delta k/2 + k_c & -k_c \\ -k_c & k - \Delta k/2 + k_c \end{bmatrix}$$ (Equation 7.26)

The scaled sum of two pairs of equations (Equations 7.19-7.20 and 7.21-7.22) then become expressions in terms of the eigencoordinates z_1 and z_2.

For in-phase mode:

Effective Mass   Effective Stiffness   Effective Force

$$M(\phi_{11}^2 + \phi_{21}^2)\ddot{z}_1 + \left((k + \Delta k/2 + k_c)\phi_{11}^2 + (k - \Delta k/2 + k_c)\phi_{21}^2 - 2k_c\phi_{11}\phi_{21} \right)z_1 = \phi_{11}F_1 + \phi_{21}F_2$$

(Equation 7.27)

For out-of-phase mode:

Effective Mass   Effective Stiffness   Effective Force

$$M(\phi_{12}^2 + \phi_{22}^2)\ddot{z}_2 + \left((k + \Delta k/2 + k_c)\phi_{12}^2 + (k - \Delta k/2 + k_c)\phi_{22}^2 - 2k_c\phi_{12}\phi_{22} \right)z_2 = \phi_{12}F_1 + \phi_{22}F_2$$

(Equation 7.28)

The motional equations in terms of the eigencoordinates contain very useful information about individual modes. First, these equations show how the unbalance terms are related to the effective mass change and the effective stiffness change. Due to stiffness imbalance, one can see that both of these parameters change. Second, the equations show that the effective forces exciting the in-phase and out-of-phase forces are simply the sums of arbitrarily applied forces, multiplied by the normalized eigenvectors.

211

The equations prove that the amount of effective force for a perfectly balanced system ($\phi_{12}/\phi_{22} = -1$) at the balanced mode is indeed zero.

For an imbalanced gyroscope, vibrational sensitivity at the out-of-phase sense mode $S_{vibration}$ (rad/sec/(g/$\sqrt{Hz}$)) can be defined as the equivalent rotational rate for generating the Coriolis force equal to the effective vibrational force. In Figure 7.7-(a), when we assume that an identical amount of out-of-phase Coriolis force ($2kM_{drive}q_{drive}\omega_o$) is acting the effective force for the out-of-phase mode becomes,

$$F_{effective} = (\phi_{12} - \phi_{22})(2M_{drive}kq_{drive}\omega_o\Omega) \text{ (From Coriolis force)} \qquad \text{(Equation 7.29)}$$

The effective force for the balanced mode due to in-phase acceleration a becomes:

$$F_{effective} = (\phi_{12} + \phi_{22})(Ma) \text{ (From in-phase acceleration } a) \qquad \text{(Equation 7.30)}$$

The equivalent rotation rate at the sense mode can derived by equating Equations 7.29-7.30.

$$S_{vibration}(\omega_o)[\Omega / (g / \sqrt{Hz})] = \left| \frac{Ma(\phi_{12} + \phi_{22})}{2M_{drive}kq\omega_o(\phi_{12} - \phi_{22})} \right| \qquad \text{(Equation 7.31)}$$

From Equation 7.31 we see there is a term that contains the imbalance of the structure which we define as the structural imbalance factor (Z).

$$Z \equiv \frac{(\phi_{12} + \phi_{22})}{(\phi_{12} - \phi_{22})} \qquad \text{(Equation 7.32)}$$

Z can be evaluated in two different ways. First, Z can be calculated by finding ϕ_{ij} from modal analysis. For a complex geometry, ϕ_{ij} can be calculated using modal analysis methods in FEM tools. The second method is the division of differential amplitudes ($|q_1-q_2|$) found experimentally from the application of the same force either in phase or in opposite phase to the two masses. At the sense mode frequency, the structure only

responds to the effective force components that excite the sense resonance pattern, and the displacement is multiplied by the Q factor. It can be shown that, the $|q_1-q_2|$ at ω_{sense} due to both the in-phase and opposite-phase forces are Q times the deflection amplitude at zero frequency, and the division of the in-phase and opposite-phase excited displacements yields the same expression as Equation 7.33.

$$\left(q_1-q_2\right)(\omega_{out-of-phase})\Big|_{in-phase\ force} \approx Q_{out-of-phase}\frac{\left(\phi_{12}+\phi_{22}\right)}{k_{out-of-phase}}F(\omega=0)$$

(under out-of-phase force F)   (Equation 7.33)

$$\left(q_1-q_2\right)(\omega_{out-of-phase})\Big|_{out-of-phase\ force} \approx Q_{out-of-phase}\frac{\left(\phi_{12}-\phi_{22}\right)}{k_{out-of-phase}}F(\omega=0)$$

(under in-phase force F)   (Equation 7.34)

$$\frac{\left(q_1-q_2\right)\Big|_{in-phase\ force}}{\left(q_1-q_2\right)\Big|_{out-of-phase}}(\omega_{out-of-phase}) \approx Z$$

(Equation 7.35)

The $S_{vibration}$ under mass imbalance (Figure 7.7-(b)) can be derived in a similar way. In the mass imbalance case, the eigenvector ratio between the two masses increases with $|\Delta M/M|$, as it does for $|\Delta k/k_c|$ for stiffness anisotropy.

The differential displacement $|q_1-q_2|$ of masses of the 2-DOF coupled system with different stiffness imbalance ratios are calculated for the in-phase and opposite-phase forcing schemes (Figure 7.9). The ratio between the $|q_1-q_2|$ for in-phase (blue) and out-of-phase (green) actuation schemes becomes the imbalance parameter (Z) of the system. The amplitude curves are calculated for $\Delta k/k$ of 0.1~0.3. The modeled mechanical system has a k/M of 1 and k_c/k of 0.1. A damping coefficient (c) of $0.001M$ is used in parallel with each spring. Since we are only interested in comparing the ratio between the displacements under the two forcing schemes, the nominal value of c does not have a

significant meaning in this calculation, in the figure, $|q_1\text{-}q_2|$ under in-phase forcing (green)

has a smaller value than $|q_1\text{-}q_2|$ under opposite-phase force (blue) at the in-phase mode

and vice versa for the out-of-phase mode. The gap between the in-phase and out-of-

Figure 7.9. Relationship between absolute value of the difference in the displacement of the two masses $|q_1\text{-}q_2|$ under in-phase (blue) and out-of-phase force (green) and ratio of stiffness anisotropy ($\Delta k/k$). In the numerical calculation, the physical parameters of the mechanical system is set to k/M of 1, k_c/k of 0.1, and $c/M =0.001$.
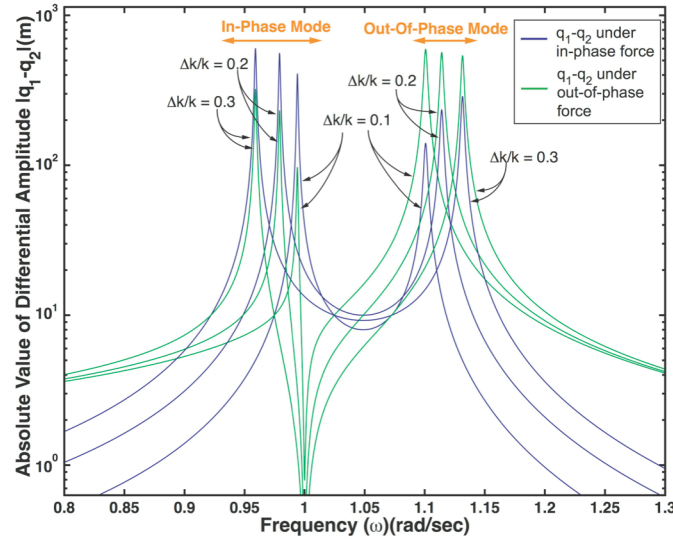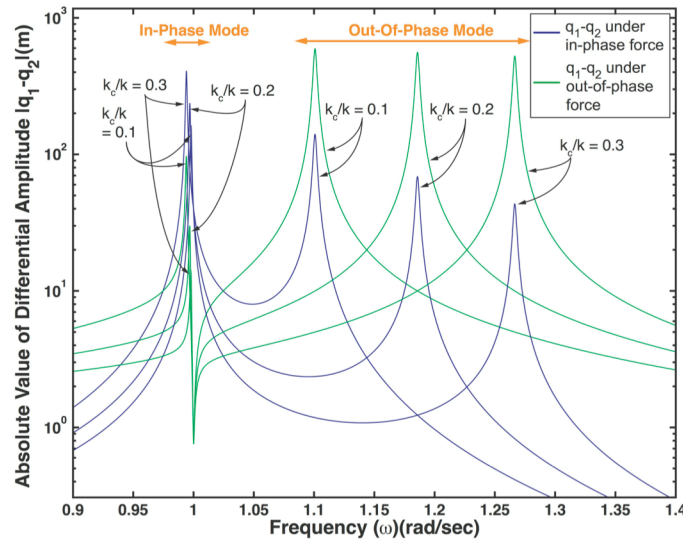

Figure 7.10. Relationship between absolute value of the difference in the displacement of the two masses $|q_1\text{-}q_2|$ under in-phase (blue) and out-of-phase force (green) and ratio between coupling stiffness and nominal stiffness k_c/k. In the numerical calculation, the physical parameters of the mechanical system is set to k/M of 1, $\Delta k/k$ of 0.1, and $c/M = 0.001$.

phase modes increase with the increasing $\Delta k/k$. The difference between $|q_1-q_2|$ under in-phase and opposite-phase decreases with increasing $\Delta k/k$, indicating that the vibrational sensitivity of the non-perfectly balanced gyroscope increases with the increase in stiffness mismatch. Figure 7.10 shows the relation between $|q_1-q_2|$ and the harmonic forcing frequency ω for k_c/k from 0.1~0.4 for constant stiffness imbalance $\Delta k/k$ of 0.2. The difference between $|q_1-q_2|$ from opposite-phase actuation (green) and in-phase actuation (blue) increases with k_c/k.

Under a constant $\Delta k/k$ ratio, the trend of the differential amplitude ratios can be quantitatively understood by considering the limit cases of k_c/k approaching infinity and zero. When k_c/k is infinite, the two coupled masses act as a merged mass, with a total mass of $2M$ (Figure 7.11). In the in-phase mode, the effective stiffness is contributed solely by the springs connected to the anchor ($2k$), so the resonance mode is found at $\sqrt{k/M}$ rad/sec. In this mode, the merged masses translate along the same direction with the same amplitude. On the other hand, the opposite-phase mode is determined by k_c and the mode frequency approaches infinity. Since k_c is much larger than k, the effect of imbalance in k is negligible and the mechanical system can be considered to be two masses connected to only a single spring. Then the two masses oscillate in the opposite phase with the exactly same amplitude, and the system resembles the perfectly balanced system.

On the other hand, when k_c/k is zero, the motion of the two masses becomes completely uncoupled (Figure 7.12). Since there is no mechanical coupling, the two masses oscillate at their own resonance frequencies ($\sqrt{(k+\Delta k/2)/M}$, $\sqrt{(k-\Delta k/2)/M}$). In this case, each mode is just the resonance frequency of one mass and in each mode

only a single mass oscillates. The displacement difference $|q_1-q_2|$ is just $|q_1|$ or $|q_2|$ under the two forcing schemes and the ratio effectively becomes $|q_1/q_2|$, which is close to 1.

The relation between the $\Delta M/M$ and $|q_1-q_2|$ ratios under two edge cases can be investigated in a similar way. Figure 7.13 shows $|q_1-q_2|$ from both in-phase (blue) and out-of-phase actuation (green) for $\Delta M/M$ of 0.1~0.3. In the calculation model, k/M is set

(a) In-phase mode ($q_1/q_2 = 1$)

(b) Out-of-phase mode ($q_1/q_2 = -1$)

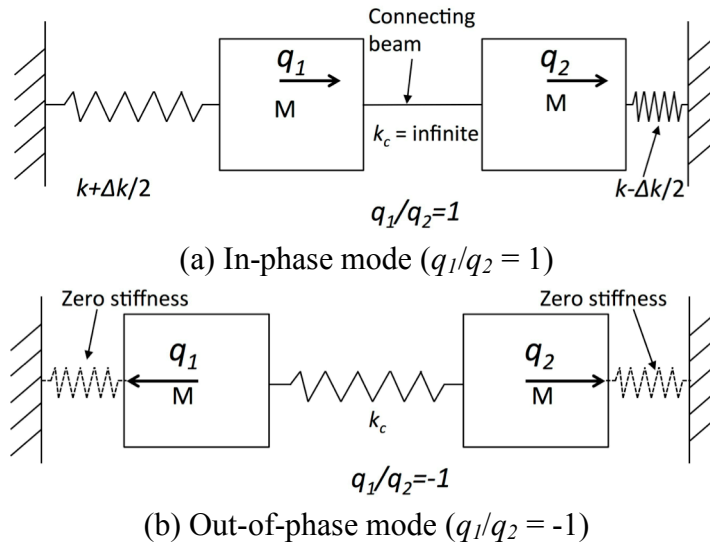Figure 7.11. Conceptual diagram describing in-phase and out-of-phase modes of 2-DOF coupled spring-mass system with k_c/k approaching infinity.

(a) Mode 1 ($\omega_1 = \sqrt{(k - \Delta k/2)/M}$)

(b) Mode 2 ($\omega_2 = \sqrt{(k + \Delta k/2)/M}$)
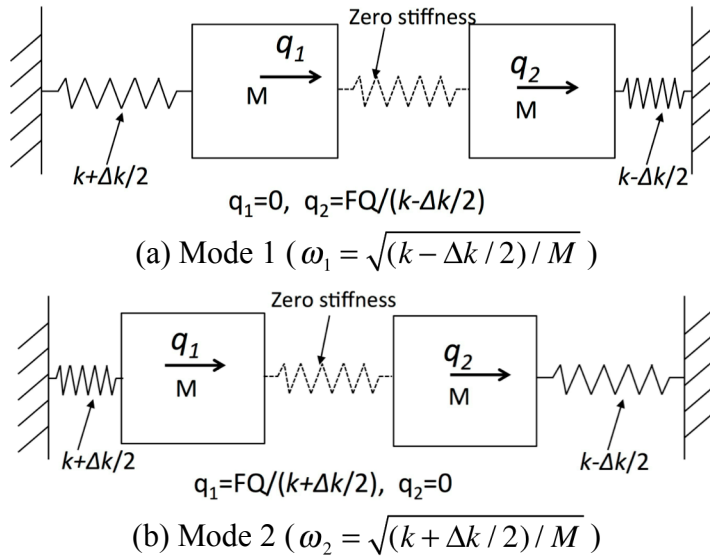
Figure 7.12. Conceptual diagram describing in-phase and out-of-phase modes of 2-DOF coupled spring-mass system with k_c/k approaching zero.

to 1 and k_c/k is set to be $0.3k$. Figure 7.14 plots $|q_1$-$q_2|$ from in-phase and out-of-phase actuation schemes for k_c/k in (0.1, 0.4), with $\Delta M/M$ equal to 0.1. Similarly to the case with stiffness variation, the difference between $|q_1$-$q_2|$ from out-of-phase actuation increases with k_c/k.

7.4. FEM Analysis of the Imbalance Factor of the Balanced Oscillating Gyro (BOG)

The principle of the Balanced Oscillating Gyroscope (BOG) was described in chapter 3. In its drive mode, four coupled masses oscillate in-plane with opposite phase. In the sense mode, the two semi-open frames oscillate torsionally along the axis of the sense torsional beam in opposite phase, whereas in the parasitic sense mode, the two frames oscillates with the same phase. The BOG has the largest vibrational sensitivity to acceleration that excites the parasitic sense mode, which is the angular acceleration
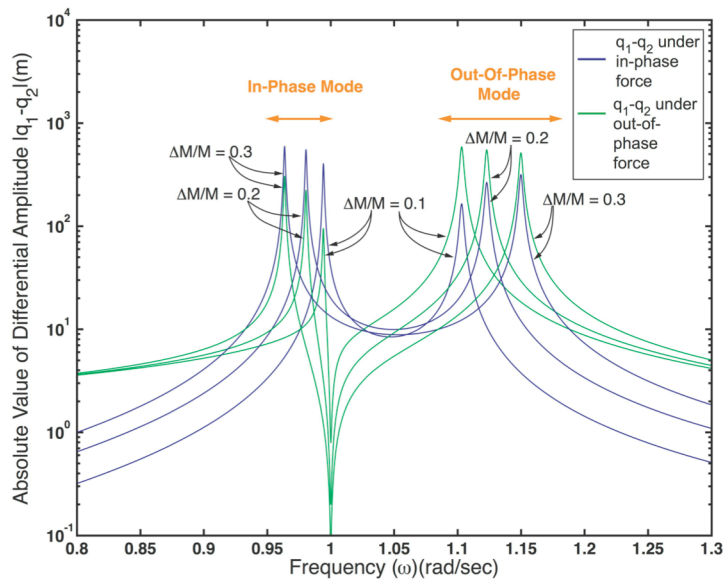
Figure 7.13.   Relationship between the absolute value of the difference in the displacement of the two masses $|q_1$-$q_2|$ under in-phase (blue) and out-of-phase forces (green) and ratio of stiffness anisotropy ($\Delta M/M$).   In the numerical calculation, the physical parameters of the mechanical system is set to k/M of 1, k_c/k of 0.1, and c/M of 0.001.
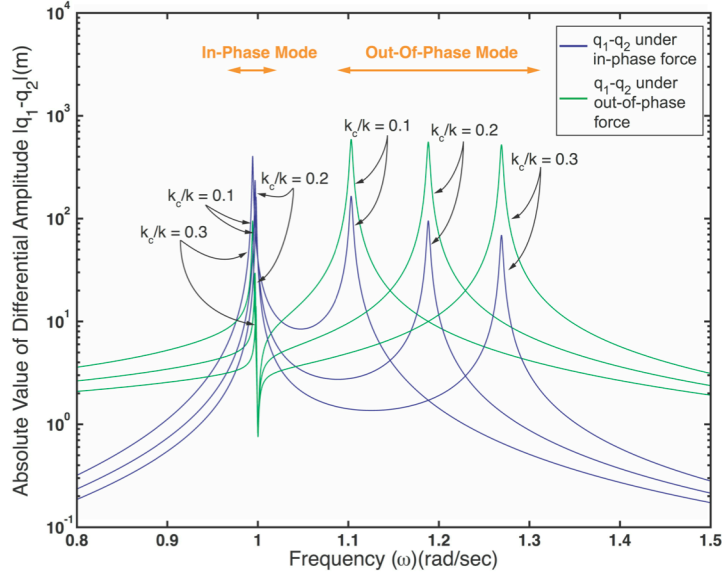
Figure 7.14. Relationship between absolute value of the difference in the displacement of the two masses $|q_1-q_2|$ under in-phase (blue) and out-of-phase forces (green) and ratio between coupling stiffness and nominal stiffness k_c/k. In the numerical calculation, the physical parameters of the mechanical system is set to k/M of 1, $\Delta M/M$ of 0.1, and c/M of 0.001.

around the sense torsional beam.

Imbalance in the BOG is created from variation in the mask dimensions in the DRIE process. The geometrical variation due to the micromachining process is, at most, a few microns. Since this variation is small compared to the proof mass dimensions, mass imbalance from geometrical variation is negligible. The stiffness, however, can change significantly due to the geometrical variation. The stiffness of the sense torsional beam ($k_{x\theta}$) is proportional to the polar moment of inertia of the rectangular beam (J_x), and it is a function of width (w) and height (h) of a torsional beam [100].

$$J_x = \frac{wh}{12}(w^2 + h^2) \qquad \text{(Equation 7.36)}$$

In the current Si-on-glass (SOG) process, the height of the device is 100μm, and the width of the torsional beam is ~20μm. Therefore, the variation in the polar moment of

218

inertia ($\Delta J_x/J_x$) is a function of $\Delta w/w$ and as a result, $k_{x\theta}$ is a function of $\Delta w/w$. A Δw of just 1μm in the torsional beam creates a 5% variation in in the torsional stiffness.

Due to the complexity in the coupling mechanism, the Z of the sensor is studied using ANSYS. In the software, the eigenvector ratios of the two frames under stiffness imbalance are calculated in modal analysis mode. Eigencoordinates for the in-phase and out-of-phase angular accelerations are then calculated using the modal superposition method in harmonic analysis mode.

The relation between $f_{parasitic}/f_{sense}$ and the ratio between the deflection of the semi-open frames on the left-hand side and right-hand side is simulated, under 10% width mismatch between the torsional beams (torsion beam at the left side of the gyro is made 10% thicker than the torsion beam at the right hand side), with a nominal width of 10μm. Note that this simulation model has a smaller beam width than the original BOG, but it is expected that Z will change with the same tendency as the change in modal characteristics. The $f_{parasitic}/f_{sense}$ ratio is changed with the width of the lateral torsional beam (along x-axis) of the sense coupling spring (Figure 7.15). The relationship between the $f_{parasitic}/f_{sense}$ and the normalized eigenvector ratios ($\left| \phi_{\theta 1} / \sqrt{\phi_{\theta 1}^2 + \phi_{\theta 2}^2} \right|$, $\left| \phi_{\theta 2} / \sqrt{\phi_{\theta 1}^2 + \phi_{\theta 2}^2} \right|$) of the torsional motion of the two frames are plotted in Figure 7.16. When $f_{parasitic}/f_{sense}$ is smaller than 1, the absolute value of the eigenvector for the left frame is larger than right frame. At $f_{parasitic}/f_{sense}$ of 1, the imbalance in the eigenvector is maximized. As $f_{parasitic}/f_{sense}$ passes 1, the normalized eigenvector of the right-hand-side frame becomes larger than the left-hand side frame. There is a clear instability point when $f_{parasitic}/f_{sense}$ is 1. Due to the instability, the imbalance parameter for $f_{parasitic}/f_{sense}$ of 0.98~1.02 is difficult to simulate.
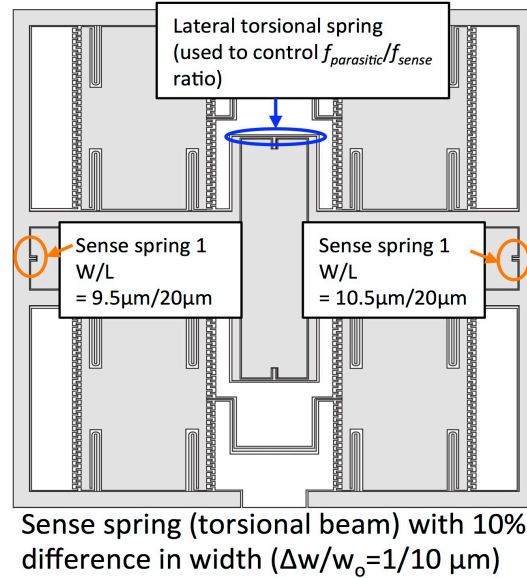
Figure 7.15. Geometry of the BOG with a structure imbalance of 10% in the in torsional stiffness of the sense spring.
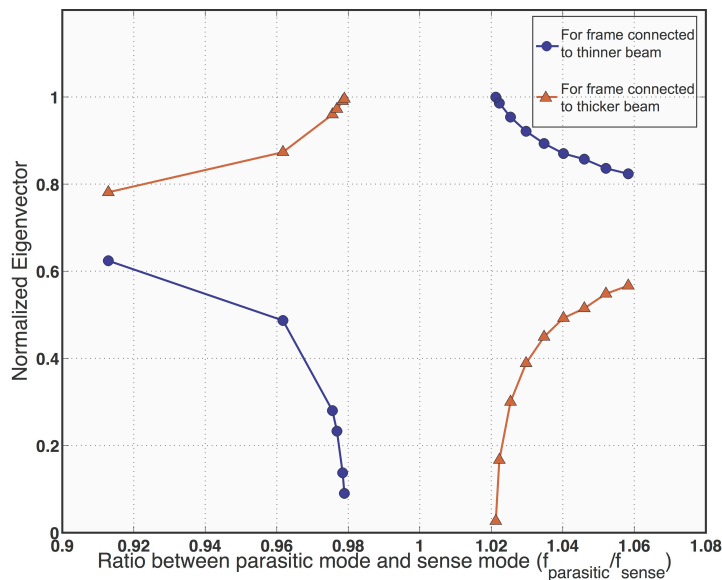
Figure 7.16. Relationship between the ratio of the parasitic sense mode and the sense mode ($f_{parasitic}/f_{sense}$) and the absolute value of the normalized eigenvectors of the semi-open frames of the BOG, under 10% difference between the two sense springs (torsional beam). The normalized eigenvectors of the frames connected to a beam with smaller and larger widths are plotted in blue and orange, respectively.

The same BOG model with stiffness imbalance is subjected to in-phase and out-of-phase forces which excite both the sensing and parasitic sensing modes. Angular acceleration is approximated with linear (z-axis) forces acting at the ends of both frames

with a magnitude F_z of 1N, creating x-axis torque of 1500N·μm to a single torsional frame (Figure 7.17). The eigencoordinate ratios of the two modes under these forces are plotted in Figure 7.18. The ratio between eigencoordinates due to the in-phase harmonic force and the out-of-phase harmonic force maximizes when $f_{parasitic}/f_{sense}$ approaches 1. This is because the eigenvector ratio for the in-phase and out-of-phase modes is largest at this frequency region.

From this analysis, it is partially verified that, like the simple 2-DOF spring-mass case, coupling stiffness in the balanced mode motion strongly influences Z and, as a result, the vibrational sensitivity at the sense frequency ($S_{vibration}(\omega_{sense})$). It is also found that the $S_{vibration}(\omega_{sense})$ decreases with the increase in $|f_{parasitic\_sense} - f_{sense}|/f_{sense}$. The polarity of the frequency difference does not affect the vibration sensitivity. Therefore, by placing $f_{parasitic\_sense}$ as far as possible from f_{sense}, a gyro can have a low $S_{vibration}(\omega_{sense})$. One disadvantage associated with having $f_{parasitic\_sense}$ lower than f_{sense} is that the sensor will have worse shock resistance because the sensor will have a larger deflection under shock.
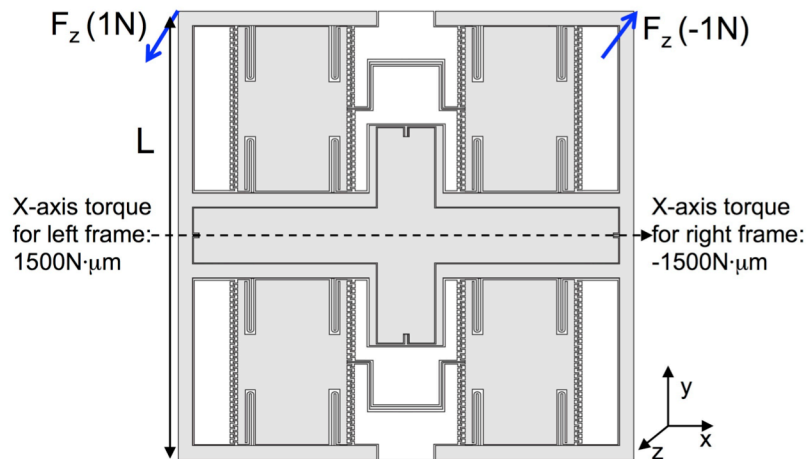
Figure 7.17. Application of z-axis force (1N) at the ends of torsional frames to create x-axis harmonic torque (T_x: 1500N·μm).
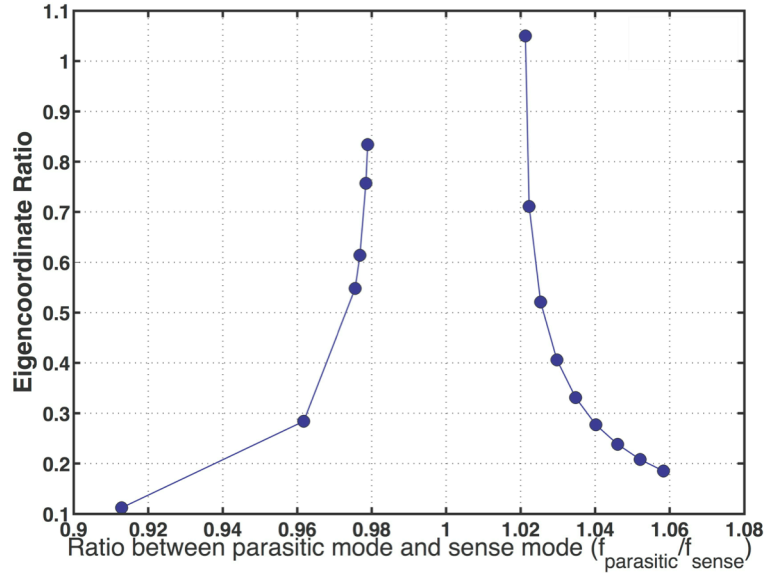
Figure 7.18. Relationship of the ratio between the parasitic sense mode and the sense mode frequencies ($f_{parasitic}/f_{sense}$) and eigencoordinate ratios in the sense mode. Gyro has 10% difference two sense springs (torsional beams). In-phase and out-of-phase x-axis harmonic torque of 1500μm·N is applied to each of the torsional frames.

7.5. FEM Analysis of the Imbalance Factor of the Cylindrical Rate-Integrating Gyro (CING)

Flexural mode gyroscopes include shell (hemispherical, half-toroid, cylinder, and ring) and disk gyroscopes. Similar to the tuning fork gyros, flexural mode gyroscopes with structural imbalance have the largest vibration sensitivity at the parasitic and flexural mode frequencies.

Compared to tuning-fork gyroscopes, the shell gyroscopes have smaller nominal mass. Therefore, mass anisotropy in the resonator has larger relative influence on the vibrational sensitivity of these gyros. Another key difference of flexural mode gyroscopes is that their vibrational sensitivity at flexural frequencies is a function of the periodicity of mass and stiffness variation along the perimeter [124]. This is because the flexural mode itself has a periodic deformation pattern along the perimeter, and the force generated due to stiffness and mass imbalance has to match the flexural mode shape in

order to excite the flexural mode. Flexural mode gyroscopes generally have tilting and vertical modes located near the wineglass mode, and under external acceleration these parasitic modes have the largest coupling to the wineglass mode (Figure 7.19).

When a vertical linear force is applied to a gyro with $sin(2\varphi)$ distribution of mass or stiffness anisotropy (Figure 7.20), where φ is the azimuthal angle, the out-of-phase vertical force also has the same $sin(2\varphi)$ distribution (Figure 7.21). As seen in Figure 7.19, the wineglass mode has vertical motion as it is flexed, so under $sin(2\varphi)$ out-of-phase vertical force, the flexural mode can be excited. When the mass has higher even-number harmonics ($cos(4\varphi), cos(6\varphi),$ etc) the vertical force patterns do not fit the profile of vertical motion in the wineglass mode, so the n=2 wineglass mode cannot be excited.

When the stiffness and mass imbalance has a distribution of $sin((2n+1)\varphi)$ (Figure

(a) Wineglass Mode

(b) Tilting Mode
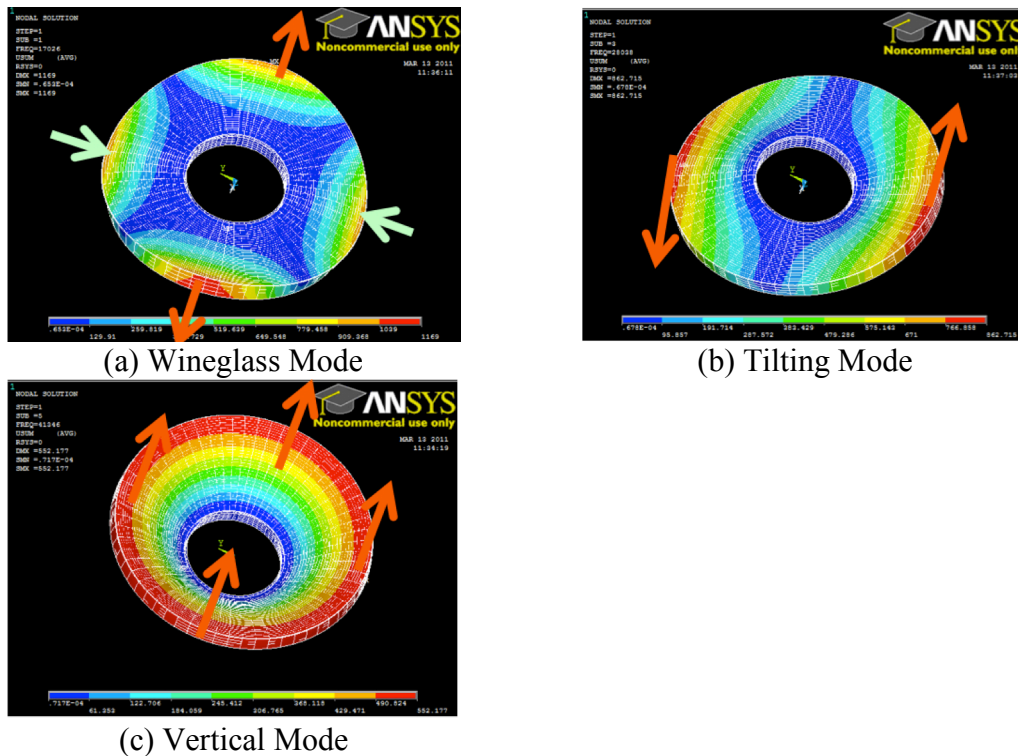
(c) Vertical Mode

Figure 7.19. Displacement patterns of wineglass mode, tilting mode, and vertical mode of the Cylindrical Rate-Integrating Gyroscope (CING), simulated using ANSYS.
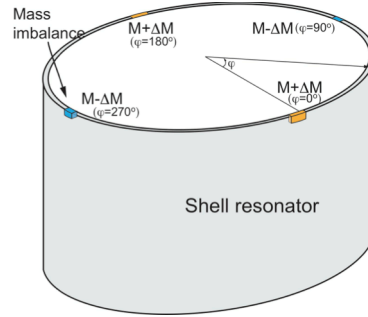
Figure 7.20. Mass imbalance pattern of $\Delta M = \Delta M_o cos(2\varphi)$, where φ is azimuthal angle along the perimeter of the shell
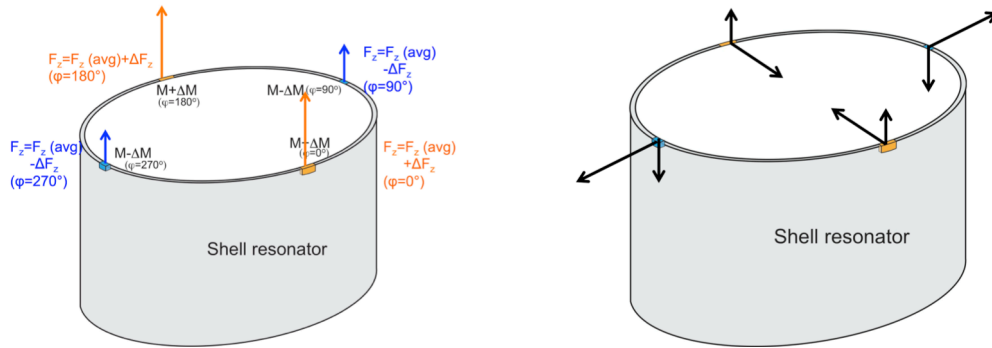
(a) Force difference generated from z-axis linear acceleration

(b) Pattern of induced wineglass mode

Figure 7.21. Imbalance in z-axis force generated to resonator having a mass imbalance pattern of $\Delta M = \Delta M_o cos(2\varphi)$ (φ: azimuthal angle) and the resultant displacement pattern of the $n=2$ wineglass mode

7.22) the $n=2$ wineglass mode can be excited by planar angular acceleration (Figure 7.23). The planar angular acceleration causes in-plane forces to the resonator. When the gyro has such $sin((2n+1)\varphi)$ mass or stiffness distribution, the distribution is anti-symmetric with respect to a cross section through the center of the gyro. So out-of-phase force can be generated from the in-phase force. The largest out-of-phase force, which excites the flexural mode, is generated when the direction of the linear acceleration is aligned to the antinode.

The relation between the ratio of the tilting mode and the wineglass mode frequency ($f_{tilting}/f_{WG}$) to the imbalance parameter of the CING is simulated with FEM. In this simulation, an approximate $sin(\varphi)$ mass-imbalance pattern is created in the model by

varying the density of the structure from the normal value at the top one fifth of the cylinder sidewalls between φ of -6°~6° and 174°~186° by -10% and 10% (Figure 7.24). Then the mass function over the perimeter of the gyro has a negative antinode at $\varphi = 180°$ and positive antinode at $\varphi = 0°$. The nominal ratio between the mass variation and the nominal mass of the devices ($\Delta M_{nominal}/M_{nominal}$) is 0.1%. The simulation is done using a high-frequency CING, with an outer radius (R) of 2500µm, bottom plate thickness (BT) of 50µm, and ring thickness (T) of 30µm. Devices with two different heights (H), 300µm and 3000µm, are simulated. The tilting mode frequency ($f_{tilting}$) is varied by changing the anchor radius (AR) of the cylinder. By changing the AR, a 30~40% change in $f_{tilting}$ is achieved while f_{WG} stayed nearly constant, having a variation of less than 2.5%.

Figure 7.25 shows the relationship between the $f_{tilting}/f_{WG}$ and normalized displacements at the top edge of the CING model at $\varphi = 0°$ and 180°. The normalized displacements increase as $f_{tilting}/f_{WG}$ approaches 1. Figure 7.26 shows the relationship between $f_{tilting}/f_{WG}$ and the structural imbalance factor Z, calculated by applying harmonic torques normal to cross-sectional plane that connects $\varphi = 0°$ to 180°. The Z value is maximized with $f_{tilting}/f_{WG}$ equal to 1, which implies the vibrational sensitivity at the
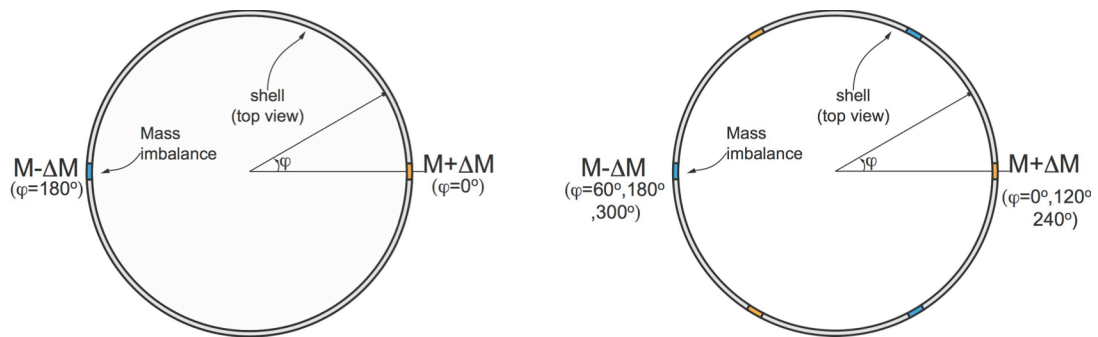
(a) Mass distribution of $\Delta M = \Delta M_o cos(\varphi)$ (b) Mass distribution of $\Delta M = \Delta M_o cos(3\varphi)$

Figure 7.22. Top view of mass distribution profile of $\Delta M = \Delta M_o cos(\varphi)$ and $\Delta M = \Delta M_o cos(3\varphi)$.

flexural frequency is also maximized. Due to their having the same $\Delta M_{nominal}/M_{nominal}$ ratio, the 300μm-thick and 3,000μm-thick CINGs have nearly the same normalized eigenvector values and Z. However, due to the difference in the angular gain A_g, the 3,000μm device is expected to have ~10 times lower vibration sensitivity than the 300μm device.

(a) Force pattern under y-axis angular acceleration

(b) Excited wineglass mode pattern
Figure 7.23. Force direction under y-axis angular acceleration and displacement pattern of the $n=2$ wineglass mode.

Figure 7.24. Cross-sectional view of CING with modeled mass imbalance. The density of the top 1/5th of the cylinder wall between $\varphi = $ -6~6° and $\varphi = $ 174~186° differs by -10% and 10% from the normal density.

Figure 7.25. Simulated normalized displacement amplitude ratios of 300μm- and 3000μm-thick CINGs with $sin\varphi$ (φ: azimuthal angle) mass distribution. Nominal mass imbalance ratio ($\Delta M_{nominal}/M_{nominal}$) of 0.1% is modeled by altering the density of top $1/5^{th}$ of the cylinder wall for φ: 6~6° and 174~186° by -10% and 10% from the normal density.
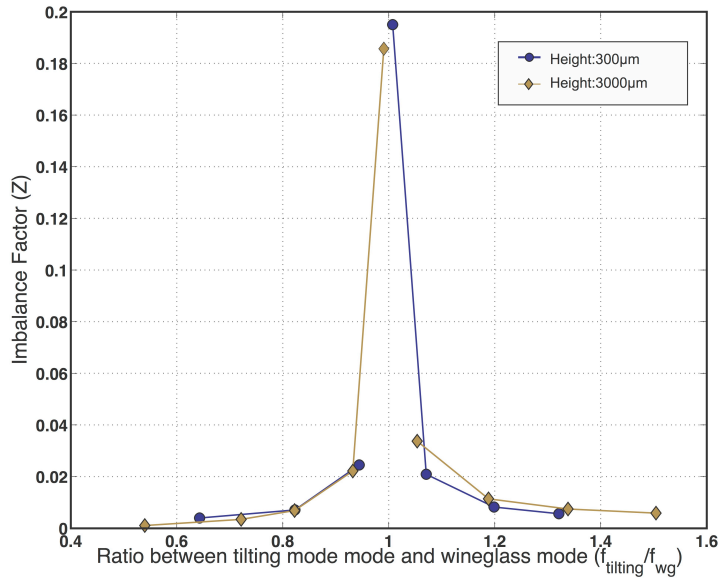
Figure 7.26. Simulated imbalance factors (Z) of 300μm- and 3000μm-thick CINGs with $sin\varphi$ (φ: azimuthal angle) mass distribution. Nominal mass imbalance ratio ($\Delta M_{nominal}/M_{nominal}$) of 0.1% is modeled by altering the density of top $1/5^{th}$ of the cylinder wall for φ between -6~6° and 174~186° by -10% and 10% from the normal density.

7.6. Discussion of Design Methodology for Achieving Lower Vibrational Sensitivity

7.6.1. Comparison Between CING and BOG's Vibration Sensitivity

Vibration sensitivity reduces as the amount of structural imbalance is reduced, the frequency difference between the parasitic and operational modes is increased, and the scale factor is increased. In the current generation of the BOG, the sense and the parasitic sense modes exist at 8.7kHz and 9.3kHz, respectively. In the first-generation (high-frequency) CING, the wineglass mode exists at 17.3kHz and the closest parasitic mode, the tilting mode, exists at over 30kHz. In the second-generation (low-frequency) CING, the wineglass mode is at 3kHz, and the lowest parasitic mode, the tilting mode, exists at 5kHz.

The frequency characteristic of the CING is advantageous for achieving smaller vibration stability. However, the fabrication accuracy of the BOG is better than the CING, and scale factor of the BOG is larger than the CING. The BOG is fabricated using a planar Si-on-glass (SOG) process, and the stiffness imbalance occurs only from the difference in the amount of lateral etching in DRIE process. In the current SOG process, the amount of mismatch in lateral etching is less than ~1μm. In the CING is made using SOG process that creates the bottom plate of the multi-ring cylinder using time-based DRIE process. The nonuniformity in the bottom plate is at least several microns within a device. In addition, the angular gain factor (k) of the BOG (1) is much larger than the k of the CING (0.02~0.1). Therefore, in order to improve the CING's vibration sensitivity, it is necessary to develop microfabrication process with better accuracy and to improve the geometry to achieve larger k.

7.6.2. Comparison of Vibration Sensitivity of the BOG and CING to Existing MEMS Gyros

We compare the BOG and the CING with existing gyroscopes with similar geometries, the butterfly gyroscope [84] and the ring gyroscope [7], respectively. The butterfly gyroscope, shown in Figure 7.27, consists of four driving springs, two sensing springs, a single coupling spring serving along both driving and sensing axes, and two anchors. Figure 7.28 describes the displacement patterns of the three lowest resonance modes of the butterfly gyro. The parasitic sensing mode is found at the lowest frequency (6kHz), and in this mode, the coupling spring does not provide any stiffness. The second mode is the driving mode (9kHz). In this mode, effective stiffness is provided from the driving and coupling springs. The third mode is the sensing mode (9.3kHz). In this mode, torsion occurs in both the sensing and coupling springs.

In the butterfly gyroscope, the coupling spring provides larger frequency separation (3.3kHz) than the CING (600Hz), leading to better vibration insensitivity. A possible drawback of the butterfly gyro, though, may include weakness to large shock, because the parasitic sensing mode is always located below the operating modes. The coupling spring of the butterfly gyro is a simple torsional beam, and it cannot make the parasitic sensing mode frequency larger than the operating mode frequencies.

The vibration sensitivity of the CING is compared with the ring gyroscope [7]. Figure 7.29 shows the displacement patterns of the ring gyro in four lowest resonance modes, simulated using ANSYS. The simulated ring has a radius of 2.5mm, a ring thickness of 40μm, an anchor radius of 1mm, and a height of 300μm.
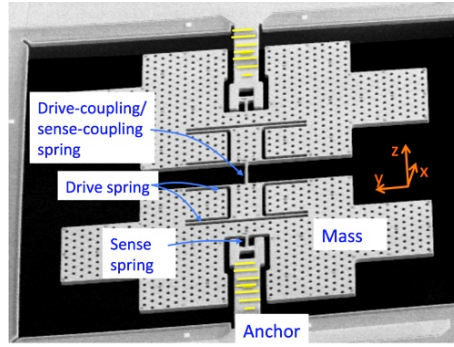
Figure 7.27. SEM picture of butterfly gyro [84].
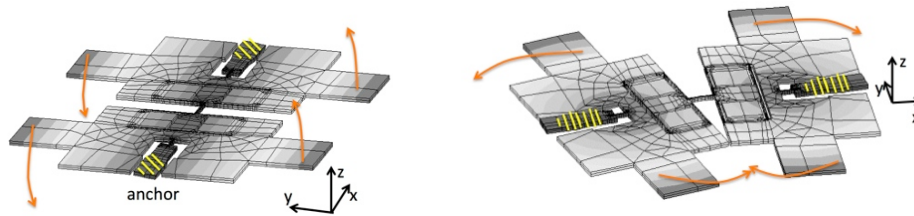
(a) Parasitic sense mode (6kHz)

(b) Driving mode (9kHz)
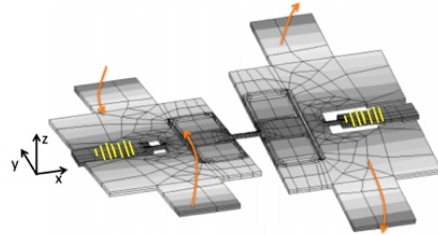
(c) Sensing mode (9.3kHz)

Figure 7.28. Parasitic sensing mode, driving mode, and sensing mode of the butterfly gyro [84].

The translational mode ($f_{translation}$), rotational mode ($f_{rotation}$), wineglass mode (f_{WG}), and tilting modes ($f_{tilting}$) are found at 8.1kHz, 8.2kHz, 10.5kHz, and 16.3kHz, respectively. The $f_{translation}$, $f_{rotation}$, and f_{WG} are determined by radius, ring thickness, and support beam thickness. In this architecture, the support springs, connecting the anchor to the ring, have to have minimal stiffness in order to keep the two wineglass mode frequencies as close as possible. Due to the small stiffness of the support spring, the $f_{translation}$ and $f_{rotation}$ are always lower than the f_{WG}. The $f_{tilting}$ and the vertical mode frequency ($f_{vertical}$) (not shown in Figure 7.29) reduce as the device height. Comparing the CING's modal characteristics with the ring gyro's modal characteristic, we find that

230

CING offers a larger $f_{parasitic}/f_{WG}$ ratio than the ring gyro; however, the advantage of the ring gyro over the CING for the given device height (300µm) is 5~40 times higher angular gain (A_g). The fabrication process for the ring gyro is planar so it can be more accurate than the fabrication process of the CING. In order to improve the vibration sensitivity of the CING, it is necessary to develop more accurate fabrication process and need to improve the A_g.
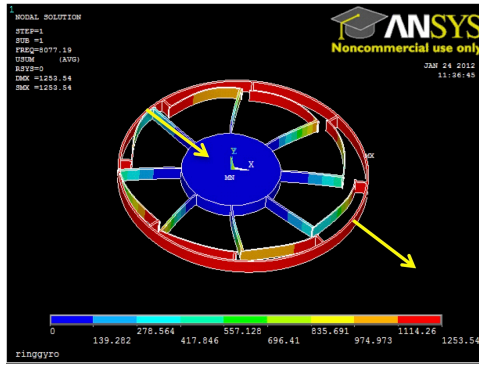
(a) Translational mode (8.1kHz)   (b) Rotational mode (8.2kHz)
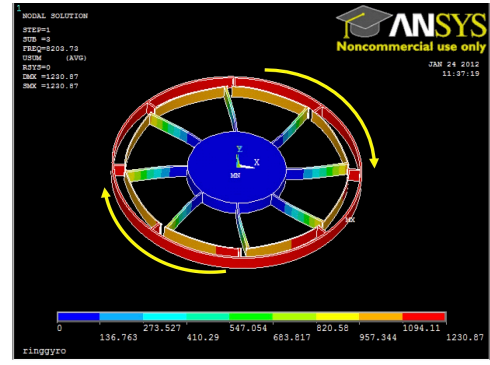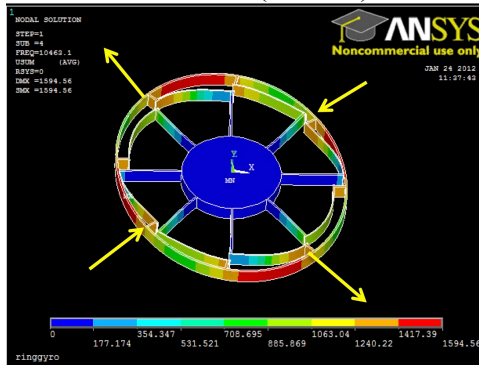
(c) Wineglass mode (10.5kHz)   (d) Tilting mode (16.3kHz)
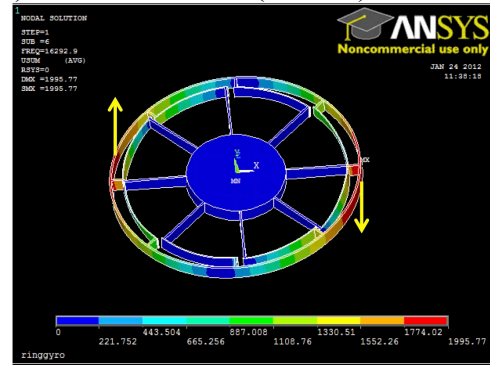
Figure 7.29. Displacement pattern of four lowest mode shapes (translational mode, rotational mode, wineglass mode, and tilting mode) of the ring gyroscope. The outer radius is 2.5mm, ring thickness is 40µm, anchor radius is 1mm, and height is 300µm.

7.7. Summary

We analyzed the relationship between the ratio of the frequency of a parasitic mode and a sense mode and the sensitivity to the vibrational pattern that excites the specific

parasitic resonance mode. It is found that the structural imbalance factor Z reaches a maximum value for a rate gyroscope as $f_{parasitic}/f_{sense}$ reaches 1.

To reduce the vibrational sensitivity at f_{sense}, it is necessary to separate $f_{parasitic}$ as far as possible from f_{sense}. The disadvantage in of lowering the $f_{parasitic}$ is reduced shock resistance, since the amount of generated stress increases under larger displacement [154]. The frequency separation is limited by the mode frequencies which depend on the topology of the geometry.

When we compare the Balanced Oscillating Gyroscope (BOG) with the Cylindrical Rate-Integrating Gyro (CING), the CING offers larger separation between the parasitic modes the operational modes. However, the vibration sensitivity of the CING is affected by structural imbalance from the current Si-on-glass (SOG) process and a small angular gain A_g. In order to achieve better vibration insensitivity, the CING need to be made with a microfabrication process with better accuracy and larger aspect ratio. A better coupling-beam design for the BOG needs to be researched to achieve larger separation between the operational modes from the parasitic modes.

CHAPTER 8.

CONCLUSIONS AND FUTURE DIRECTIONS

8.1. Summary

This work investigated the gyroscope design methodologies for reduced vibrational sensitivity. In order to achieve improved vibrational sensitivity, a gyro needs to have balanced modes in its driving and sensing modes. In the balanced mode, the sum of the linear and angular momentum are zero. The balanced mode cannot be excited from in-phase force generated from environmental acceleration. However, a gyro always has imbalance in stiffness and mass, so imperfectly balanced modes (i.e. out-of-phase mode) become excitable under in-phase acceleration. From analytical and numerical studies, the vibrational sensitivity at the out-of-phase mode reaches to its maximum value when $f_{parasitic}$ and f_{sense} are matched.

In order to reduce the vibrational sensitivity, the sensor needs to have a large frequency separation between $f_{parasitic}$ and f_{sense}. Since shock resistance of a gyro is roughly inversely proportional to the $f_{parasitic}$, it is desirable to place $f_{parasitic}$ higher than f_{sense}.

This design principle is applied to develop two new MEMS gyroscopes, the Balanced Oscillating Gyroscope (BOG) and the Cylindrical Rate-Integrating Gyroscope (CING). In the BOG, the structure of the sense-coupling beam is studied extensively to have larger $f_{parasitic}/f_{sense}$ ratio. The CING geometry is developed from the cylinder

geometry to increase vertical stiffness of the bottom plate to have larger $f_{tilting}/f_{WG}$ and $f_{vertical}/f_{WG}$ ratios. The two devices are fabricated using two different silicon-on-glass (SOG) processes.

The functionality of the BOG is proved by interfacing the sensor with the first-generation off-chip interface circuitry. Without having the bottom electrode for cross-stiffness balancing and quadrature cancellation loop, the minimum separation between the f_{drive} and f_{sense} is found to be 5Hz, and the sensor resolution is limited by quadrature error and noise in the driving loop to 0.56deg/sec/√Hz.

Two versions of Cylindrical Rate-Integrating Gyroscope (CING) are developed to operate at 18kHz and 3kHz, respectively. The CING geometry offers complete axisymmetry and the gyro mass can be self-aligned with all the side electrodes. The CING geometry offers good frequency separation ($f_{tilting}/f_{WG}$ ~ 1.5), but due to large motional energy along the vertical direction, the angular gain (A_g) is smaller than 0.03. The small A_g limits the accuracy of the sensor in both rate and rate-integrating mode. The 3kHz-CING has a matched τ_o of 8 seconds (Q~72,000) at frequency mismatch of <20mHz. The Q is limited by thermoelastic damping (TED). Using digital rate and rate-integrating mode circuitry, the second-generation CING performes with an angle random walk (ARW) of 0.09deg/√hr and bias drift of 129°/hr in the rate-sensing mode, and the sensor demonstrates precession with an angular gain (A_g) of 0.011±0.001 in the rate-integration mode for several hours with frequency mismatch of 20mHz to 80mHz.

8.2. Thesis Contribution

The presented work is believed to form a foundation for future development of low-vibrational sensitivity and high-resolution micro rate-integrating gyroscopes. The specific contributions of the presented research include:

1) Detailed comparison between the principle, control, device design, and discussion of practical limitations in MEMS rate and rate-integrating gyroscopes.

2) Analytical derivation and numerical simulation of the relationship between the modal characteristics ($f_{parasitic}/f_{sense}$) and vibrational sensitivity at the sense mode (f_{sense}) of both balanced tuning-fork gyro and wineglass-mode gyroscopes with structural anisotropy.

3) Detailed comparison of mechanical characteristics (modal characteristics, effective mass, angular gain (A_g), and centrifugal mass) and microfabricational simplicity of various 3D axisymmetric resonator shapes.

4) Design, fabrication, and demonstration of the self-aligned, fully axisymmetric, 3D, single-crystal-Si Cylindrical Rate-Integrating Gyroscope (CING). Analysis of relationship between modal characteristics with geometrical parameter of the gyro. Demonstration of both the rate-mode and rate-integrating mode operation using 3kHz-CING with τ_o of ~8 seconds under <20mHz mode matching. Demonstration of scale factor accuracy (A_g) in rate-integrating mode operation. Demonstration of mode matching within <80mHz for several days of use at uncontrolled temperature. Rate mode operation with angle random walk (ARW) of 0.09deg/√Hr and bias drift of 129°/Hr at ~40°C in vacuum (<5mTorr) (device performance is limited by A_g).

5) Design, fabrication, and demonstration of operation of the Balanced Oscillating Gyroscope (BOG). Detailed analysis of mechanism of sense coupling stiffness for increasing $f_{parasitic}/f_{sense}$ ratio to reduce vibration sensitivity at f_{sense}. Development of a new SOG process with thick Al layer with enhanced thermal conduction and charge dissipation during DRIE step. Demonstration of sensor measurement using first-generation interface circuit (without quadrature compensation) at noise level of 0.44°/sec/√Hz (device performance is limited by quadrature error and circuit noise).

8.3. Future Work

The performance of the CING is limited by its low angular gain (A_g). Since the A_g is related to the aspect ratio of the device, it is practically difficult to improve the A_g of the CING above the current level. In order to have a good rate-integration performance, it will be necessary to develop a new geometry with less vertical motion during the flexural mode.

More CING devices should be tested to better understand the physical source of the mechanical coupling that shifted the resonance frequency and quality factor of the gyro, following the polarity of the input rotation rate.

The 1st generation BOG that is presented in this thesis has a limitation in cross-axis stiffness balancing. With addition of balancing electrodes, the modes will become matchable. The performance of the new generation gyroscope should be tested extensively under various vibrational inputs.

Lastly, the SOG gyros should be wafer-level packaged using anodic bonding methods, and it will be tested on a mechanical isolation package.

APPENDICES

APPENDIX A

DERIVATION OF STIFFNESS AND DAMPING MATRICES IN SENSOR COORDINATE

The stiffness matrix of a sensor coordinate that is separated from the principal stiffness axis by θ_ω is found by 1) expressing a potential energy $E_{stiffness}$ in terms of principal stiffness, 2) transforming coordinates from the principal stiffness axes to the sensor axes, and 3) calculating the stiffness with respect to the sensor axis by double-differentiating the $E_{stiffness}$ in terms of displacement.

A.1. Stiffness Matrix

Assume a mass is moved from the origin to a coordinate (x, y) with respect to the principal stiffness axes (Figure A.1). The coordinate of the mass with respect to the sensor axis is called (q_1, q_2) (Figure A.2). The $E_{stiffness}$ is expressed in terms of k_1 and k_2 as:

$$E_{stiffness} = \frac{1}{2}k_1 x^2 + \frac{1}{2}k_2 y^2$$

(Equation A.1)

The relationship between the (x, y) and (q_1, q_2) is:

$$\begin{bmatrix} x \\ y \end{bmatrix} = \begin{bmatrix} \cos\theta_\omega & -\sin\theta_\omega \\ \sin\theta_\omega & \cos\theta_\omega \end{bmatrix} \begin{bmatrix} q_1 \\ q_2 \end{bmatrix}$$

(Equation A.2)

The stiffness terms with respect to the sensor coordinate is:

$$\begin{bmatrix} k_{11} & k_{12} \\ k_{21} & k_{22} \end{bmatrix}$$

(Equation A.3)

In Equation A.3, the stiffness k_{11}, k_{12}, k_{21}, and k_{22} are:

$$k_{11} = \frac{\partial}{\partial q_1}\left(\frac{\partial E_{stiffness}}{\partial q_1}\right)$$

(Equation A.4)

$$k_{12} = k_{21} = \frac{\partial}{\partial q_1}\left(\frac{\partial E_{stiffness}}{\partial q_2}\right)$$

(Equation A.5)

$$k_{22} = \frac{\partial}{\partial q_2}\left(\frac{\partial E_{stiffness}}{\partial q_2}\right)$$

(Equation A.6)
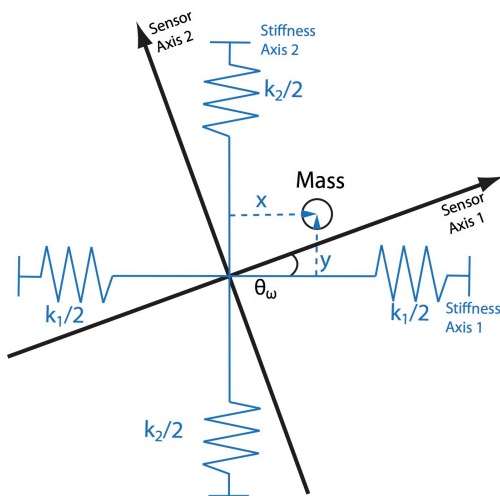
Figure A.1. Displacement in stiffness coordinate with respect to the principal stiffness axis.
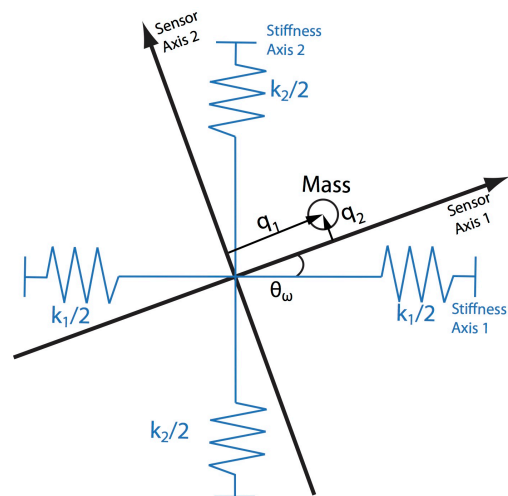
Figure A.2. Displacement in stiffness coordinate with respect to sensor axis.

The stiffnesses in the sensor coordinate k_{11}, k_{12}, k_{21}, and k_{22} are calculated as:

$$k_{11} = \frac{\partial}{\partial q_1}\left(\frac{\partial E_{stiffness}}{\partial q_1}\right) \qquad \text{(Equation A.7)}$$

$$= \frac{\partial}{\partial q_1}\left(\frac{\partial x}{dq_1}\frac{\partial E_{stiffness}}{dx} + \frac{\partial y}{dq_1}\frac{\partial E_{stiffness}}{dy}\right)$$

$$= \frac{\partial}{\partial q_1}\left(\cos\theta_\omega k_1 x + \sin\theta_\omega k_2 y\right)$$

$$= \frac{\partial}{\partial q_1}\left(\cos\theta_\omega k_1(\cos\theta_\omega q_1 - \sin\theta_\omega q_2) + \sin\theta_\omega k_2(\sin\theta_\omega q_1 + \cos\theta_\omega q_2)\right)$$

$$= k_1\cos^2\theta_\omega + k_1\sin^2\theta_\omega$$

$$k_{22} = \frac{\partial}{\partial q_2}\left(\frac{\partial x}{dq_2}\frac{\partial E_{stiffness}}{dx} + \frac{\partial y}{dq_2}\frac{\partial E_{stiffness}}{dy}\right) \qquad \text{(Equation A.8)}$$

$$= \frac{\partial}{\partial q_1}\left(-\sin\theta_\omega k_1 x + \cos\theta_\omega k_2 y\right)$$

$$= k_1\sin^2\theta_\omega + k_2\cos^2\theta_\omega$$

$$k_{12} = k_{21} = \frac{\partial}{\partial q_2}\left(\frac{\partial x}{dq_1}\frac{\partial E_{stiffness}}{dx} + \frac{\partial y}{dq_1}\frac{\partial E_{stiffness}}{dy}\right) \qquad \text{(Equation A.9)}$$

$$= \frac{\partial}{\partial q_2}\left(\cos\theta_\omega k_1(\cos\theta_\omega q_1 - \sin\theta_\omega q_2) + \sin\theta_\omega k_2(\sin\theta_\omega q_1 + \cos\theta_\omega q_2)\right)$$

$$= -k_1\sin\theta_\omega\cos\theta_\omega + k_2\sin\theta_\omega\cos\theta_\omega$$

C.2. Damping Matrix

Assume a mass is moving at a velocity vector ($\dot{x}$, $\dot{y}$) with respect to the principal damping axes. The velocity vector corresponds ($\dot{q}_1$, $\dot{q}_2$) with respect to the sensor coordinate.
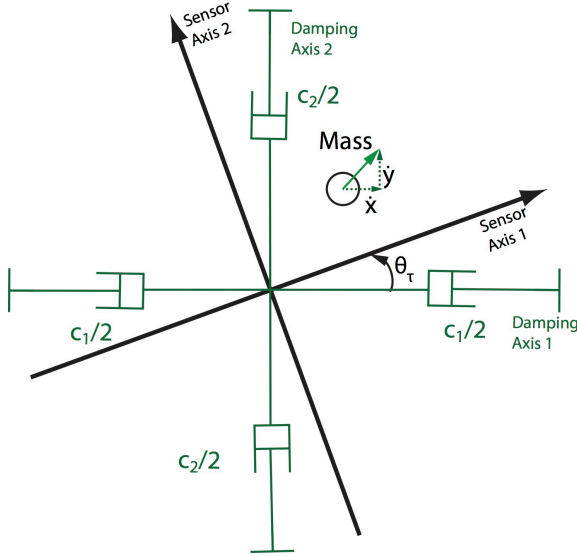
Figure A.3. Velocity of a mass with respect to principal damping axes.
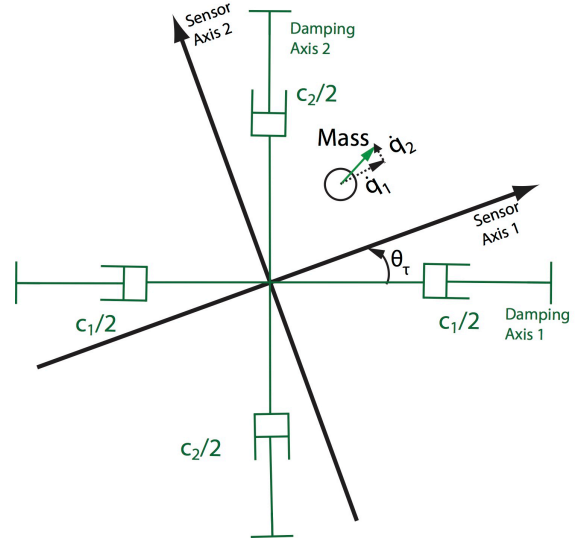
Figure A.4. Velocity of a mass with respect to sensor axes.

The change in the damping energy ($dE_{damping}$) is expressed in terms of the forces and displacements with respect to the stiffness axes as:

$$dE_{damping} = F_x dx + F_y dy$$
$$= c_x \dot{x} dx + c_y \dot{y} dy$$

(Equation A.10)

The damping coefficient matrice along the sensor axes is:

$$\begin{bmatrix} c_{11} & c_{12} \\ c_{21} & c_{22} \end{bmatrix}$$

(Equation A.11)

In Equation A.11, the coefficients c_{11}, c_{22}, c_{12}, and c_{21} are calculated as:

$$c_{11} = \frac{\partial}{\partial \dot{q}_1}\left(\frac{\partial E_{damping}}{\partial q_1}\right)$$

(Equation A.12)

$$c_{12} = \frac{\partial}{\partial \dot{q}_1}\left(\frac{\partial E_{damping}}{\partial q_2}\right)$$

(Equation A.13)

$$c_{21} = \frac{\partial}{\partial \dot{q}_2}\left(\frac{\partial E_{damping}}{\partial q_1}\right)$$

(Equation A.14)

$$c_{22} = \frac{\partial}{\partial \dot{q}_2} \left(\frac{\partial E_{damping}}{\partial q_2} \right)$$

The damping coefficients are calculated as:

$$c_{11} = \frac{\partial}{\partial \dot{q}_1} \left(\frac{\partial E_{damping}}{\partial q_1} \right)$$

$$= \frac{\partial}{\partial \dot{q}_1} \left(\frac{\partial x}{dq_1} \frac{\partial E_{damping}}{dx} + \frac{\partial y}{dq_1} \frac{\partial E_{damping}}{dy} \right)$$

$$= \frac{\partial}{\partial \dot{q}_1} \left(\cos\theta_\tau c_1 \dot{x} + \sin\theta_\tau c_2 \dot{y} \right)$$

$$= c_1 \cos^2\theta_\tau + c_2 \sin^2\theta_\tau$$

$$c_{22} = \frac{\partial}{\partial \dot{q}_2} \left(\frac{\partial E_{damping}}{\partial q_2} \right)$$

$$= c_1 \sin^2\theta_\tau + c_2 \cos^2\theta_\tau$$

$$c_{12} = c_{21}$$

$$= \frac{\partial}{\partial \dot{q}_2} \left(-c_1 \cos\theta_\tau \sin\theta_\tau \dot{q}_2 + c_2 \cos\theta_\tau \sin\theta_\tau \dot{q}_2 \right)$$

$$= -c_1 \cos\theta_\tau \sin\theta_\tau + c_2 \cos\theta_\tau \sin\theta_\tau$$

APPENDIX B

ANSYS CODE FOR PHYSICAL PARAMETER OF THE 3D WINEGLASS MODE GYROSCOPE

The following code lines are used to simulate the resonance frequency, angular gain, and

effective mass of a fused-silica hemispherical resonator.

```
finish
/CLEAR,START
/PREP7

!2-1.  The multiconcentric ring. Material: fused silica, element:  shell93, fused silica's
mechanical data found from (http://www.accuratus.com/fused.html)
Mat,1
et, 1, shell93
MPTEMP,,0  ! temperature
mp, ex, 1, 73e9
MP,NUXY,1,0.17
MPDATA,DENS,1,,2200
thickness = 100e-6          ! thickness of the shell
R,1,thickness               ! setting the thickness of the shell

*SET,tol,1e-7
btol, tol
radius1 = 1900e-6
radius2 = 500e-6
height  = 1000e-6
k,1,radius1,0,0
k,2,radius2,0,-height
k,3,radius2+0.5*(radius1-radius2),0,-0.8*height
LARC,2,1,3,
k,10000,0,0,0
k,10001,0,0,100e-6
ldiv = 36
adiv = 120
ldiv,1,,,ldiv
* do,i,1,ldiv,1,
```

```
AROTAT,i,,,,,,10000,10001,360,adiv
*enddo
ESIZE,,1          ! esize number and arotat division number needs to be same
AMESH,all
/eshape, 1        ! show element with the real thicknesses
nsel,all
nummerg, all, tol
csys,1
NSEL,s,LOC,x,radius2
D,ALL,ux,0
d,all,uy,0
d,all,uz,0
nsel,all
FINISH

/SOLU
ANTYPE,2                     ! analysis type = 2 (modal analysis)
MODOPT,LANB,20               ! Calculating 10 modes using Lanzos method
EQSLV,SPAR                   ! Using sparse equation solver
MXPAND,20, , ,1             ! Calculating element solutions for 10 modes
LUMPM,0                      ! Do not use lumped modeling
PSTRES,0                     ! no pre stress

MODOPT,LANB,20,0,0, ,OFF          ! Calculating 10 modes using Lanzos method
/STATUS,SOLU
SOLVE
FINISH

!7. Calculating effective mass along xyz
!7-1.  Going to postpressing mode and read the first set of solutions, which is the wine
glass mode
/post1
SET,,, ,,, ,3                !read the solution at first set (lowest frequency)
rsys,0                       !List or plot the solution along the coordinate 0 (global
Cartesisn)

!7-2.  Reading volume, displacements along x and y axes (UX, UY)
 AVPRIN,0,0.17 ,            ! calculates the element data by averaging the nodal data
ETABLE, ,VOLU,             ! calculates the element volume

!*
AVPRIN,0,0.17 ,
ETABLE,,U,X                 !calculates the x direction displacement
!*
AVPRIN,0,0.17 ,             ! calculates the element data by averaging the nodal data
ETABLE,,U,Y                 !calculates the y direction displacement
```

```
!*
AVPRIN,0,0.17 ,
ETABLE,,U,z                    !calculates the z direction displacement

!7-3.  Calculating UX^2, UY^2, and sum of square of displacements
SMULT,UX1^2,UX,UX,1,1,  ! Multiply UX by UX and store as the name of UX^2
SMULT,UY1^2,UY,UY,1,1,  ! Multiply UY by UY and store as the name of UY^2
SMULT,UZ1^2,UZ,UZ,1,1
SADD,UXUYSUM1,UX1^2,UY1^2,1,1,
SADD,UXUYUZSUM1,UXUYSum1,UZ1^2,1,1
PRETAB,volu,ux,uy,uz,UXUYUZsum1

!==================================================================
  !7-4.  max(UXUYUZSum1)= 0.20867E+07    sqrt( max(UXUYUZSum1))
=1444.54145
!==================================================================

 !7-5.  Normalize UX and UY using the Sqrt(MAX(USSUM1))
! Multiply UX by 1/max(ux), and store as the name of NORx
SMULT,norx1,Ux, ,1/1444.54141    ,1,
! Multiply UX by 1/max(uy), and store as the name of NORy
SMULT,nory1,Uy, ,1/1444.54145    ,1,
! Multiply UX by 1/max(uz), and store as the name of NORZ
SMULT,norz1,Uz, ,1/1444.54145    ,1,
! Multiply NORX by NORX and store as the name of NORX^2
SMULT,norx1^2,NORx1,NORx1,1,1,
! Multiply NORX by NORX and store as the name of NORy^2
SMULT,nory1^2,NORy1,NORy1,1,1,
! Multiply NORX by NORX and store as the name of NORz^2
SMULT,norz1^2,NORz1,NORz1,1,1,
! Sum NORX^2 and NORY^2 and store as a name of NORSxy
SADD,norsxy1,NORX1^2,NORY1^2,1,1,0,
! Sum NORsumXY and NORZ^2 and store as a name of NORSxyz
SADD,norsxyz1,Norsxy1,norz1^2,1,1,0
! Multiply NORSUM, Volume, and Density of fused silica (2220kg/m^3) and store as
EFFMASS
SMULT,effmass1,NORsxyz1,VOLU,2200,1,
! Print element solution in table and display the calculated values
PRETAB,volu,norx1,nory1,norz1,norsxyz1,EFFMASS1
 !11-6. Add each column on the displayed element solution table
ssum
!==================================================================
!
!11-7. From SSUM table, the sum of the effective mass elements is
!    0.478259E-06
!==================================================================
```

!7. Calculating effective mass along z
!7-1. Going to postpressing mode and read the first set of solutions, which is the wine
glass mode
/post1
SET,,, ,,, ,4   !read the solution at first set (lowest frequency)
rsys,0   !List or plot the solution along the coordinate 0 (global
Cartesisn)

!7-2. Reading volume, displacements along x and y axes (UX, UY)
AVPRIN,0,0.17 ,   ! calculates the element data by averaging the nodal data
ETABLE, ,VOLU,   ! calculates the element volume
AVPRIN,0,0.17 ,
ETABLE,,U,X   !calculates the x direction displacement
AVPRIN,0,0.17 ,   ! calculates the element data by averaging the nodal data
ETABLE,,U,Y   !calculates the y direction displacement
AVPRIN,0,0.17 ,
ETABLE,,U,z   !calculates the z direction displacement

!7-3. Calculating UX^2, UY^2, and sum of square of displacements
! Multiply UX by UX and store as the name of UX^2
SMULT,UX2^2,UX,UX,1,1,
! Multiply UY by UY and store as the name of UY^2
SMULT,UY2^2,UY,UY,1,1,
SMULT,UZ2^2,UZ,UZ,1,1
! Add UX^2 and UY^2 and store as USSUM (=u square sum)
SADD,UXUYSUM2,UX2^2,UY2^2,1,1,
SADD,UXUYUZSUM2,UXUYSum2,UZ2^2,1,1
! Print element solution in table and display volume, UX, UY, and USSUM
PRETAB,volu,ux,uy,uz,UXUYUZsum2
!===
!7-4. max(UXUYUZSum2)= 0.20867E+07 sqrt(max(UXUYUZSum2)) = 1444.54141
!===

!7-5. Normalize UX and UY using the Sqrt(MAX(USSUM1))
! Multiply UX by 1/max(ux), and store as the name of NORx
SMULT,norx2,Ux, ,1/1444.54141   ,1,
! Multiply UX by 1/max(uy), and store as the name of NORy
SMULT,nory2,Uy, ,1/1444.54141   ,1,
! Multiply UX by 1/max(uz), and store as the name of NORZ
SMULT,norz2,Uz, ,1/1444.54141   ,1,
! Multiply NORX by NORX and store as the name of NORX^2
SMULT,norx2^2,NORx2,NORx2,1,1,
! Multiply NORX by NORX and store as the name of NORy^2
SMULT,nory2^2,NORy2,NORy2,1,1,
! Multiply NORX by NORX and store as the name of NORz^2

SMULT,norz2^2,NORz2,NORz2,1,1,
! Sum NORX^2 and NORY^2 and store as a name of NORSxy
SADD,norsxy2,NORX2^2,NORY2^2,1,1,0,
! Sum NORsumXY and NORZ^2 and store as a name of NORSxyz
SADD,norsxyz2,Norsxy2,norz2^2,1,1,0
! Multiply NORSUM, Volume, and Density of fused silica (2220kg/m^3) and store as EFFMASS
SMULT,effmass2,NORsxyz2,VOLU,2200,1,
! Print element solution in table and display the calculated values
PRETAB,volu,norx2,nory2,norz2,norsxyz2,EFFMASS2

 !11-6. Add each column on the displayed element solution table
ssum
!===
!11-7. From SSUM table, the sum of the effective mass elements is
 ! 0.478259E-06
!===

!!**********Save the tables for the calculation of the angular gain **************
!12-8. Calculate NORX1*NORY2 - NORX2*NORY1
! Multiply NORX1 by NORY2 and store as the name of NORX1Y2
SMULT,NORX1Y2,NORX1,NORY2,1,1,
! Multiply NORX2 by NORY1 and store as the name of NORX2Y1
SMULT,NORX2Y1,NORX2,NORY1,1,1,
! Subtract NORX2Y1 from NORX1Y2 and store as the name of NORSUB
SADD, NORSUB,NORX1Y2,NORX2Y1,1,-1,0,
! Multiply NORSUB, Volume, and Density of Si (2330kg/m^3) and store as NORSUB
SMULT,Gamma,NORSUB,VOLU,2200,1
! Print element solution in table and display the calculated values
PRETAB,volu,NORX1Y2, NORX2Y1, NORSUB,Gamma

!12-9. Add each column on the displayed element solution table
ssum
!===
!12-10. From SSUM table, the sum of the gamma is
 ! 0.150500E-06 , therefore, the angular gain is 150.5/2/478 (average of effective mass)=0.23
!===

APPENDIX C

DESIGN OF VERTICAL COMB DRIVE (VC) ELECTRODES FOR SILICON-ON-GLASS (SOG) PROCESS

The vertical comb-drive (VC) electrode is used to measure vertical deflection and to actuate masses along the out-of-plane direction. The electrodes are fabricated using the Si-on-glass (SOG) process with thermal dissipation bumps [125] (Figure 4.27). The electrodes have larger out-of-plane actuation range than the parallel plate by not suffering from pull-in phenomenon.

The electrodes are formed by localized anodic bonding, induced by electrostatic pull-in, at step (e) of Figure 4.27. The rest of the device is prevented from bonding by the glass bumps. While the VC electrodes here were designed to be compatible with the SOG process, a similar technique is believed to be useful for sensors made from a SOI substrate.

The VC electrodes consist of comb drive electrodes, bonding plate, torsion spring, torsion bar, and anchor. The bonding plate defines where the anodic bonding takes place. The plate is connected to torsion springs and torsion bars that provide flexibility in the vertical direction. We can configure the structure of the VC electrode to be placed both at a lower level and a higher level than the normal level of the sensor mass. These comb drive electrodes are named the pull-down vertical comb drive electrode (PDVC) and the pop-up vertical comb drive electrode (PUVC), respectively (Figure C.1)

Cross-section of the VC electrode along AA'

(a) Lower-level vertical comb drive (PDVC)

(b) Cross section BB' of pop-up VC structure

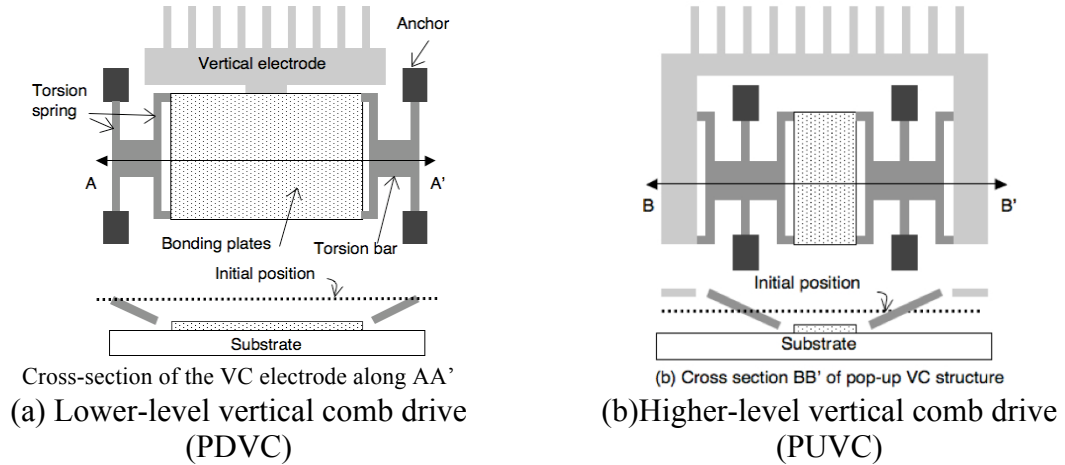(b)Higher-level vertical comb drive (PUVC)

Figure C.1. Structures and dimensions of the of the lower-level pull-down vertical comb drive (PDVC) and higher-level pull-up vertical comb drive (PUVC).

The PDVC has anchors and torsion beams at both sides. The bonding plate is located at the center of the device, and the bonding plate as well as the comb drive electrodes are made to be pulled down on the glass recess. In the PUVC, levers are made from the bonding plate to the electrodes. When the bonding plate is pulled down, the electrodes are pushed up with a vertical amplification factor determined by the ratio of the lever. To prevent the electrodes from being pulled down together with the bonding plate, it is necessary to provide a sheet of conducting material with the same potential as the vertical electrodes underneath the electrodes.

The vertical stiffness of the VC electrode is determined by the width (w) and length (l) of the narrow beams as well as the length of the lever (L). The thin beams bend laterally along the x-axis as well as tilt along the y-axis when the bonding plate is subjected to a vertical force. Due to the complex nature of the deformation of these narrow beams, the dimensions of the VC electrode are designed with the FEM method.

The design criteria of the VC electrodes are 1) reasonable pull-in voltage (<1000V), 2) von-Mises stress under the fracture stress of Si, and 3) for the PUVC, vibration stability, based on having the lowest resonance frequency be over 100kHz. An expression for the

dimensions required to meet the first criterion can be derived from the expression for pull-in voltage. The pull-in voltage ($V_{pull-in}$) is related to the area of the bonding plate (A), recess gap (d), vertical stiffness (k_z) by:

$$V_{pull-in} = \sqrt{\frac{8}{27} \frac{k_z d^3}{\varepsilon A}}$$ (Equation C.1)

With a nominal gap of 5μm, and the maximum pull-in voltage of <1000V, the relation between A and k_z are then expressed as:

$$
\begin{aligned}
k_z(N/m) \;&< \frac{27}{8} \times \frac{\varepsilon(V_{pull-in})^2}{d^3} A \\
&= \frac{27}{8} \times \frac{(8.85E-12)(1E3)^2}{(5E-6)^3} A \\
&= (2.39E11) \times A(m^2)
\end{aligned}
$$ (Equation C.2)

According to this relation, the maximum stiffness for a bonding plate with an area A of 2500μm^2 (= 50x50μm^2) is about 600N/m. As will be shown later, such vertical stiffness is readily achieved with VC electrodes consisting of bending/torsional beams with a width (w) of about 5μm, length (l) of 100μm, and a height (h) of 100μm.

The dimensions for meeting the second and third criteria are selected with the FEM method. Table C.1 shows the typical dimension of the electrode meeting our design goals. Figures C.2 (a) and (b) show the FEM model of the PDVC and PUVC, respectively. Figure C.3 shows the modeling results for a PDVC drive modeled using ANSYS. Figure C.4 shows modeling results for a PUVC drive modeled using ANSYS. Figure C.5 shows a SEM photograph of both types of the VC electrodes. Both simulation results indicate that the electrodes developed here are robust enough for inertial sensing applications with a resonance frequency under 50kHz. Further development may improve robustness if an application requires it. Figure C.6 shows a SEM photograph of

a torsion actuator created using the developed SOG process where the VC electrodes are used to provide force in the vertical direction.

Table C.1 Typical dimension of the designed pull-down (PDVC) and pop-up vertical electrodes (PUVC) (can be further optimized)

VC Type	Pull-Down Vertical Comb Drive (PDVC)	Pop-Up Vertical Comb Drive (PUVC)
A (bonding area) (μm^2)	5×10^4	5×10^4
w (width of the narrow beam) (μm)	4	4
l (length of narrow beam) (μm)	110	110
L (length of lever) (μm)	110	110
Max von-Mises stress (GPa) (with vertical deflection: 10μm)	0.65	0.65
Resonance frequency (with vertcial deflection: 10μm)	NA	90kHz (lateral mode)
k_z (vertical stiffness) (N/m)	233	275
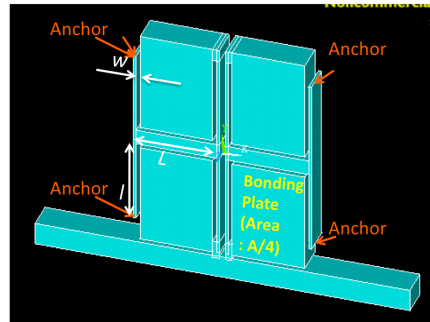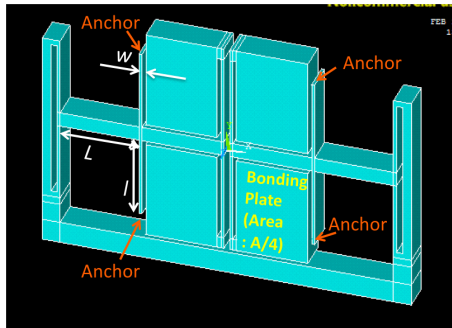
(a) Pull-down vertical comb drive (PDVC)   (b) Pop-up vertical comb crive (PUVC)
Figure C.2. Vertical comb drive electrodes compatible with the Si-on-Glass (SOG) process.
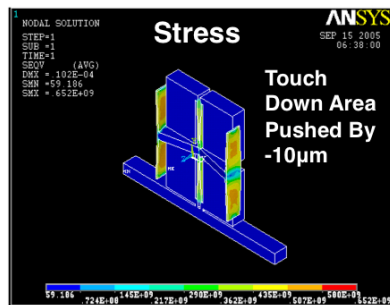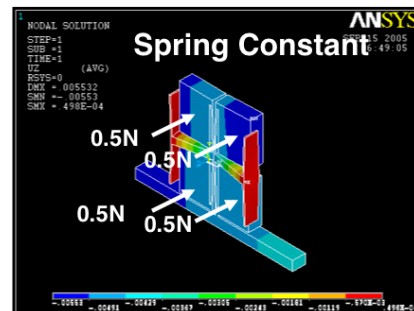
(a) Maximum von-Mises stress of 0.65GPa under vertical deflection of 10μm (b) Vertical stiffness: 233N/m

Figure C.3. Calculation of mechanical properties of the PDVC architecture using FEM (width: 488μm, length: 300μm, minimum beam width (w): 4μm).
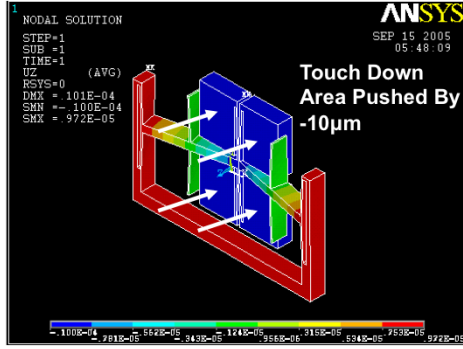
(a) Vertical deflection of 10µm when the bonding plate is pushed down by 10µm
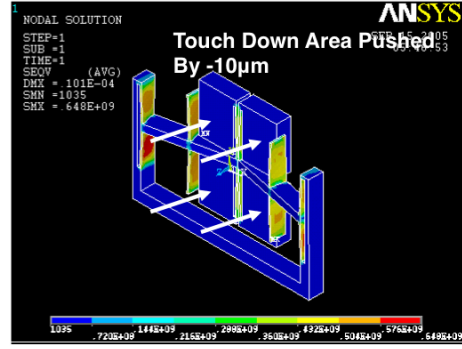
(b) Maximum von-Mises stress of 0.65GPa under vertical deflection of 10µm
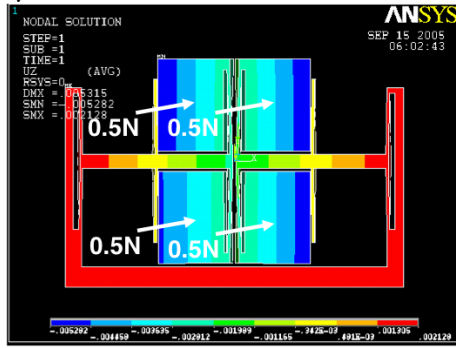
(c) Vertical stiffness of 275N/m
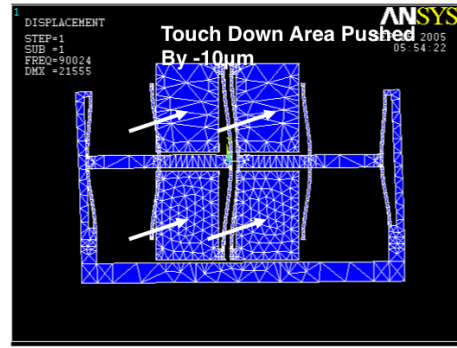
(d) Lowest-order resonance mode (lateral translation) at 90kHz

Figure C.4. Calculation of mechanical properties of the PUVC architecture with FEM (width: 496µm, length: 335µm, minimum beam width (w): 4µm).
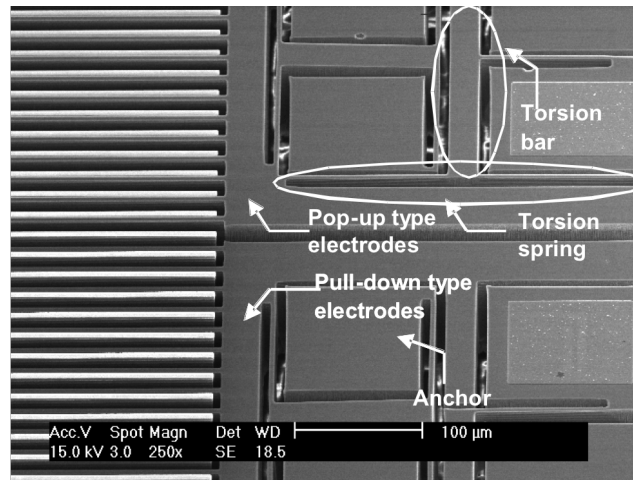
Figure C.5. SEM photograph of both pop-up (PUVC) and pull-down (PDVC) vertical comb electrodes.
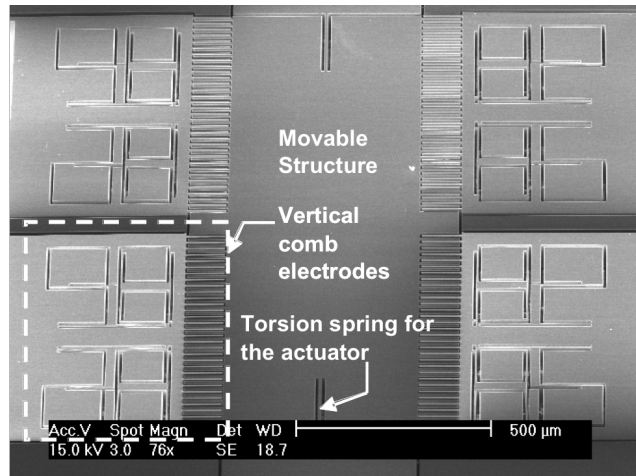
Figure C.6. SEM photograph of a torsion actuator where the vertical comb drive electrodes are used.

BIBLIOGRAPHY

BIBLIOGRAPHY

[1]   D. H. Titterton and J. L. Weston, *Strapdown Inertial Navigation Technology*. Stevenage, U.K.: Institution of Electrical Engineers, 2004.

[2]   V. H. Aske, "The MHD/magnetohydrodynamic/two-axis Rate Sensor," in *American Institute of Aeronautics and Astronautics (AIAA) Aircraft Systems Meeting*, Anaheim, CA, 1980, pp. 1-6.

[3]   N. Yazdi, F. Ayazi, and K. Najafi, "Micromachined inertial sensors," *Proceedings of the IEEE*, vol. 86, no. 8, pp. 1640-1659, 1998.

[4]   A. Kourepenis, J. Borenstein, J. Connelly, R. Elliott, P. Ward, and M. Weinberg, "Performance of MEMS inertial sensors," in *IEEE Position Location and Navigation Symposium*, Palm Springs, CA, 1998, pp. 1-8.

[5]   P. Greiff, B. Boxenhorn, T. King, and L. Niles, "Silicon monolithic micromechanical gyroscope," in *Proc. International Conference on Solid-State Sensors and Actuators (Transducers '91)*, San Francisco, CA, 1991, pp. 966-968.

[6]   J. Bernstein, S. Cho, A. T. King, A. Kourepenis, P. Maciel, and M. Weinberg, "A micromachined comb-drive tuning fork rate gyroscope," in *Proc. IEEE Inverstigation of Micro Structures, Sensors, Actuators, Machines and Systems (MEMS'93*), Fort Lauderdale, FL, 1993, pp. 143-148.

[7]   M. W. Putty, "A Micromachined Vibrating Ring Gyroscope," Ph.D. dissertation, Dept. Elect. Eng. and Comp. Sci., Univ. Michigan, Ann Arbor, MI, 1995.

[8]   W. A. Clark, "Micromachined Z-axis vibratory rate gyroscope," Ph.D. dissertation, Dept. Elect. Eng., Univ. California-Berkeley, Berkeley, CA, 1997.

[9]   T. Juneau, A. P. Pisano, and J. H. Smith, "Dual axis operation of a micromachined rate gyroscope," in *Proc. International conference on Solid-State Sensors and Actuators (Transducers'97)*, Chicago, IL, 1997, pp. 883-886.

[10]   I. Hopkin, "Performance and design of a silicon micromachined gyro," in *Proc. Symp. Gyro Technology*, Stuttgart, Germany, 1997, pp. 1.0-1.10.

[11]   M. Weinberg, J. Connelly, A. Kourepenis, and D. Sargent, "Microelectromechanical instrument and systems development at the Charles Stark Draper Laboratory, Inc," in *Proc. 16th IEEE Digital Avionics Systems Conference*, Irvine, CA, 1997, pp. 8.5.34-8.5.40.

[12]   W. Geiger, B. Folkmer, J. Merz, H. Sandmaier, W. Lang, "A new silicon rate gyroscope," in *Proc. 11th IEEE International Conference on Micro Electro Mechanical Systems (MEMS'98)*, Heidelberg, Germany, 1998, pp. 615-620.

[13] K. Schumacher, O. Krömer, U. Wallrabe, J. Mohr, and V. Saile, "Micromechanical LIGA-gyroscope," in *Proc. 10th International Conference on Solid-State Sensors and Actuators (Transducers' 99)*, Sendai, Japan, 1999, pp. 1574-1577.

[14] R. L. Kubena, D. J. Vickers-Kirby, R. J. Joyce, and F. P. Stratton, "New miniaturized tunneling-based gyro for inertial measurement applications," *J. Vacuum Science & Technology B: Microelectronics and Nanometer Structures*, vol. 17, no. 6, pp. 2948-2952, 1999.

[15] K. Y. Park, H. S. Jeong, S. An, S. H. Shin, H. Song, and C. W. Lee, "Lateral gyroscope suspended by two gimbals through high aspect ratio ICP etching," in *Proc. 10th International Conference on Solid-State Sensors and Actuators (Transducers '99)*, Sendai, Japan, 1999, pp. 972-975.

[16] H. Song, Y. S. Oh, I. S. Song, S. J. Kang, S. O. Choi, H. C. Kim, B. J. Ha, S. S. Baek, and C. M. Song, "Wafer level vacuum packaged de-coupled vertical gyroscope by a new fabrication process," *in Proc. 13th International Conference on Micro Electro Mechanical Systems (MEMS'00)*, Miyazaki, Japan, 2000, pp. 520-524.

[17] S. Kim, B. Lee, J. Lee, and K. Chun, "A gyroscope array with linked-beam structure," *in Proc. 14th International Conference on Micro Electro Mechanical Systems (MEMS'01)*, Interlaken, Switzerland, 2001, pp. 30-33.

[18] ADXRS614 Data Sheet, Analog Devices, Available: www.analog.com/static/imported-files/data_sheets/ADXRS614.pdf

[19] G. He and K. Najafi, "A single-crystal silicon vibrating ring gyroscope," *in Proc. 15th International Conference on Micro Electro Mechanical Systems (MEMS'02)*, Las Vegas, NV, 2002, pp. 718-721.

[20] S. Y. Bae, K. J. Hayworth, K. V. Shcheglov, K. Y. Yee, and D. V. Wiberg, "JPL's MEMS Gyroscope Fabrication, 8-Electrode Tuning, and Performance Results," in *Proc. Solid-state Sensor and Actuator Workshop (Hilton Head'02)*, Hilton Head, S.C., 2002, pp. 146-149.

[21] M. Palaniapan, R. T. Howe, and J. Yasaitis, "Performance comparison of integrated z-axis frame microgyroscopes," in *Proc. 16th International Conference on Micro Electro Mechanical Systems (MEMS'03)*, Kyoto, Japan, 2003, pp. 482-485.

[22] J. Kim, S. Park, D. Kwak, H. Ko, and D.-I. D. Cho, "A planar, x-axis, single-crystalline silicon gyroscope fabricated using the extended SBM process," in *Proc. 17th International Conference on Micro Electro Mechanical Systems (MEMS'04)*, Maastricht, Netherlands, 2004, pp. 556-559.

[23] D. Karnick, G. Ballas, L. Koland, T. Braman, M. Secord, E. Abbott, and T. Kourepenis, "Honeywell Gun-hard Inertial Measurement Unit (IMU)

Development," in *Proc. IEEE Position, Location, and Navigation Symposium (PLANS'04)*, pp.49-55, 2004.

[24] J. Y. Lee, S. H. Jeon, H. K. Jung, H. K. Chang, and Y. K. Kim, "Vacuum packaged low noise gyroscope with sub mdeg/s/sqrtHz resolution," in *Proc. 18th IEEE International Conference on Micro Electro Mechanical Systems (MEMS'05)*, Miami, FL, 2005, pp. 359-362.

[25] M. F. Zaman, A. Sharma, and F. Ayazi, "High Performance Matched-Mode Tuning Fork Gyroscope," in *Proc. 19th IEEE International Conference on Micro Electro Mechanical Systems (MEMS'06)*, Istanbul, Turkey, 2006, pp. 66-69.

[26] H. Johari and F. Ayazi, "High-frequency capacitive disk gyroscopes in (100) and (111) silicon," in *Proc. 20th IEEE International Conference on Micro Electro Mechanical Systems (MEMS'07)*, Kobe, Japan, 2007, pp. 47-50.

[27] M. F. Zaman, A. Sharma, and F. Ayazi, "A 0.1deg/Hr bias drift electronically matched tuning fork microgyroscope," in *Proc. 21st IEEE International Conference on Micro Electro Mechanical Systems (MEMS'08)*, Tucson, AZ, 2008, pp. 6-9.

[28] G-2000 Dynamically Tuned Gyroscope (DTG) Specification Sheet, Northrop Grumman.   Available: http://www.es.northropgrumman.com/solutions/g2000/assets/G-2000_Dynamically_Tuned_Gyro_.pdf

[29] E. J. Loper and D. D. Lynch, "Hemispherical resonator gyro- Status report and test results," in *Proc. Institute of Navigation National Technical Meeting*, San Diego, CA, 1984, pp. 105-107.

[30] R. Neul, U. Gomez, K. Kehr, W. Bauer, J. Classen, C. Doring, E. Esch, S. Gotz, J. Hauer, B. Kuhlmann, C. Lang, M. Veith, and R. Willig, "Micromachined gyros for automotive applications," in *Proc. IEEE Sensors 2005*, Irvine, CA, 2005, pp. 527-530.

[31] J. A. Geen, "Very Low Cost Gyroscopes," in *Proc. IEEE Sensors 2005*, Irvine, CA, 2005, pp. 537-540.

[32] W. W. Chow, J. Gea-Banacloche, L. M. Pedrotti, V. E. Sanders, W. Schleich, and M. O. Scully, "The ring laser gyro," *Reviews of Modern Physics*, vol. 57, no. 1, pp. 61-104, 1985.

[33] C. Volk, J. Lincoln, and D. Tazartes, "Northrop Grumman's Family of Fiber-Optic Based Intertial Navigation Systems," Available: http://www.es.northropgrumman.com/media/whitepapers/assets/FOGINS_Paper_Final.pdf

[34] B. C. Grover, E. Kanegsberg, J. G. Mark, and R. L. Meyer, "Nuclear magnetic resonance gyro," U.S Patent 4 157 495, June 5th, 1979.

[35] B. C. Grover, "Nuclear magnetic resonance gyroscope," U.S. Patent 4 430 616, Feb. 7th ,1984.

[36] T. L. Gustavson, P. Bouyer, and M. A. Kasevich, "Precision Rotation Measurements with an Atom Interferometer Gyroscope," *Physical Review Letters*, vol. 78, no. 11, pp. 2046-2049, 1997.

[37] M. Kasevich, "Science and technology prospects for ultra-cold atoms," Available: http://wwww.dmphotonics.com/Tekhnoscan/kasevich_CAMOS_021124.pdf".

[38] S. A. Jerebets, "Gyro evaluation for the mission to Jupiter," in *Proc. IEEE Aerospace Conference*, Big Sky, MT, 2007, pp. 1-9.

[39] K. Kumar, N. Barbour, and M. Weinberg, "UNCOMMON INERTIAL SENSING CONCEPTS REVISITED," in *Proc. AIAA Guidance, Navigation and Control Conference*, Baltimore, MD, 1995, pp. 524-535.

[40] A. Matthews and F. J. Rybak, "Comparison of hemispherical resonator gyro and optical gyros," *IEEE Aerospace and Electronic Systems Magazine*, vol. 7, no. 5, pp. 40-46, 1992.

[41] N. Barbour, "Inertial Components-Past, Present, and Future," in. *Proc. AIAA Guidance, Navigation and Control Conference*, Montreal, Canada, 2001, pp. 2001-

[42] Epson Toyocom Gyroscopes (XV series), Epson, Available: http://www.epsontoyocom.co.jp/english/tech/note/pdf/xv9000series_technote.pdf

[43] M. Yachi, H. Ishikawa, Y. Satoh, Y. Takahashi, and K. Kikuchi, "Design methodology of single crystal tuning fork gyroscope for automotive applications," in *Proc. IEEE Ultrasonics Symposium*, Sendai, Japan, 1998, pp. 463-466.

[44] S. Nasiri and J. Seeger, "XY axis dual-mass tuning fork gyroscope with vertically integrated electronics and wafer-scale hermetic packaging," U.S Patent 6 892 575, May 17th, 2005.

[45] I. P. Prikhodko, S. A. Zotov, A.A. Trusov, and A.M. Shkel, "Foucault Pendulum on a Chip: Rate Integrating Silicon MEMS Gyroscope" in *Proc. 24th IEEE International Conference on Micro Electro Mechanical Systems (MEMS'11)*, Cancun, Mexico, pp. 161-164.

[46] E. Sahin, S. E. Alper, and T. Akin, "Experimental Evaluation of Alternative Drive-Mode Control Electronics Developed for High-Performance MEMS Gyroscopes," in *Proc. 16th International Conference on Solid-State Sensors, Actuators and Microsystems (Transducers'11)*, Beijing, China, 2011, pp. 2817-2820.

[47] T. K. Tang, R. C. Gutierrez, J. Wilcox, C. Stell, V. Vorperian, R. Calvet, W. Li, I. Charkaborty, R. Bartman, and W. Kaiser, "Silicon Bulk Micromachined Vibratory Gyroscope," in *Proc. Solid-State Sensor and Actuator Workshop (Hilton Head'96)*, Hilton Head, S.C., 1996, pp. 288-293.

[48] "MEMS Inertial Products Performance and Production Readiness", Accessed on April 1st, 2008. Available: http://www.ssec.honeywell.com/pressure/new/20050907

[49] M. I. Ferguson, D. Keymeulen, C. Peay, K. Yee, and D. L. Li, "Effect of Temperature on MEMS Vibratory Rate Gyroscope," *in Proc. IEEE Aerospace 2005 Conference*, Big Sky, MT, 2005, pp. 1-6.

[50] F. Paoletti, M. A. Gretillat, and N. F. de Rooij, "A silicon micromachined vibrating gyroscope with piezoresistive detection and electromagnetic excitation," in *Proc. 9th IEEE International Workshop an Investigation of Micro Structures, Sensors, Actuators, Machines and Systems (MEMS'96)*, San Diego, CA, 1996, pp. 162-167.

[51] K. Fukatsu, T. Murakoshi, and M. Esashi, "Electrostatically levitated micro motor for inertia measurement system," in *Proc. 10th International Conference on Solid-State Sensors and Actuators (Transducers'99)*, Sendai, Japan, 1999, pp. 1558-1561.

[52] C. Shearwood, K. Y. Ho, and H. Q. Gong, "Testing of a micro-rotating gyroscope," in *Proc. 10th International Conference on Solid-State Sensors and Actuators (Transducers'99)*, Sendai, Japan, 1999, pp. 984–987.

[53] C-L. Wong and M.Palaniapan, "Phonon detection technique for the study of the temperature coefficient of resonance frequency in clamped–clamped beam resonators", *J. Micromech. Microeng.,* vol. 19, no.6, pp. 1-10, 2009.

[54] S-H Lee, "Wafer-Level Packaging for Environment-Resistant Microinstruments," Ph.D. dissertation, Dept. Elect. Eng. and Comp. Sci., Univ. Michigan, Ann Arbor, MI, 2008.

[55] W. Geiger, B. Folkmer, U. Sobe, H. A. S. H. Sandmaier, and W. A. L. W. Lang, "New designs of micromachined vibrating rate gyroscopes with decoupled oscillation modes," in *Proc. International Conference on Solid State Sensors and Actuators (Transducers'97)*, Chicago, IL, 1997, pp. 1129-1132.

[56] S. S. Baek, Y. S. Oh, B. J. Ha, S. D. An, B. H. An, H. Song, and C. M. Song, "A symmetrical z-axis gyroscope with a high aspect ratio using simple and new process," in *Proc. 12th IEEE International Conference on Micro Electro Mechanical Systems (MEMS'99)*, Orlando, FL, pp. 612-617.

[57] S. Kobayashi, T. Hara, T. Oguchi, Y. Asaji, K. Yaji, and K. Ohwada, "Double-Frame Silicon Gyroscope Packaged Under Low Pressure By Wafer Bonding," in *Proc. 10th International Conference on Solid-State Sensors and Actuators (Transducers' 99)*, Sendai, Japan, 1999, pp. 972-975.

[58] S. Lee, S. Park, J. Kim, S. Lee, and D. I. Cho, "Surface/bulk micromachined single-crystalline-silicon micro-gyroscope," *J. Microelectromechanical Systems*, vol. 9, no. 4, pp. 557-567, 2000.

[59] S. E. Alper and T. Akin, "A symmetric surface micromachined gyroscope with decoupled oscillation modes," *Sensors & Actuators: A. Physical*, vol. 97, pp. 347-358, 2002.

[60] A. A. Seshia, R. T. Howe, and S. Montague, "An integrated microelectromechanical resonant output gyroscope," in *Proc. 15th IEEE International Conference on Micro Electro Mechanical Systems (MEMS'02)*, Las Vegas, NV, 2002, pp. 722-726.

[61] G. Yan, Y. Zhu, C. Wang, R. Zhang, Z. Chen, X. Liu, and Y. Y. Wang, "Integrated bulk-micromachined gyroscope using deep trench isolation technology," in *Proc. 17th IEEE International Conference on Micro Electro Mechanical Systems (MEMS'04)*, Maastricht, Netherlands, 2004, pp. 605-608.

[62] L. A. Oropeza-Ramos, C. B. Burgner, and K. L. Turner, "Inherently robust micro gyroscope actuated by parametric resonance," in *Proc. 21st IEEE International Conference on Micro Electro Mechanical Systems (MEMS'08)*, Tucson, AZ, 2008, pp. 872-875.

[63] Y. Oh, B. Lee, S. Baek, H. Kim, J. Kim, S. Kang, and C. Song, "A surface-micromachined tunable vibratory gyroscope," in *Proc. 10th IEEE International Conference on Micro Electro Mechanical Systems (MEMS'97)*, Nagoya, Japan, 1997, pp. 272-277.

[64] T. Tsuchiya, Y. Kageyama, H. Funabashi, and J. Sakata, "Vibrating gyroscope consisting of three layers of polysilicon thin films," *Sensors & Actuators: A. Physical*, vol. 82, pp. 114-119, 2000.

[65] S. E. Alper and T. Akin, "Ultra-Thick and High-Aspect-Ratio Nickel Microgyroscope Using EFAB TM Multi-Layer Additive Electroforming," in *Proc. 19th IEEE International Conference on Micro Electro Mechanical Systems (MEMS'06)*, Istanbul, Turkey, 2006, pp. 670-673.

[66] X. S. Liu, Z. C. Yang, X. Z. Chi, J. A. Cui, H. T. Ding, Z. Y. Guo, B. Lv, and G. Z. Yan, "An x-axis micromachined gyroscope with doubly decoupled oscillation modes," in *Proc. 21st IEEE International Conference on Micro Electro Mechanical Systems (MEMS'08)*, Tucson, AZ, 2008, pp. 860-863.

[67] K. Maenaka, "A study of silicon angular rate sensors using anisotropic etching technology," *Sensors and Actuators. A, Physical*, vol. 43, p. 72, 1994.

[68] O. Bochobza-Degani, D. J. Seter, E. Socher, and Y. Nemirovsky, "A Novel Micromachined Vibrating Rate Gyroscope with Optical Sensing and Electrostatic

Actuation," in *Proc. 10th International Conference on Solid-State Sensors and Actuator (Transducers '99)*, Sendai, Japan, 1999.

[69] S. A. Bhave, J. I. Seeger, J. Xuesong, B. E. Boser, R. T. Howe, and J. A. Yasaitis, "An integrated, vertical-drive, in-plane-sense microgyroscope," *in Proc. 12th International Conference on Solid-State Sensors, Actuators and Microsystems (Transducers'03)*, Boston, MA, 2003, pp. 171-174.

[70] G. H. He, C. T. Nguyen, J. Hui, M. S. Wong, A. F. L. Ng, H. C. Luong, and C. Ling, "A piezoelectric-plate microgyroscope," *in International Conference on Solid State Sensors and Actuators (Transducers'97)*, Chicago, IL, 1997, pp. 895-898.

[71] K. Funk, H. Emmerich, A. Schilp, M. Offenberg, R. Neul, and F. Larmer, "A surface micromachined silicon gyroscope using a thick polysilicon layer," in *Proc. 12th IEEE International Conference on Micro Electro Mechanical Systems (MEMS'99)*, Orlando, FL, pp. 57-60, 1999.

[72] J. A. Geen, "Single-chip surface micromachined integrated gyroscope with 50 deg/h Allan deviation," *IEEE J. Solid-State Circuits*, vol. 37, no. 12, pp. 1860, 2002.

[73] M. Lutz, W. Golderer, J. Gerstenmeier, J. Marek, B. Maihofer, S. Mahler, H. Munzel, and U. Bischof, "A precision yaw rate sensor in silicon micromachining," in *Proc. International conference on Solid-State Sensors and Actuators (Transducers'97)*, Chicago, IL, 1997, pp. 847-850.

[74] K. Azgin, Y. Temiz, and T. Akin, "An SOI-MEMS tuning fork gyroscope with linearly coupled drive mechanism," in *Proc. 20th IEEE International Conference on Micro Electro Mechanical Systems (MEMS'07)*, Kobe, Japan, 2007, pp. 607-610.

[75] J. Soderkvist, "Piezoelectric beams and vibrating angular rate sensors," *IEEE Transactions on Ultrasonics, Ferroelectrics and Frequency Control*, vol. 38, pp. 271-280, 1991.

[76] M. Hashimoto, C. Cabuz, K. Minami, and M. Esashi, "Silicon resonant angular rate sensor using electromagnetic excitation and capacitive detection," *J. Micromech. Microeng.*, vol. 5, pp. 219–25, 1995.

[77] G. Zhou, K. K. L. Cheo, D. Yu, and F. S. Chau, "A novel optical lamellar grating out-of-plane microgyroscope," in *Proc. 21st IEEE International Conference on Micro Electro Mechanical Systems (MEMS'08)*, Tucson, AZ, pp. 864-867.

[78] R. Voss, K. Bauer, W. Ficker, T. Gleissner, W. Kupke, M. Rose, S. Sassen, J. Schalk, H. Seidel, and E. Stenzel, "Silicon angular rate sensor for automotive applications with piezoelectric drive and piezoresistive read-out," in *Proc. International conference on Solid-State Sensors and Actuators (Transducers'97)*, Chicago, IL, 1997, pp. 847-850.

[79] U. Breng, W. Gutmann, P. Leinfelder, B. Ryrko, S. Zimmermann, D. Billep, T. Gessner, K. Hiller, and M. Wiemer, "µCORS-a bulk micromachined gyroscope based on coupled resonators," *in Proc. 10th International Conference on Solid-State Sensors and Actuator (Transducers '99)*, Sendai, Japan, 1999, pp. 1570-1573.

[80] S. E. Alper, K. Azgin, and T. Akin, "High-Performance SOI-MEMS Gyroscope with Decoupled Oscillation Modes," in *Proc. 19th IEEE International Conference on Micro Electro Mechanical Systems (MEMS'06)*, Istanbul, Turkey, pp. 70-73.

[81] F. Ayazi, "A high aspect-ratio high-performance polysilicon vibrating ring gyroscope," Ph.D. dissertation, Dept. Elect. Eng. and Comp. Sci., Univ. Michigan, Ann Arbor, MI, 2000.

[82] M. F. Zaman, A. Sharma, B.V. Amini, and F. Ayazi, "The resonating star gyroscope," in *Proc. 18th IEEE International Conference on Micro Electro Mechanical Systems (MEMS'05)*, Miami, FL, 2005, pp. 355-358.

[83] G. I. Andersson, N. Hedenstierna, P. Svensson, and H. Pettersson, "A novel silicon bulk gyroscope," in *Proc. 10th International Conference on Solid-State Sensors and Actuators (Transducers' 99)*, Sendai, Japan, 1999, pp. 902–905.

[84] N. Hedenstierna, S. Habibi, S. M. Nilsen, T. Kvisteroy, and G. U. Jensen, "Bulk micromachined angular rate sensor based on thebutterfly'-gyro structure," *in Proc. 14th International Conference on Micro Electro Mechanical Systems (MEMS'01)*, Interlaken, Switzerland, 2001, pp. 178-181.

[85] M. Abe, E. Shinohara, K. Hasegawa, S. Murata, and M. Esashi, "Trident-type tuning fork silicon gyroscope by the phase difference detection," *in Proc. 13th International Conference on Micro Electro Mechanical Systems (MEMS'00)*, Miyazaki, Japan, 2000, pp. 508-513.

[86] J. A. Geen and J. Kuang, "Cross-quad and vertically coupled inertial sensors," U.S Patent 7 421 897, September 9th, 2005.

[87] K. Maenaka, H. Kohara, M. Nishimura, T. Fujita, and Y. Takayama, "Novel Solid Micro-Gyroscope," *in Proc. 19th IEEE International Conference on Micro Electro Mechanical Systems(MEMS'06)*, Kobe, Japan, 2006, pp. 634-637.

[88] D. D. Lynch, "Vibratory gyro analysis by the method of averaging," *in Proc. 2nd Saint Petersburg International Conference on Gyroscopic Technology and Navigation*, St. Petersburg, Russia, 1995, pp. 26–34.

[89] B. Friedland and M. F. Hutton, "Theory and Error Analysis of Vibrating-Member Gyroscope", *IEEE Transactions on Automatic Control*, vol. AC-23, no. 4, August 1978.

[90] *IEEE Standard Specification Format Guide and Test Procedure for Single-Axis Interferometric Fiber Optic Gyros*, IEEE Standards 952, 1997.

[91] T.B. Gabrielson, "Mechanical-Thermal Noise in Micromachined Acoustic and Vibration sensors," *IEEE Transactions on Electron Devices*, vol. 40, no. 5, pp. 903-909, 1993.

[92] F. Ayazi, "Multi-DOF Inertial MEMS: From gaming to dead reckoning", in *Proc. 16th International Conference on Solid-State Sensors, Actuators and Microsystems (Transducers'11)*, Beijing, China, 2011, pp. 2805-2808.

[93] V. Ph. Zhuravlev, "A controlled Foucault pendulum as a model of a class of free gyros," *Izv. AN. MTT [Mechanics of Solids]*, no. 6, pp. 27-35, 1997.

[94] D. D. Lynch, "Vibratory gyro analysis by the method of averaging," *in Proc. 2nd Saint Petersburg International Conference on Gyroscopic Technology and Navigation*, St. Petersburg, Russia, 1995, pp. 26–34.

[95] E. J Loper and D.D. Lynch, "Hemispherical Resonator Gyro Status Report and Test Results," in *Proc. National Technical Meetings, Institute of Navigation*, San Diego, CA, 1984.

[96] L. Meirovitch, *Elements of Vibration Analysis*, Singapore, Singapore: McGraw-Hill, 1986.

[97] A. Bedford and W. L. Fowler, *Engineering Mechanics: Dynamics*, 3rd ed., Prentice Hall, 2001.

[98] R. D. Blevins, Formulas for Natural Frequencies and Mode Shapes, New York: Krieger, 1979.

[99] B. J. Gallacher, J. S. Burdess, A. J. Harris, and M. E. McNie, "Principles of a three-axis vibrating gyroscope", *IEEE Transactions on Aerospace and Electronic Systems*, vol. 37, no. 4, 1333-1343, 2001.

[100] F. P. Beer, E. R. Johnston, and J. T. DeWolf, "Mechanics of Materials", 3rd ed., McGraw-Hill, 2002.

[101] Boroafloat 33 datasheet. Available: http://www.schott.com/borofloat/english/download/thermal_expa.pdf, accessed on Nov 1st, 2010.

[102] Y. Okada and Y. Tokumaru, "Precise determination of lattice parameter and thermal expansion coefficient of silicon between 300 and 1500 K", *J. Appl. Phys.*, vol. 56, no. 2, pp. 314-321, 1984.

[103] S. E. Alper, K. M. Silay, and T. Akin, "Tactical-grade silicon-on-glass gyroscope with very-small quadrature coupling," in *Proc. 19th European Conf. on Solid-State Transducers (Eurosensors XIX)*, Göteborg, Sweden, 2006.

[104] H. Johari, Micromachined Capacitive Silicon Bulk Acoustic Wave Gyroscopes Ph.D. dissertation, Dept. Mech. Eng., Georgia. Inst. Tech., Atlanta, GA, 2008.

[105] M. F. Zaman, Degree-Per-Hour Mode-Matched Micromachined Silicon Vibratory Gyroscopes, Ph.D. dissertation, Dept. Elec. Eng., Georgia. Inst. Tech., Atlanta, GA, 2008.

[106] C. Zener, "Internal friction in solids, I. Theory of internal friction in reeds," *Phys. Rev.*, vol. 52, pp. 230-235, 1937.

[107] S. Lee, Micromechanical Resonator Reference Oscillators for Wireless Communications, Dept. Elect. Eng. and Comp. Sci., Univ. Michigan, Ann Arbor, MI, 2008.

[108] W. C. Tang, M.G. Lim, and R.T. Howe, **"**Electrostatic Comb Drive Levitation and Control Method," *J. Microelectromech. Syst.*, vol. 1, no. 4, pp. 170–178, Oct. 1992.

[109] Lynch, A. Matthews, and G.T.Varty, " Innovative Mechanizations to Optimize Inertial Sensors for High or Low Rate Operations", *Symposium Gyro Technology*, Stuttgart, Germany, 1997.

[110] J. Cho and K. Najafi, "Gyroscope", U. of Michigan Tech. Transfer Office, US Provisional Application #61/490,038, May 11th, 2011.

[111] M. Koning, "Vibrating cylinder gyroscope and method," U.S Patent 4 793 195, Dec. 27, 1988.

[112] J. Cho, J.A. Gregory, K. Najafi, "Single-Crystal-Silicon Vibratory Cylindrical Rate Integrating Gyroscope (CING)," *in Proc. 16th International Conference on Solid-State Sensors, Actuators, and Microsystems (TRANSDUCERS'11*), Beijing, China, 2011, pp. 2813-2816.

[113] Y. Jimbo and K. Itao, "Energy loss of a cantilever vibrator", *J. Horological Institute of Japan*, vol. 47, pp.1-15, 1968 (in Japanese).

[114] Hao, Erbil, and Ayazi, "An analytical model for support lloss in micromachined beam resonators with in-phase flexural vibrations", *Sensors and Actuators A*, vol. 109, pp. 156-164, 2003.

[115] S. Bindel, "Structured and Parameter-Dependent Eigensolvers for Simulation-Based Design of Resonant MEMS", Ph.D. Thesis, Dept. Comp. Sci., Univ. California-Berkeley, Berkeley, CA, 2006.

[116] P.G. Steeneken, J.J.M. Ruigrok, S. Kang, J.T.M. van Beek, J. Bontemps and J.J. Koning, "Parameter Extraction and Support-Loss in MEMS Resonators," *in Proc. Comsol conference 2007*, Grenoble, France, 2007, p. 725.

[117] K.Y. Yasumura, T.D. Stowe, E.M. Chow, T. Pfafman, T.W. Kenny, B.C. Stipe, and D. Rugar , "Quality factors in micron- and submicron-thick cantilevers, " *Journal of Microelectromechanical Systems*, vol. 9, pp. 117-125, 2000.

[118] E. J. Loper et al., "Projected performance of smaller hemispherical resonator gyros," in *Proc. PLANS '86 - Position Location and Navigation Symposium*, Las Vegas, NV, 1986, pp. 61-64.

[119] J. Gregory, J. Cho, K. Najafi, "Characterization and control of a high-Q MEMS inertial sensor using low-cost hardware," *IEEE ION/PLANS Conference*, Myrtle Beach, S.C., April 24th, 2012.

[120] J. Gregory, J. Cho, K. Najafi, "Rate and rate-integrating gyroscope control with commercial software defined radio hardware," in *Proc. 16th International Conference on Solid-State Sensors, Actuators, and Microsystems (Transducers'11)*, Beijing, China, 2011, pp. 2394-2397.

[121] S. P. Murarka, H. J. Levinstein, I. Blech, T. T. Sheng, and M. H. Read, "Investigation of the Ti-Pt Diffusion Barrier for Gold Beam Leads on Aluminum", *J. Electrochem. Soc.*, vol. 125, no. 1, pp. 156-162, 1978.

[122] J. Cho, J. Gregory, K. Najafi, "High-Q, 3kHz Single-Crystal-Silicon Cylindrical Rate-Integrating Gyro (CING)", in *Proc. 25th IEEE International Conference on Micro Electro Mechanical Systems (MEMS'12)*, Paris, France, 2012.

[123] M. Paz and W. E. Leigh, "Structural Dynamics: Theory and Computation", 4th ed., Kluwer Academic Publishers, 2001.

[124] D.D. Lynch, "Vibration Induced Drift in the Hemispherical Resonator Gyro," in *Proc. The institute of navigation proceedings of the forty-third annual meeting*, 1987, pp. 34-37.

[125] S. Lee, J. Cho, and K. Najafi, "Fabrication of vertical comb electrodes using selective anodic bonding," *in Proc. 20th International Conference on Micro Electro Mechanical Systems (MEMS'07)*, Kobe, Japan, 2007, pp. 349-352.